Defect-Driven Processing of Two-Dimensional Transition Metal Dichalcogenides

by

Kevin Christopher Bogaert

B.S. in Materials Science and Engineering

Georgia Institute of Technology, 2014

Submitted to the Department of Materials Science and Engineering

in Partial Fulfillment of the Requirements for the Degree of

Doctor of Philosophy

in Materials Science and Engineering at the

Massachusetts Institute of Technology

June 2019

Author: _____

Department of Materials Science and Engineering

April 30, 2019

Certified by: _____

Silvija Gradečak

Professor of Materials Science and Engineering

Thesis Supervisor

Accepted by: _____

Donald R. Sadoway

Chairman, Departmental Committee on Graduate Studies

Defect-Driven Processing of Two-Dimensional Transition Metal Dichalcogenides

by Kevin C. Bogaert

Submitted to the Department of Materials Science and Engineering
on April 30, 2019, in Partial Fulfillment of the
Requirements for the Degree of Doctor of Philosophy
in Materials Science and Engineering

Abstract

Two-dimensional transition metal dichalcogenides (TMDs) are an emerging class of semiconductor materials that offer exciting new properties for future electronic and optoelectronic applications. However, many ongoing challenges related to synthesis and processing must be overcome before this nascent technology can become industrially viable. In this thesis, processing-related phenomena relevant to the fabrication of TMD heterostructures, alloys, and nanoporous membranes are presented.

This thesis begins with an investigation of the role of substrate temperature in two-step chemical vapor deposition (CVD) growth of MoS_2/WS_2 heterostructures. We demonstrate diffusion-mediated synthesis of inverted lateral heterostructures following low MoS_2 growth temperatures in the second CVD step and homogeneous $Mo_xW_{1-x}S_2$ alloyed crystals following higher MoS_2 growth temperatures.

Investigating the nature of this diffusion-mediated process, we identify an energetically favorable atomistic model proposing that transition metal diffusion is driven by a heterogeneous distribution of sulfur vacancies. This model is corroborated by the synthesis of a composition-graded $Mo_xW_{1-x}S_2$ alloy crystals in which the final-stage spatial distribution of transition metal

atoms correlates with intermediate-stage distribution of point defects. These heterogeneous crystals allow for correlation of the local optical properties with the local composition, demonstrating a variation in photoluminescence intensity spanning two orders of magnitude and reaching the maximum value for equicompositional alloy $Mo_{0.5}W_{0.5}S_2$ (x=0.5).

Furthermore, the correlation between intermediate-stage distribution of point defects and final-stage spatial distribution of transition metal atoms enables the opportunity for bespoke patterning. Utilizing a laser annealing technique, we demonstrate the ability to locally induce defects that define the regions of preferential nucleation during subsequent CVD growth.

Finally, defect processing is also demonstrated in nanoporous TMD membrane applications. Combining modeling with experimentation, we demonstrate the relationship between vacuum annealing time and temperature with nanopore properties such as average radius and edge structure. Control of these properties is essential for the fabrication of functional nanoporous membrane devices for sensing, filtration, and energy applications.

This thesis motivates further work on TMD processing in pursuit of developing a fundamental understanding of the defect-driven diffusion mechanism, a larger library of interesting TMD compositions and structures, as well as industrially viable TMD devices.

Thesis Supervisor: Silvija Gradečak
Title: Professor of Materials Science and Engineering

Acknowledgements

I would like to thank my advisor, Prof. Silvija Gradečak. She provided a number of opportunities for me to grow, professionally and personally, and supported me as the founding member of the two-dimensional materials branch of the lab. I would also like to thank Prof. Jeffrey Grossman and Prof. Carl Thompson for serving as members of my thesis committee and for offering support and advice throughout the course of this research.

I would also like to thank the current and former members of the Gradečak group. Jordan Chesin was an invaluable mentor to me during the early stages of my research, helping me to construct our first 2D materials CVD system and forming a journal club to stay up-to-date in the rapidly changing field of 2D research. Akshay Singh, Jian-An Ke, and Haeyeon Lee have spent countless hours working alongside me to improve growth recipes and develop various processing and characterization techniques. To the rest of the group – Hadi Dastjerdi, Sarah Goodman, Olivia Hentz, Zhibo Zhao, Nina Andrejevic, Jayce Cheng, Paul Rekemeyer, Sema Ermez, Eric Jones, John Hanson, and Denis Titow – for contributing technical expertise, listening to countless practice talks and research updates, sharing wisdom, and providing guidance and support.

I would also like to thank Prof. Slaven Garaj and the Garaj group at the National University of Singapore. Prof. Garaj hosted me as a visiting researcher in his lab four times for seven cumulative months, allowing me access to some of the most advanced equipment and leading experts in the field of 2D materials. My thesis would be an entirely different document if it were not for these opportunities. Over the course of my numerous visits to the Garaj group, I developed meaningful research collaborations and friendships with members of the Garaj group. I would especially like to thank Song Liu, Tao Liu, Massimo Spina, Rajesh Sharma, and Milan Blašković. Also in the Singapore community, I would like to thank Prof. Chun Zhang and Na Guo of NUS for their DFT contributions to the work presented in Chapter 4 and Prof. Martial Duchamp and Chris Boothroyd of Nanyang Technological University for their TEM contributions to the work presented in Chapter 6.

I would like to thank my friends and family for their support throughout this journey. I would like to thank Owen Morris, Jérôme Michon, Jonathan Hwang, and Seth Cazzell for the time we shared at our Seckel St. apartment as well as Erica Lai, Derek Kita, Chris Couch, and Jason Adams for their friendship and support. I owe an enormous debt of gratitude to Sarah Schwartz for providing the emotional support to help me savor the highs and survive the lows of graduate school. Lastly and most importantly, I am thankful for my parents, Debra and Paul, as well as my sister, Lauren, and my extended family for instilling the values and providing the never-ending support and love to help me pursue my dreams, wherever that journey takes me.

Table of Contents

List of Figures

List of Tables

List of Abbreviations

Abbreviations

2D	Two-dimensional
AC	Armchair
AFM	Atomic force microscopy
CVD	Chemical vapor deposition
DNA	Deoxyribonucleic acid
DFT	Density functional theory
EDS	Energy-dispersive X-ray spectroscopy
HAADF	High-angle annular dark field
IQE	Internal quantum efficiency
NR	Non-radiative
PL	Photoluminescence
PMMA	Poly(methyl methacrylate)
RPM	Rotations per minute
RR	Radiative recombination
SEM	Scanning electron microscopy
SRH	Shockley-Read-Hall
STEM	Scanning transmission electron microscopy
TEM	Transmission electron microscopy/microscope
TMD	Transition metal dichalcogenide
vdW	van der Waals
ZZ	Zigzag

Mathematical symbols

a	Interatomic distance
α	Average surface area per atom
A	Area
C	Concentration
d_{SF}	stagnant film boundary layer thickness
D	Diffusivity
E_a	Activation energy
f_P	Faceting parameter
F	Flux
γ	Surface energy
G	Free energy
G_R	Average radial growth rate
Γ	Jumping rate
h_G	Gas phase mass transport coefficient
h_{Vap}	Enthalpy of vaporization
k_B	Boltzmann constant
k_S	Surface reaction rate constant
λ	Mean free path
m	Layer number
μ	Viscosity
n	Number of clusters
ν	Jumping attempt frequency
N	Number of atoms
p_R	Removal probability
P	Pressure
r	Radius
ρ	Density
R_e	Evaporation rate
t	Time
τ	Carrier lifetime
T	Temperature
U	Bulk gas flow velocity
w	Wave number
x	Spatial distance or alloy composition
y	Spatial distance
z	Thickness

Chapter 1: Introduction and Motivation

The 1956 Nobel Prize in Physics was awarded to William Shockley, John Bardeen, and Walter Brattain "for their researches on semiconductors and their discovery of the transistor effect."[1] Their 1947 invention of a working solid-state transistor demonstrated a scalable replacement to the vacuum tube technology used in early computing. Over the following decades to the present day, advances in semiconductor research and transistor manufacturing for the computing industry have followed a trend known as Moore's Law, resulting in an approximately biennial doubling in the number of components per integrated circuit.[2]

Alongside these advances in computing technologies, other semiconductor technologies such as photovoltaics[3] and light emitting diodes[4] have improved significantly due to research in materials discovery and processing. In addition to the thorough understanding of silicon-based technologies built on over a half-century of research, semiconductor device prospects have also significantly improved due to research in alternative semiconducting materials such as III-V,[4] carbon nanotube,[5] perovskite,[6] and two-dimensional (2D) materials.[7,8] These alternative semiconducting materials have the potential to enable further advancement in device performance for various applications in which their unique properties exceed those of more traditional options such as silicon. To achieve this potential, these materials must escape their relative nascence to become well-understood technologies with processing capabilities and control on par with competitive traditional devices.

In this chapter, we will introduce two-dimensional transition metal dichalcogenides (TMDs) as an emerging class of semiconducting materials. By discussing the novel properties and ongoing challenges related to the processing capabilities of this materials class, we will motivate

the work discussed in the remainder of this thesis which aims to address some of these challenges.

1.1 **Two-dimensional transition metal dichalcogenides**

1.1.1 Properties

TMDs such as MoS_2 are naturally occurring crystalline minerals. The crystal structure consists of three-atom-thick sheets (*i.e.*, monolayers) with a hexagonal atomic arrangement (Figure 1-1).[9] The hexagonal lattice consists of alternating sites of either a single transition metal atom (*e.g.*, Mo, W) or a pair of chalcogen atoms (*e.g.*, S, Se, Te). The transition metal atom is positioned in the central plane of the sheet whereas the pair of chalcogen atoms are split into the top and bottom planes. Ideal monolayers have no c-axis dangling chemical bonds and are only bound to their substrate or other TMD monolayers by van der Waals (vdW) bonding with a layer thickness of approximately 6.5 Å.

Due to the weak nature of vdW bonding, bulk TMDs have commonly been used as dry lubricants alongside graphite, another vdW-bonded layered material.[10,11] In 2004, monolayers of graphite (*i.e.*, graphene) were isolated and measured to be semimetals with a strong ambipolar electric field effect and room-temperature mobilities of ~10,000 cm^2/Vs.[12] For their isolation and characterization of graphene as a remarkable 2D conductor, Andre Geim and Konstantin Novoselov were awarded the 2010 Nobel Prize in Physics.[13] In that same year, the isolation of monolayer MoS_2 was first reported. Early research on monolayer MoS_2 demonstrated quantum confinement effects upon thinning to the monolayer limit such as a crossover from an indirect band gap to direct band gap and a consequent improvement in luminescence quantum yield by orders of magnitude.[14–16] Shortly thereafter, MoS_2 field-effect transistors were reported with a room-temperature current on/off ratio exceeding 1×10^8 and mobility of ~200 $cm^2V^{-1}s^{-1}$.[17] With

direct band gap energies ranging from 1.55 to 1.97 eV (Table 1-1) and exciton binding energies of 320 to 570 meV,[18–20] monolayer TMDs are a promising class of materials for high-speed and low-power electronic, optoelectronic and photonic applications.[21–23]

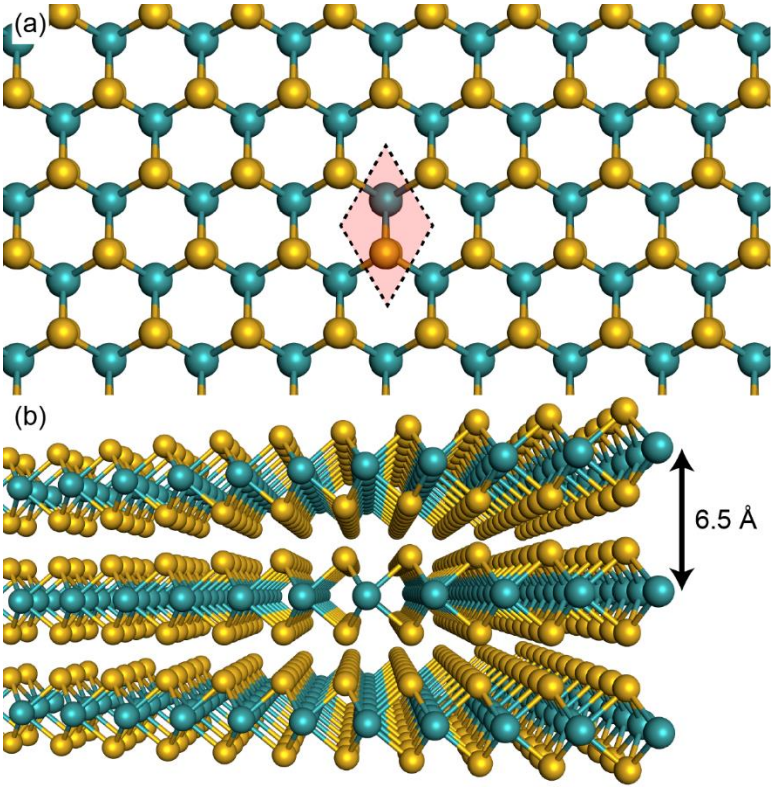

Figure 1-1. (a) Planar and **(b)** side views of a MoS_2 crystal. The red diamond in (a) defines the unit cell.

Material	Band Gap (eV)	Lattice Constant (Å)
MoS_2	1.82	3.160
WS_2	1.97	3.155
$MoSe_2$	1.55	3.299
WSe_2	1.65	3.286

Table 1-1. Optical band gaps and lattice constants of some of the most commonly studied monolayer TMDs.[24–26]

1.1.2 Heterostructures

Due to the composition-dependent properties of 2D TMDs, there is a desire to create heterostructures in which an interface between two 2D TMDs corresponds to an abrupt change in

material properties, such as a p-n junction. These 2D heterostructures are divided into two classes by the topology of their interfaces: lateral and vertical heterostructures (Figure 1-2).[24] In a lateral heterostructure, the full structure is a single monolayer in which the composition of the monolayer varies in-plane. Consequently, the interface between the constituent materials is one-dimensional and comprised of chemical bonds. In a vertical heterostructure, the full structure is comprised of multiple monolayers stacked on top of one another in which the constituent materials occupy separate planes. Vertical heterostructure interfaces are two-dimensional and comprised of vdW bonds.

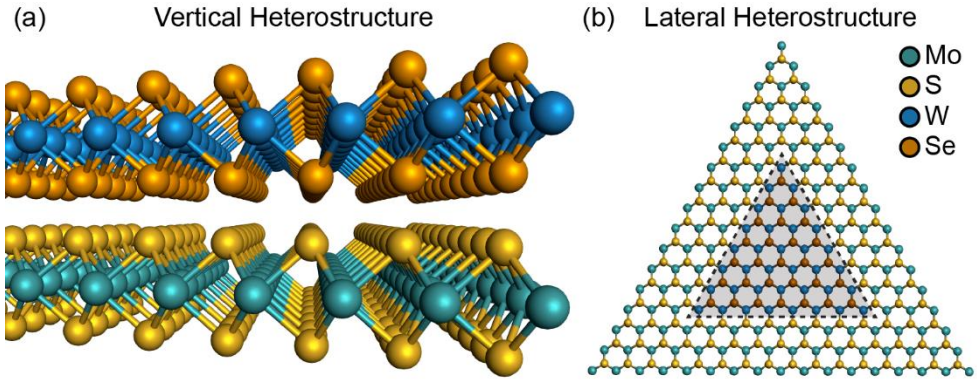

Figure 1-2. Schematics of a **(a)** vertical and **(b)** lateral heterostructure with 2D TMD domains.

As indicated in Table 1-1, the lattice constants of TMDs sharing the same chalcogen element are virtually identical whereas the lattice constants of TMDs with different chalcogen elements vary by a few percent. Given that TMDs also share the same hexagonal monolayer crystal structure, it is relatively trivial to construct high-quality interfaces between these materials to form heterostructures, albeit with some strain or dislocations in the case of lateral heterostructures with different chalcogen elements.

Vertical heterostructures can be synthesized by mechanical stacking techniques (see Section 2.1.1) or by chemical growth techniques (see Section 2.1.2) due to the poor bonding between layers. However, the in-plane chemical bonding within monolayers necessitates that lateral

heterostructures must be produced by chemical growth techniques. Lattice continuity of lateral heterostructures yields superior in-plane electronic properties, including excellent current rectification behavior and photocurrent generation characteristics.[27,28] Furthermore, lateral in-plane heterostructures can act as intrinsic p-n junctions and have arbitrarily tuned bandgaps *via* alloying. Chemical growth presents a more scalable and reproducible method for heterostructure fabrication and so it has generated more interest within the field. Several chalcogen-changing (*e.g.*, $MoS_2/MoSe_2$ or WS_2/WSe_2), metal-changing (*e.g.*, MoS_2/WS_2 or $MoSe_2/WSe_2$), and dual-changing (*e.g.*, MoS_2/WSe_2) lateral heterostructures grown by chemical vapor deposition (CVD) have been reported.[24,27–34]

In one-step lateral heterostructure growth processes, two metallic precursors are simultaneously present in the reaction chamber during the growth; after the growth, the material with higher vapor pressure and nucleation rate is found in the core of the 2D crystal.[24,29,31,34–38] In two-step growths, the core domain of the first material is grown first, followed by the exchange of precursors and the growth of the ring of the second material.[27,28,30,32,39] While these growth techniques are successful, they offer little control for complexity as the radial domain configuration is strictly a function of growth chronology.

One of the goals of the work presented in this thesis is to develop an understanding of the mechanisms that govern the growth of pure and multi-phase TMDs that will be critical for engineering more advanced heterostructures with controlled properties. This involves an investigation of the role of processing parameters, as will be discussed in Chapter 3, as well as the development of new processing techniques, as will be discussed in Chapter 5.

In addition to the work presented in this thesis, other researchers have made parallel developments in the field of 2D TMD processing. These include top-down patterning methods

involving masked etching,[40,41] selective chalcogen conversion of $MoSe_2$ into $MoS_2/MoSe_2$ heterostructures,[42] and bottom-up methods of surface functionalization and lithographically patterned seeding to yield selective nucleation.[43–47] While these techniques have provided useful contributions to the field, further research is still necessary to enable the fabrication of arbitrary heterostructures with highly controlled spatial configurations of domains with bespoke compositions and properties.

1.1.3 Alloys

In addition to the benefits of creating atomically abrupt hetero-interfaces, there are also benefits to creating 2D TMD alloys by utilizing the similar crystal structure and lattice spacing of these materials to create crystals that possess properties that continuously span the full range of their pure counterparts. These alloyed crystals can be divided into multiple classes based on composition (*i.e.*, metal-alloyed and/or chalcogen-alloyed) or spatial distribution (*i.e.*, uniform or graded). Similar to one-step lateral heterostructure growth processes, composition-graded alloy growth processes often involve the delayed introduction and/or vaporization of one or more precursor, resulting in a radial composition distribution that correlates with the chronology and relative abundance of each precursor.[34–36,48–51] Conversely, uniform alloy growth processes aim to maintain a constant abundance of each precursor throughout crystal growth.[52–59] Beyond alloying by growth, alloying can also be achieved by post-processing of crystals through techniques such as atomic substitution.[60] As with heterostructures, there is an ongoing need to improve the processing capabilities and controls of TMD alloys to enable the fabrication of crystals with high spatial control of local composition and properties, as will be discussed in Chapter 4.

1.1.4 Defects

Like in any other crystalline solid, defects are thermodynamically inevitable in monolayer TMDs. Limited by the dimensionality of the crystal, defects in 2D TMDs exist in no greater than two dimensions of space. Examples of common structural defects in TMDs include 2D pores,[61] 1D dislocations and grain boundaries,[62,63] and 0D point defects (*e.g.*, substitutions, vacancies) (Figure 1-3).[64]

Vacancies are especially common in chemically grown samples due to imperfections in the growth process. Monosulfur vacancies (V_S) have the lowest formation energy among the intrinsic point defects in monolayer MoS_2, followed by disulfur vacancies (V_{S_2}), molybdenum vacancies (V_{Mo}), vacancy complexes (e.g., V_{MoS_3}), and eventually antisite defects (*e.g.*, Mo_{S_2} or $S_{2_{Mo}}$).[64] Although a non-zero concentration of monosulfur vacancies is expected to exist, an excess of vacancies beyond thermodynamic equilibrium can exist due to external factors such as sample irradiation or annealing. Under high vacancy conditions, material systems are subjected to a thermodynamic driving force to minimize the energy of the system by vacancy agglomeration. In monolayer transition metal disulfides, this has been observed to occur by a process of sulfur vacancy diffusion into 1D vacancy channels.[65–68]

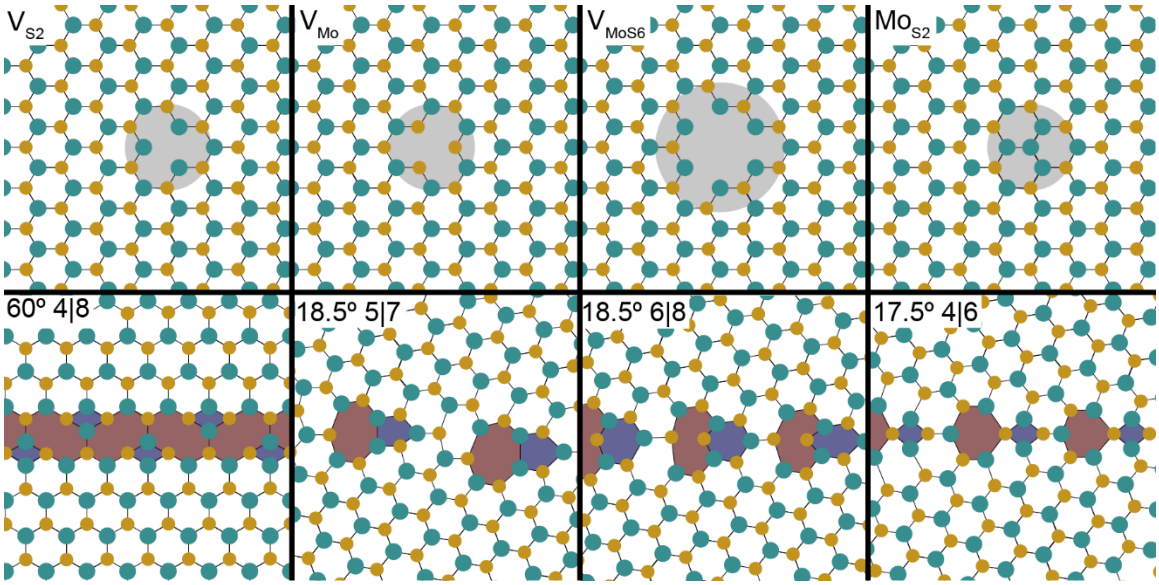

Figure 1-3. Common point defects (top row) and grain boundary dislocations (bottom row) in MoS_2.[64]

Two-dimensional pores in TMDs are often the result of thermal decomposition and/or oxidation.[61,69,70] This process can be initiated during chemical growth due to a precursor deficiency, following growth due to aging in air, or during post-growth processing steps. While crystalline defects are typically considered undesirable, controllable fabrication of nanometer-scale pores in 2D TMDs are highly desirable for energy, filtration, and sensing applications, as will be described in greater detail in Chapter 6. Due to the hexagonal nature of the TMD crystal structure, nanopores in TMDs often tend to possess 3-fold or 6-fold symmetries, terminated by low-index facets such as the zigzag (ZZ) or armchair (AC) edges (Figure 1-4).

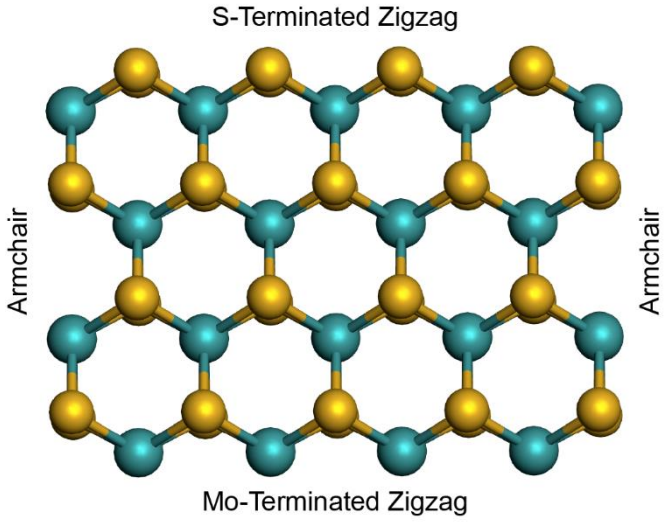

Figure 1-4. ZZ and AC edges of 2D TMDs.

1.2 **Thesis outline**

In this thesis, we explore the effects of defect-driven processing of 2D TMD semiconducting materials. We first demonstrate how the control of substrate temperature in CVD can allow for diffusion-mediated synthesis of heterostructures and alloys in 2D TMDs. We then determine the scope of this diffusion-mediated process by identifying a defect-driven atomistic model that is corroborated by our synthesis of chemically-graded alloys in which the composition is determined by the defect distribution. Next, we expand the control of defect placement by developing a laser-based technique for direct-write defect patterning that translates into bespoke heterostructure patterning. Finally, we investigate the application of 2D TMD defect processing to the field of nanoporous membrane technology.

Chapter 2 introduces the experimental methods used in this thesis, focusing on sample preparation and characterization. Sample preparation includes 2D TMD crystal isolation by mechanical exfoliation, crystal growth by chemical vapor deposition, and methods of crystal transfer from native SiO_2 substrates to transmission electron microscopy (TEM) grids. Sample characterization includes a variety of techniques utilizing lasers, scanning probes, and electron

beams to map the local properties of these samples. The techniques of Raman spectroscopy, photoluminescence (PL) spectroscopy, atomic force microscopy (AFM), and scanning transmission electron microscopy (STEM) will form the basis of our experimental investigation and will therefore be discussed in detail.

Chapter 3 investigates how substrate temperature in the second step of a two-step CVD process affects compositional configuration in the (Mo/W)S_2 material system. Lateral heterostructures of MoS_2-WS_2 and alloys of $Mo_xW_{1-x}S_2$ are presented following otherwise comparable CVD procedures. We present Raman and PL spectroscopy characterization of the composition as a function of position. We propose a diffusion-mediated process to explain the observations.

Chapter 4 continues the investigation of the nature of the proposed diffusion-mediated process. By replacing the first CVD step of the two-step process with mechanical exfoliation of either MoS_2 or WS_2, we investigate the limitations of the diffusion-mediated process in an attempt to understand the mechanism. We present an energetically favorable atomistic model proposing that the transition metal diffusion process is driven by a heterogeneous distribution of point defects. This model is corroborated by the synthesis of a composition-graded $Mo_xW_{1-x}S_2$ alloy in which the final-stage spatial distribution of transition metal atoms correlates with intermediate-stage distribution of point defects. Additionally, we analyze the spatially heterogeneous PL spectra of these graded alloy crystals to correlate local optical properties with the local composition.

Chapter 5 investigates methods of controlling the intermediate-stage distribution of point defects to enable direct-write defect patterning that translates into bespoke heterostructure patterning. Utilizing a laser annealing technique, we demonstrate the ability to locally induce

defects. These defects serve as preferred sites for heterostructure formation during subsequent CVD growth. Using this technique, we are able to create arbitrarily patterned MoS_2-WS_2 heterostructures.

In Chapter 6, we turn our attention to defect processing for nanoporous 2D TMD membrane applications. We present series of atomically resolved STEM images of nanoporous 2D TMDs throughout intermittent *in situ* vacuum annealing. We examine both the evolution of the nanopore edge structure as well as the rate of growth as functions of annealing temperature. We corroborate these experimental findings with Monte Carlo modeling and the presentation of a fundamental mathematical framework.

Finally, in Chapter 7 we will conclude this thesis by summarizing the important scientific contributions of this work and suggesting future directions of research in this field based on the results presented here.

Chapter 2: Experimental Methods

The experimental work presented throughout this thesis can be divided into two classes: sample synthesis/preparation and sample measurement. The first section of this chapter focuses on various methods of sample preparation including the simple top-down method of isolating TMD monolayers by mechanical exfoliation and the more versatile bottom-up method of growing crystals by CVD. The advantages, disadvantages, and important considerations of each of these techniques will be discussed. The ability to transfer crystals from their native substrate to new substrates is critical to enable investigation by TEM. Best known practices and important considerations for crystal transfer will be discussed. The second section of this chapter focuses on various methods of sample measurement utilizing lasers, scanning probes, and electron beams to map the local properties of these samples. The techniques of Raman spectroscopy, PL spectroscopy, AFM, and STEM will form the basis of our experimental investigation and will therefore be discussed in detail.

2.1 **Preparation of two-dimensional crystals**

2.1.1 Mechanical exfoliation

The fundamental principle of mechanical exfoliation of layered materials such as TMDs is the utilization of weak inter-layer vdW bonds to separate layers from each other. In an ideal scenario, a single crystal containing m layers can be divided into two equal parts $\log_2 m$ times to produce m separate crystals each containing a single layer. In reality, crystals rarely divide evenly, therefore resulting in some thicker crystals and some thinner crystals (Figures 2-1 and 2-2). After a sufficiently large number of divisions, it becomes statistically likely that some of the thinner crystals will reach monolayer thickness and will no longer be capable of dividing.

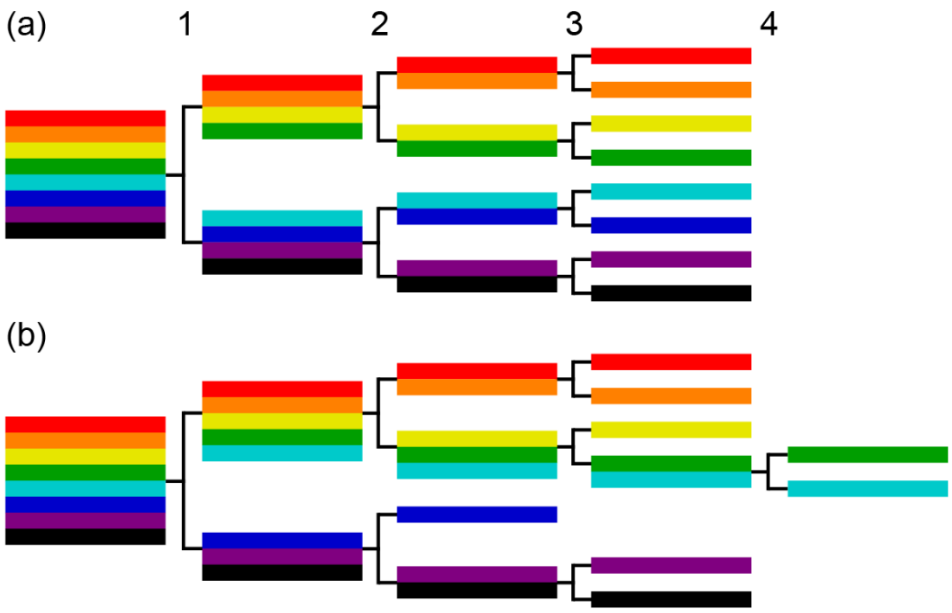

Figure 2-1. (a) Ideal (*i.e.*, $\log_2(m)$) and **(b)** more realistic layer isolation pathways by mechanical exfoliation. Mechanical exfoliation often results in a distribution of layer numbers.

To perform the technique of mechanical exfoliation, one must begin with a pure bulk crystal of the desired 2D layered material. These crystals can originate from synthetic sources such as chemical vapor transport growth of bulk crystals or from natural sources such as mining. A small piece (≤1 mm^2) is placed on laboratory-grade adhesive (*e.g.*, Nitto SPV 224PRM or Nitto 3195MS). The tape is iteratively folded in half and peeled apart to thin the crystal into isolated layers. Following ~5 exfoliation iterations, the adhesive can be applied to a cleaned SiO_2 substrate and delaminated. This step may result in additional layer exfoliation, but will also result in the transfer of full crystals from the adhesive to the SiO_2 substrate. At this point, the mechanical exfoliation process is complete and the researcher must search across the substrate to locate TMD crystals and determine their thicknesses. The majority of transferred crystals will be multi-layer, but, with practice, this technique can reliably yield multiple monolayer crystals on the order of tens of μm in length (Figure 2-2).

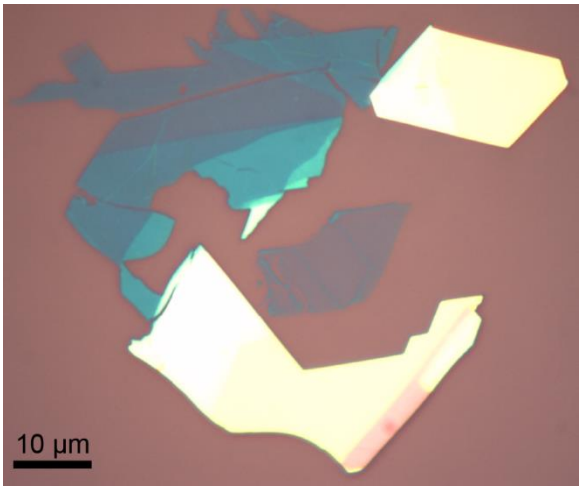

Figure 2-2. WS_2 crystal example of the variety of crystal thicknesses achieved following mechanical exfoliation ranging from monolayer (light purple, center) to few-layer (blue, upper left) to multi-layer (yellow, bottom and upper right).

The main advantages of mechanical exfoliation as a method of producing monolayer TMD crystals are simplicity, versatility, and crystal quality. In terms of simplicity and versatility, a seminal paper in the field noted that "the whole procedure takes literally half an hour to implement" and can be easily and equally applied to a wide range of layered crystalline materials such as BN, MoS_2, $NbSe_2$, $Bi_2Sr_2CaCu_2O_x$ and graphite.[71] The quality of mechanically exfoliated crystals, measured by point defect density, is a function of the method of production. Whereas CVD-grown crystals are nucleated and grown from the vapor phase on the time scale of minutes, and are therefore susceptible to high defect densities due to fluctuations in local concentrations and kinetic phenomena, mechanically exfoliated crystals are produced on much longer time scales (*e.g.*, hours for synthetic bulk crystals and geological time scales for natural minerals) and therefore tend to equilibrate to thermodynamically preferred stoichiometries and defect densities.

The main disadvantages of this technique are the prevalence of organic residue, the lack of scalability, and the lack of capabilities to achieve complex structure formation. The organic residue (*i.e.*, glue) on the SiO_2 substrate and exfoliated TMD crystals comes from the adhesive as well as adsorbates from the environment.[72] Appropriate choice of adhesive can limit the amount

of organic residue found on the substrate and crystals and cleaning steps can be taken to remove it.[73] However, these cleaning steps much be chosen carefully to avoid damage to the TMD crystal. The scalability issues of mechanical exfoliation are largely irrelevant for academic research, but pose a fundamental limitation to the commercialization of any technology dependent upon this technique. Most mechanically exfoliated TMD crystals used in research have been produced manually by processes that involves several poorly controlled parameters (*e.g.*, layer number of initial crystal and force of adhesive peeling). While steps can be taken to automate the exfoliation process, it will likely never achieve the level of reproducibility and control attainable by bottom-up methods such as CVD. Lastly, top-down methods such as mechanical exfoliation can break both chemical and vdW bonds, but cannot form chemical bonds. Therefore, while this technique is adequate for isolation of monolayers of pre-defined chemistries, it is incapable of producing complex chemically bonded structures through advanced processing and patterning steps. When simplicity and quality are desired, mechanical exfoliation is effective and efficient. However, for advanced manufacturing, alternative techniques such as CVD must be pursued.

2.1.2 Chemical vapor deposition

For wafer-scale fabrication of TMD-based electronic and optoelectronic devices, the use of a scalable technique such as CVD is necessary. The fundamental principle of CVD involves the vaporization of multiple precursor materials that will then adsorb on the target substrate and chemically react with each other to nucleate and grow crystalline material. This technique has been applied toward the synthesis of a large and growing list of TMDs and other 2D materials as well as the growth of heterostructures and alloys.[74–83]

A typical set-up for a CVD system used for the growth of 2D TMDs involves the placement of precursor powders into alumina boats that are loaded into a quartz tube inside a tube furnace (Figure 2-3). A carrier gas will flow in from the upstream end of the tube to carry the vaporized precursor powders downstream toward the substrate. The effluent vapor will exhaust out of the downstream end of tube. This process contains a large number of tunable parameters which can make it difficult to optimize but can also enable a high degree of control. The key parameters can be grouped into the following categories which will be discussed in detail below: gas, temperature, materials selection, and timing.

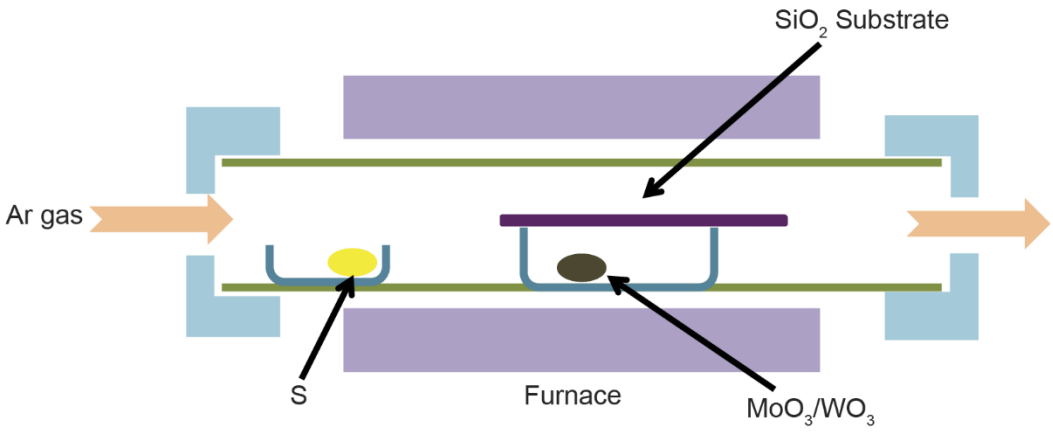

Figure 2-3. Schematic of a typical CVD furnace set-up identifying the relative locations of key components.

2.1.2.1 CVD gas parameters

The role of the input gas in a CVD system is to act as a carrier of the precursor vapor to the substrate and to define the environmental conditions in which the chemical and physical processes occur. There are typically three main CVD parameters related to the input gas: chemical choice, background pressure, and flow rate.

Ar and N_2 are commonly chosen input gases due to their relative inertness, low cost, and ease of handling. H_2 gas is a common additive (*e.g.*, 10-15% mixture with Ar or N_2) to create a

reducing environment favorable for growth of WX_2.[84–86] Conversely, H_2O vapor has been demonstrated as useful additive to rapidly neutralize a H_2-generated reducing environment and create an oxidizing environment to promote growth of MoX_2. By alternating between reducing and oxidizing environments, multi-domain lateral heterostructures have been demonstrated with nearly atomically sharp interfaces.[85] In the CVD experiments discussed throughout this thesis, Ar is used as the input gas.

The background pressure of the system controls the vapor transport mechanism between the precursor source and target substrate. The mean free path is calculated from the total pressure of the system by:

$$\lambda\ (cm) \approx 5x10^{-3}/P\ (Torr) \qquad 2\text{-}1$$

Since our CVD system does not operate on the principle of "line of sight" deposition, the background pressure should be chosen such that the mass transport is viscous (*i.e.*, diffusive) instead of molecular (*i.e.*, ballistic) (Figure 2-4). Under viscous transport conditions, molecular collisions are expected and and the vapor flow outside the boundary layer of the substrate is assumed to be convective. Gas diffusivity is related to total pressure as well as gas temperature by:

$$D_{gas} \propto T^{\frac{3}{2}}/P \qquad 2\text{-}2$$

where gas temperature can be approximated by the temperature of the CVD zone. While some 2D TMD research has been conducted using low-pressure CVD to increase D_{gas} and thereby improve mass transport to the substrate,[38,44,86–93] a significant amount of research including all of the results presented in this thesis has been conducted at atmospheric pressure.[27,35,36,78,94–98]

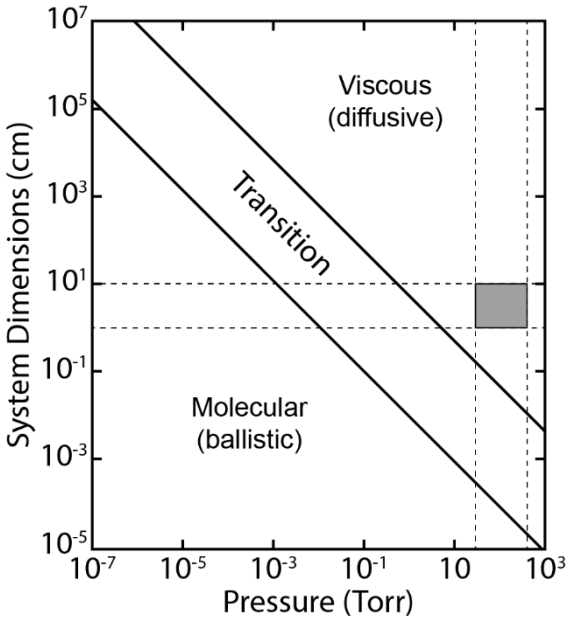

Figure 2-4. Gas flow regimes as a function of system dimensions and pressure. The approximate range of operating conditions reported throughout this thesis corresponds to the region within the grey rectangle in the viscous regime. Figure adapted from Ref. 99.

Whereas the background pressure controls the mass transport between the precursor source and target substrate, the flow rate dictates the behavior in the immediate vicinity of the substrate. With an immobile substrate and a non-zero flow rate, the boundary conditions of mass transport result in a stagnant film boundary layer (Figure 2-5):

$$d_{sf} \approx \sqrt{\mu x/\rho U} \qquad 2\text{-}3$$

where μ is the viscosity of the gas, x is the distance from the leading edge, ρ is the density of the gas, and U is the bulk velocity of the gas. From the boundary layer thickness and gas diffusivity, the gas phase mass transport coefficient can be calculated as:

$$h_G = D_G/d_{SF} \qquad 2\text{-}4$$

In the bulk gas, the concentration of precursor vapor can be approximated as uniform and is determined by the precursor vaporization rate. Within the boundary layer, the concentration will

decrease as there is a net flux of precursor out of the bulk gas and onto the substrate where it is deposited. This can be modeled by a mass transport flux:

$$F_1 = h_G(C_G - C_S) \quad 2\text{-}5$$

where C_G is the bulk gas concentration and C_S is the gas concentration at the substrate interface, and a reaction flux:

$$F_2 = k_S C_S \quad 2\text{-}6$$

where k_S is a surface reaction rate constant which is dictated by adsorption and desorption rates that will be expanded upon in Section 2.1.2.2. Combining these equations together, the mass transport-limited growth regime is related to the macroscopic gas flow rate processing parameter by $F_1 \propto U^{\frac{1}{2}}$, indicating that higher flow rates result in higher mass transport flux.

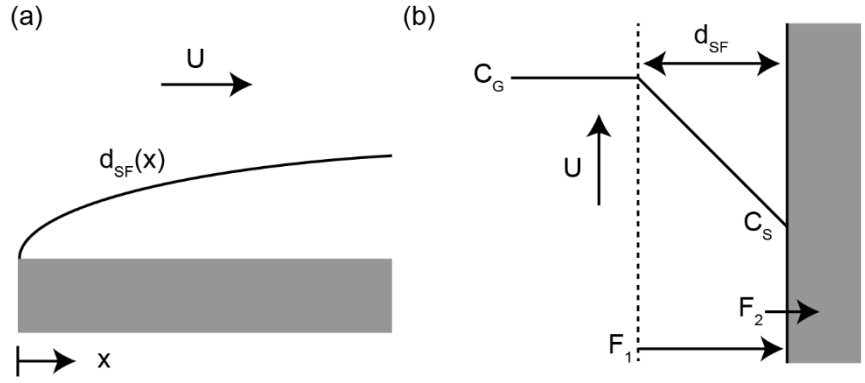

Figure 2-5. Schematics of **(a)** the stagnant film boundary layer, **(b)** concentration profile, and fluxes.

2.1.2.2 CVD temperature parameters

The three thermally-sensitive components of the CVD growth of 2D TMDs are the chalcogen precursor, metal precursor, and substrate. In a one-zone furnace (see Figure 2-3), it can be difficult to de-couple the temperatures of these three components, often resulting in identical substrate and metal precursor temperatures and slightly lower chalcogen precursors depending

on the exact placement of the that respective alumina boat relative to the center of the furnace. Conversely, in a three-zone furnace (Figure 2-6), each component can be placed in its own heating zone, thereby allowing independent control of the temperature parameter for all three components. For additional temperature control, a push rod and pair of magnets can be used to change the position of the chalcogen precursor boat throughout the CVD growth process.

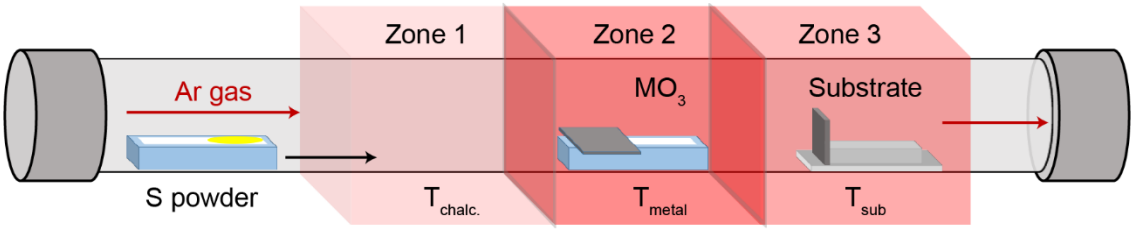

Figure 2-6. Schematic of a three-zone CVD furnace set-up demonstrating the ability to achieve thermal de-coupling of each precursor as well as the substrate.

The chalcogen precursor and metal precursor temperatures are relatively straightforward parameters. In each case, a growth temperature should be chosen to allow for vaporization of the precursor powder at a steady rate described by:

$$R_e \propto T^{-\frac{1}{2}} exp\left(-h_{vap}/k_B T\right) \qquad 2\text{-}7$$

This temperature is typically in the range of 120-200 °C for S and Se precursor powders,[31,100–102] 650-800 °C for MoO_3 precursor powder,[27,49,63,75,78] and 900-1100 °C for WO_3 precursor powder.[80,86,95,102]

Due to the relatively high temperature necessary for WO_3 vaporization and the consequent discrepancy in the vaporization rates of MoO_3 and WO_3 for any fixed temperature, there has been an effort to identify ways to lower the W precursor growth temperature to facilitate the controlled synthesis of mixed-metal alloys and heterostructures. One method that is becoming increasingly popular is mixing of alkali metal halide additives (*e.g.*, NaCl) to the transition metal

precursor powder to volatilize the precursor and reduce its vaporization temperature.[96,103–105] While this method is effective, it also places additional emphasis on the importance of controlling relative precursor vaporization rates. That is, if the metal precursor CVD zone temperature is not adequately adjusted to the vaporization temperature, accounting for any possible additives, then the metal precursor will vaporize at a rate that is incompatible with the vaporization rate of the chalcogen precursor.

The relative vaporization rates of the chalcogen and metal precursors affect the vapor concentrations of those precursors and the eventual stoichiometry of the grown crystal. As the M:X ratio of the MX_2 TMD deviates from 1:2, the crystal will become rich in one precursor and deficient in the other. The hexagonal crystal structure implies that a crystal with a balanced stoichiometry will be macroscopically hexagonal with three chalcogen-terminated edges and three metal-terminated edges. To accommodate imbalances in stoichiometry, the crystal will become macroscopically triangular, comprised exclusively of the three ZZ edges terminated by the element in surplus. In the extreme case, this imbalance can eventually lead to high probabilities of defect formation as well as undesirable dendritic morphologies.[94,106]

When the substrate temperature can be de-coupled from the metal vaporization temperature, as is the case in multi-zone furnaces, greater consideration must be given to this parameter as it affects the kinetics of the precursor flux as well as the nucleation and growth of the TMD crystal. As described earlier in Section 2.1.2.1, the two fluxes that describe precursor deposition on the substrate are the mass transport flux and the chemical reaction flux. The mass transport flux is sensitive to gas flow rate, but also contains a temperature component through the gas diffusivity equation. The temperature relation of crystal growth in the mass transport-limited regime is therefore modeled as $F_1 \propto T_{substrate}^{3/2}$. This regime exists at high substrate temperatures and/or

low flow rates and is relatively insensitive to temperature and relatively sensitive to flow rate (Figure 2-7).

In addition to mass transport flux, the concentration gradient in the boundary layer is also described by the surface reaction flux (Equation 2-6). As a thermally activated process, a first-order equilibrium reaction rate can be modeled by as:

$$k_s = k_0 \exp(-E_a/k_B T_{substrate}) \quad \text{2-8}$$

Consequently, when the gas flow rate is high and/or the substrate temperature is low and the system is operating in a reaction-limited regime, the reaction flux and therefore also the growth rate are related to the substrate temperature by $F_2 \propto \exp(-1/T_{substrate})$.

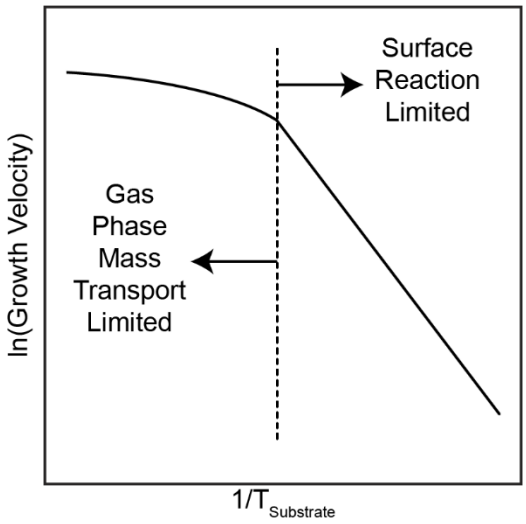

Figure 2-7. Schematic plot of the temperature dependence of the growth velocity in different growth regimes.

The surface reaction flux refers to the difference between adsorption and desorption of the precursor vapor. This non-zero difference results in the accumulation of adsorbed material that can undergo a variety of temperature-dependent phenomena including surface diffusion, adatom clustering (*i.e.*, crystal nucleation), and crystal growth. Adatoms will diffuse across the surface of

a substrate by a series of atomic jumps from potential energy well to potential energy well. Those jumps will collectively form a random walk in the absence of an energy gradient and a correlated walk in the presence of an energy gradient. The temperature-dependent jumping rate is modeled as:

$$\Gamma = \nu \exp(-E/k_B T_{substrate}) \quad \text{2-9}$$

where ν is the attempt frequency derived from a simple harmonic oscillator model and E refers to the energy barrier between neighboring potential wells. The 2D surface diffusion coefficient can be calculated from jumping rate as:

$$D = \Gamma a^2/4 \quad \text{2-10}$$

where a is the distance per jump.

As the number of atomic jumps and the number of adatoms increase, the probability of adatom-adatom interaction also increases. As adatoms interact with each other, they will tend to form thermodynamically stable clusters (*i.e.*, nuclei) of atoms. The temperature-dependent steady-state distribution of the n number of clusters containing N atoms can be modeled as:

$$n_N/n_1 \approx \exp(-\Delta G_N/k_B T) \quad \text{2-11}$$

Approximating a TMD nucleus as a 2D disc, the free energy can be modeled as:

$$\Delta G_{r,\gamma} = \pi r^2 z \Delta G_{vol} + \pi r^2(\gamma_c + \gamma_{sc} - \gamma_s) + 2\pi r z \gamma_{c,edge} \quad \text{2-12}$$

where G is free energy, r is radius, z is thickness, γ is surface energy, and the surface energy subscripts refer to the crystal-air, substrate-crystal, and substrate-air planar interfaces and the crystal-air edge interface, respectively.[32] Beyond the critical cluster radius where $\partial \Delta G/\partial r = 0$, it

becomes energetically favorable for nuclei to continue to grow into larger crystals. Optimal CVD growth should operate in a substrate temperature range that allows for a sufficient amount of surface diffusion of adatoms to occur between adsorption and desorption events to allow nuclei to form and grow to the critical size necessary for stability and continued growth. Adjustments within this process parameter range will affect nucleation density, which then affects grain size.

On a properly cleaned substrate, deposited TMD material can either nucleate a new monolayer crystal on the substrate, attach to the edge of an existing TMD crystal to contribute to crystal growth, or nucleate a new layer on top of an existing TMD crystal. Similarly, in heterostructure formation, new chemical domains can also nucleate by attaching to the edge of an existing TMD crystal to form a lateral heterostructure or on top of existing TMD crystals, which would form vertical heterostructures. The kinetics of these possible processes are dictated by substrate temperature and the relative surface energy values of the relevant TMD and substrate interfaces through the surface diffusion, nucleation, and free energy model equations discussed earlier (Equations 2-10 through 2-12, respectively) and demonstrated in Figure 2-8. In the case of monolayer *vs.* multilayer growth of a single TMD chemical domain[32] as well as lateral *vs.* vertical TMD heterostructure growth,[24] lower substrate temperatures tend to favor lateral monolayer crystal growth with a TMD-substrate planar interface whereas higher substrate temperatures tend to favor vertical multilayer growth with a TMD-TMD planar interface.

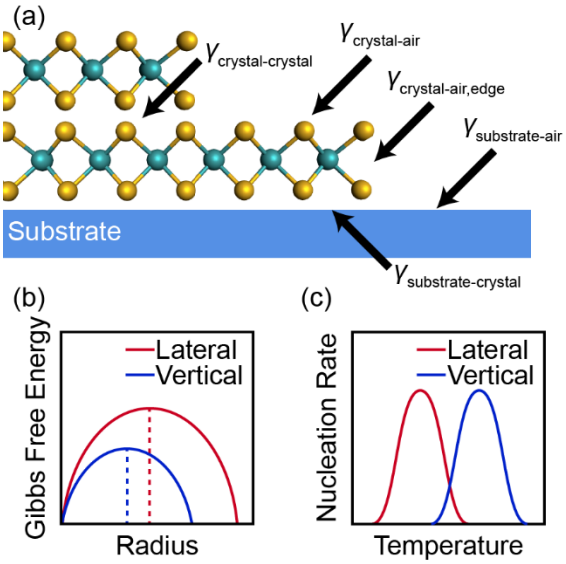

Figure 2-8. Energetics for calculating critical nucleation size and monolayer vs. multilayer growth. Figure adapted from Ref. 32.

2.1.2.3 CVD materials selection

The materials selection requirements for CVD growth of TMD materials involve the choice of a chalcogen precursor, transition metal precursor, substrate, and any possible additives (*e.g.*, NaCl discussed in Section 2.1.2.2) to aid the growth process. In the CVD experiments discussed throughout this thesis and in the majority of the literature in the field, the chalcogen precursor powder is the elemental solid powder of the chalcogen material (*i.e.*, S, Se, or Te) whereas the transition metal precursor is in the form of a metal trioxide (*e.g.*, MoO_3 or WO_3). Other demonstrated transition metal precursors include ammonium-based precursors (*e.g.*, $(NH_4)_2MoS_4$),[77,107] elemental metal films,[108] and metal chlorides (*e.g.*, $MoCl_4$).[109] Precursor selection can also vary by the selection of a non-CVD deposition technique such as metal-organic CVD and molecular beam epitaxy. Metal-organic CVD has been demonstrated using metal hexacarbonyls (*e.g.*, $Mo(CO)_6$), diethyl sulfide (*i.e.*, $(C_2H_5)_2S$), and dimethylselenium (*i.e.*, $(CH_3)_2Se$).[40,110–112] Molecular beam epitaxy of 2D TMDs has also been demonstrated using high-purity elemental sources.[113–118]

In the CVD experiments discussed throughout this thesis and in the majority of the literature in the field, polished silicon wafers are used as substrates. These wafers are typically 150 mm diameter as-purchased, then manually cleaved into smaller pieces to fit into the 1" or 3" CVD quartz tubes. Alternative growth substrates include other crystalline wafers (*e.g.*, sapphire)[58,86,95,117,119–123], molten glass,[124] and pre-deposited layered (*e.g.*, graphene, mica),[77,87,112,121,125–127].

The (0001) plane of c-sapphire is hexagonally arranged, matching the crystal symmetry of TMDs, with a lattice constant that is almost exactly 50% larger than that of MoS_2 (4.814 Å vs. 3.212 Å). Therefore, despite its higher cost, there has been growing interest in the use of highly polished sapphire substrates with atomically smooth terraces for CVD of TMDs in an effort to control film orientation to enable the synthesis of large-area, uniform, single crystal, monolayer crystals. As TMD nuclei begin to grow, there is a thermodynamic driving force to be in registry with the substrate, adopting a 3-on-2 superstructure at either 0° or 60° orientations with respect to the crystal symmetry of the sapphire. As crystals with perfectly matched orientations impinge upon each other during crystal growth, the crystals should seamlessly stitch together to form a continuous and defect-free film.[119] This phenomenon has also been reported when using monolayer single-crystal films of other hexagonal 2D materials as substrates.[112,127]

2.1.2.4 CVD timing parameters

The relevant timing parameters involved in CVD growth recipes are the duration at the target growth temperature, the rate and duration of furnace heating, and the rate and duration of furnace cooling. As long as there is a sufficient supply of precursor vapor and there are empty sites on the surface of the substrate for adsorption, crystal growth will continue. As the monolayer TMD film occupies a larger fraction of the substrate surface area, multilayer nucleation and growth

also becomes increasingly likely.[110] However, the use of finite supplies of precursor powder loaded into the CVD system prior to the start of the growth process indicates that precursor vapor concentration will not remain indefinitely uniform. As vapor concentration begins to decrease, TMD decomposition may begin, resulting in crystal defects, pore formation, and eventually complete crystal disintegration.[128] Balancing these factors, an appropriate target growth temperature duration is typically on the order of 5-30 min.

The heating rate of the CVD growth process is dictated by the capabilities of the furnace and is typically ~15°C/min. Faster heating helps to reduce the amount of time that the substrate spends at high temperatures, which may be beneficial if there are temperature-sensitive materials pre-deposited on the substrate. Additionally, faster heating narrows the time window between the onset of vaporization and the start of the target growth temperature duration. However, faster heating also leads to greater overlap between the intermediate-temperature outgassing period and the target growth period, thus potentially resulting in the presence of residual outgassed material during the growth process. Lastly, one must also consider that the chalcogen precursor, metal precursor, and substrate must all be heated simultaneously, usually to different target temperatures, and should ideally reach their respective target temperatures simultaneously. With lower heating rates, the margin for error and the ability to make impromptu adjustments are greatly improved. As discussed at the beginning of Section 2.1.2.2 and illustrated in Figure 2-6, the use of a magnet and push rod can improve the reproducibility of simultaneously reaching the target temperature by storing the chalcogen precursor boat outside of the furnace and only introducing it into its target zone once the metal precursor and substrate have reached their respective target temperatures.

The cooling rate of the CVD growth process is typically designed to be as fast as possible. At the end of the target growth temperature duration, the CVD furnace is turned off. As soon as safely possible, the hinged lid of the furnace is opened allowing for free conduction, convection, and radiation of heat into the lab environment. This process can be expedited through the use of a fan pointed at the furnace to increase convection. After 30-45 min, the system is usually cool enough to allow for the removal of the substrate.

2.1.3 Crystal transfer

For several characterization techniques and processing procedures, it may be necessary to transfer samples from their native substrate to a new substrate. The most notable example applicable to the work presented in this thesis involve transferring 2D TMDs onto TEM grids. The general strategy of all 2D TMD crystal transfer methods involves four steps (Figure 2-9): (1) attach a temporary second substrate to the exposed surface of the sample, (2) remove the native substrate, (3) attach the new permanent substrate along the surface that formerly connected the sample to the native substrate, and (4) remove the temporary substrate.[129–132]

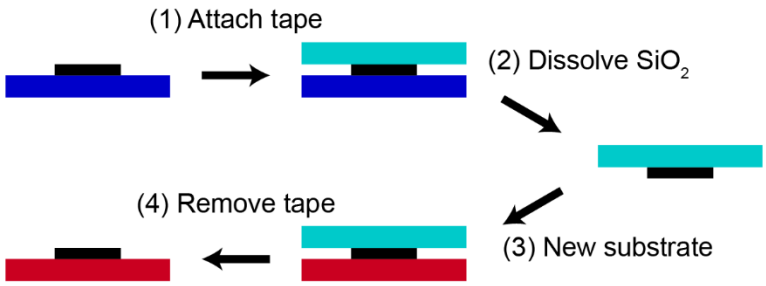

Figure 2-9. Schematic process of crystal transfer steps.

In the first step of the transfer process, the temporary second substrate used throughout this thesis is poly(methyl methacrylate) (PMMA). PMMA has the advantages of processability, transparency, and flexibility. The processability of PMMA means that it can be spin-coated onto a SiO_2 substrate containing 2D TMDs and uniformly and conformally coat the sample. The

transparency allows the sample(s) to be located and monitored throughout the transfer process. The flexibility of PMMA eases the process of attaching a new substrate in the third step. A typical PMMA attachment process involves the use of 495-950K molecular weight PMMA in anisole that is spin-coated at 3000 rotations per minute (RPM) for 1 min and then annealed at 70-180°C for 2-5 min. Mechanical exfoliation tape (*e.g.*, Nitto SPV 224PRM or Nitto 3195MS) is then applied to the exposed surface of the PMMA to provide mechanical support. Prior to its application, a small window is cut in the tape (Figure 2-10a) and the tape is placed such that the target sample is centered within the window. This window eases the PMMA removal process in the fourth step (Figure 2-10b).

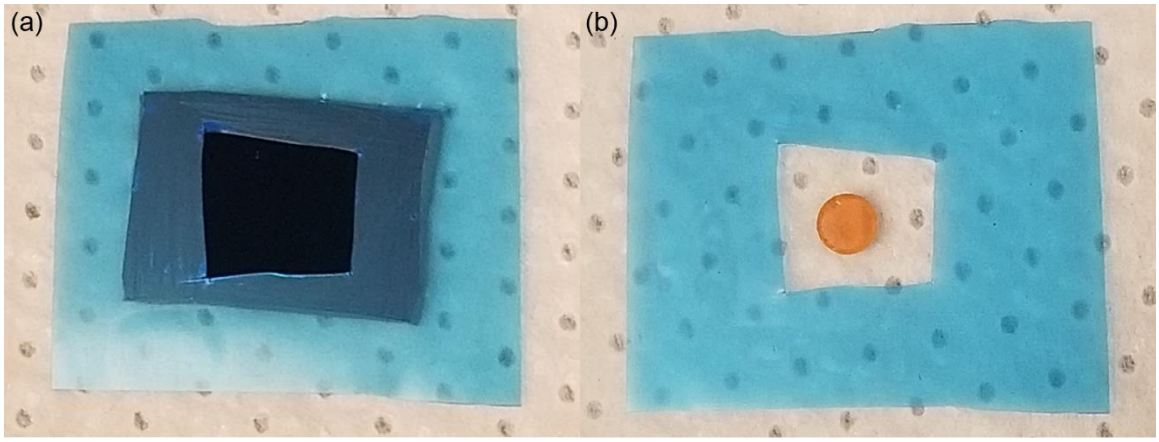

Figure 2-10. Photographs of **(a)** transfer step 1 (*i.e.*, aligned placement of tape on the substrate) and **(b)** transfer step 3 (*i.e.*, aligned placement of crystal/tape structure on new TEM grid substrate).

The second step of the crystal transfer process involves removing the SiO_2 substrate by immersion in a strong basic solution (*e.g.*, KOH). The molarity and temperature of the solution can be increased to significantly accelerate the process, but this comes with the added risk of damaging the sample. Typical SiO_2 etching involves the use of 1-2 M KOH at room temperature overnight or at 70°C for 2-3 hr. Following this process, the bare Si will sink to the bottom of the

beaker and the tape, PMMA, and crystals will be floating on the surface of the solution while still attached to each other.

In the third step of the crystal transfer process, the choice of new substrate becomes relevant. For standard TEM imaging, 3 mm Cu grids with either holey carbon or lacey carbon films are typically sufficient (*e.g.*, Ted Pella Product No 609). Depending on the selected mesh size, the individual cells of the Cu grid are typically on the range of several tens of μm. Therefore, precise manual placement of the PMMA-attached TMD crystal is very difficult, though not impossible. To improve reproducibility and increase the probability of success, sample placement on TEM grids can be assisted by the use of a stationary XYZ micromanipulator with a rigid mounted lever (Figure 2-11a). The tape, PMMA, and crystal are attached to the underside of the rigid mounted lever which is inserted between the objective lens and stage of a microscope, while the TEM grid is placed on a heating element built into the microscope stage. By changing the focus of the microscope between the crystal and the grid while slowly lowering the crystal to the grid, the relative position of the crystal on the grid can be controlled through lateral micromanipulation. With the application of heat (~100°C for 10 min) through the microscope stage heating element, the PMMA will soften and laminate onto the TEM grid (Figure 2-11b).

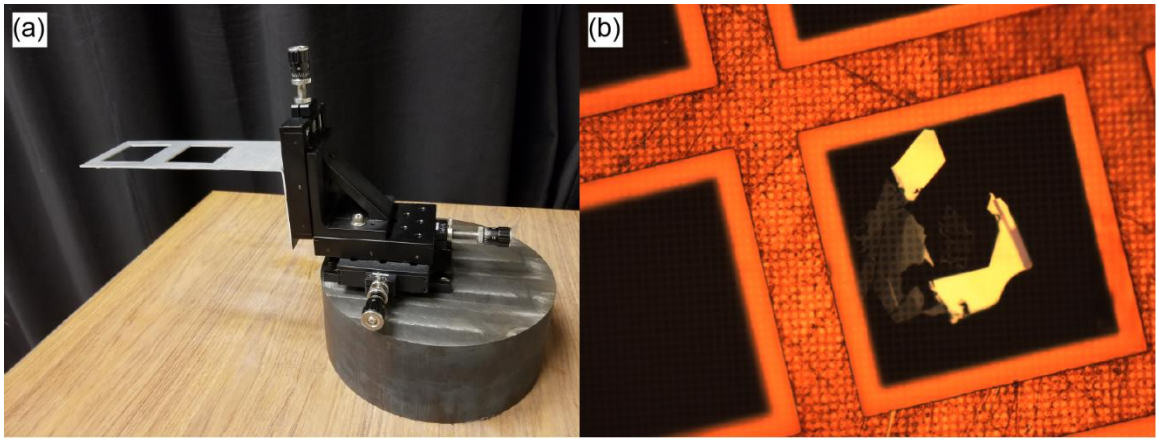

Figure 2-11. (a) XYZ micromanipulator. **(b)** Crystal transferred onto Cu TEM grid with micron-scale precision.

For the *in situ* annealing experiments discussed in Chapter 6, Protochips Fusion E-FHBS thermal e-chips TEM grids were used, requiring a modified procedure for the third step of the transfer process. Unlike Cu TEM grids, Protochips grids only contain nine electron-transparent windows, thereby increasing the necessity for the use of an XYZ micromanipulator. These 4 mm × 5.8 mm × 300 µm grids have two gold electrodes attached to opposite ends of a 700 µm × 700 µm × 120 nm ceramic film (Fig 2-12a). The application of electrical biasing to these electrodes will cause the ceramic film to rapidly heat (up to 1,000°C/ms). In the center of the ceramic film, there is a 3×3 array of 9 µm diameter windows containing a 40 nm thick film of SiN (Fig 2-12b). The grids used in the experiments discussed in Chapter 6 were modified further by focused ion beam milling of dozens of ~100 nm diameter holes through the SiN film. Upon crystal transfer, the regions of interest for microscopy were the areas of free-standing TMDs suspended over the milled SiN holes (Fig 2-12c).

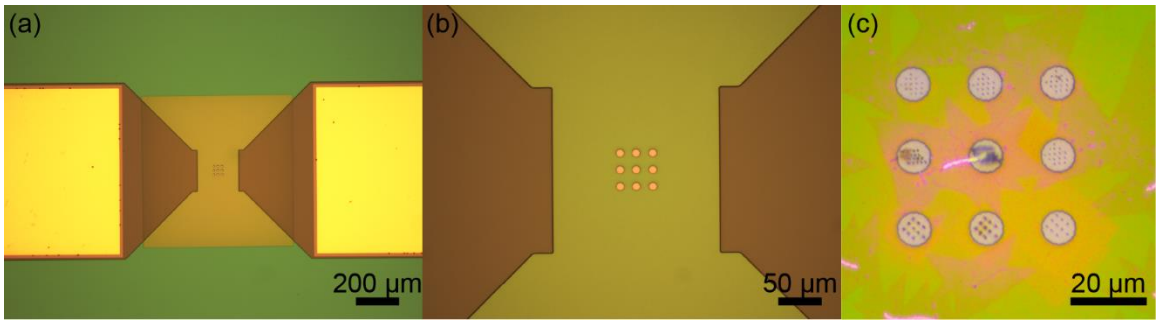

Figure 2-12. Optical microscope images of Protochips Fusion *in situ* heating TEM grids with **(a)** 5×, **(b)** 20×, and **(c)** 100× objective lens magnification. MoS_2 crystals are visible on the grid in (c) following the transfer technique described above.

The transfer process is completed by successful removal of the PMMA film and accompanying mechanical support tape. Following adequate lamination of the PMMA onto the TEM grid, the mechanical support tape can be easily removed by manual peeling. The PMMA film must then be dissolved in an appropriate solvent. Rinsing in isopropanol and then methanol removes the PMMA on the time scale of seconds, but the rapid dissolution may result in damage to the transferred crystal. For sensitive samples, the PMMA-coated TEM grid should be immersed in glacial (*i.e.*, undiluted) acetic acid for up to 24 h followed by a methanol rinse.[131] Following this process, the free-standing crystal is isolated on the TEM grid and ready for characterization.

2.2 **Characterization techniques**

There are a number of tools and techniques that can be used to characterize the various properties of 2D TMD crystals. Many of these properties relate to chemical composition, electronic band structure, and crystal structure. Throughout this section, the operating principles, relevant parameters, output data, and methods of analysis will be discussed for methods used in this work, including Raman spectroscopy, PL spectroscopy, AFM, and STEM.

2.2.1 Raman spectroscopy

Raman spectroscopy is a laser-based spectroscopic technique that measures the atomic vibrations within a sample. When a laser illuminates a sample, the photons may interact with the atomic vibrations, resulting in inelastic scattering. During inelastic scattering, energy is transferred either from the crystal to the laser photons (*i.e.*, anti-Stokes Raman scattering) or, more typically, from the laser photons to the crystal (*i.e.*, Stokes Raman scattering). The resulting scattered light will have a slightly higher or lower energy than the incident light, respectively. Since the density of states in the phonon dispersion curve is non-uniform, there will be greater counts of scattered photons at energy shifts associated with the most stable vibrational frequencies of the crystal bonds (Figure 2-13). These spectral peaks can serve as a fingerprint of the nature of the chemical bonds within the material and can provide insight into properties such as chemical composition, crystal structure, local strain, and defect density.

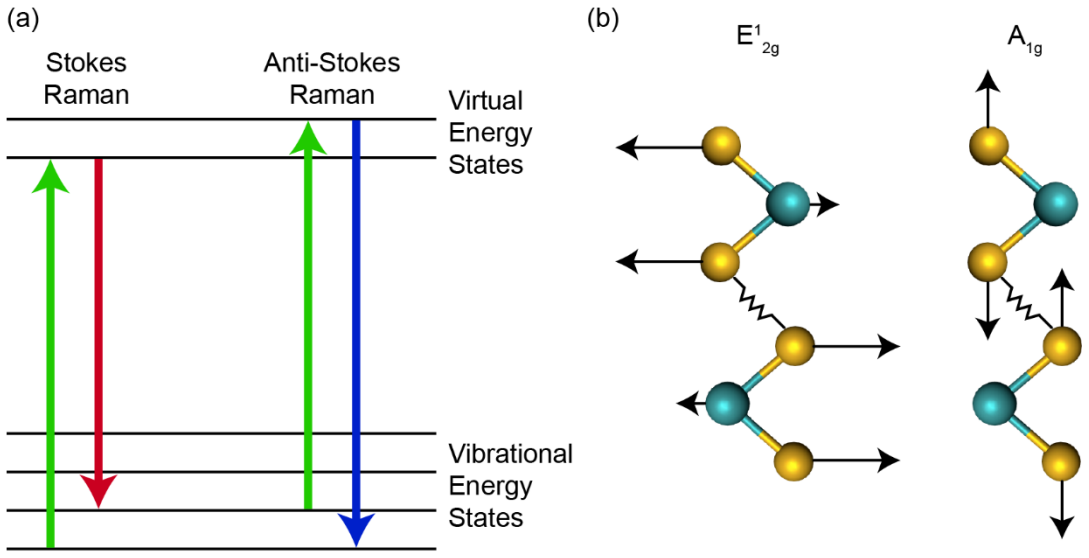

Figure 2-13. (a) Schematic of vibrational energy state transitions involved in Raman scattering. **(b)** Schematic of relevant vibrational modes in MoS_2.

The Raman spectroscopy measurements presented throughout this thesis were performed on WITec Alpha 300 R and Horiba Jobin Yvon LabRAM HR800 confocal microscopes. For

maximal resolution, the laser was focused onto the sample using a 100× objective lens, resulting in a spot size of ~1 μm in diameter.

The relevant parameters in Raman spectroscopy measurement are acquisition time, laser intensity, and laser wavelength. While higher intensities and longer acquisition times yield a greater signal-to-noise ratio, they also result in more energy transfer between the laser and crystal, due to the greater number of inelastic scattering events. This results in an increased likelihood of beam-induced damage. The sample will thermally dissipate the accumulated energy to approach equilibrium with the environment, so longer acquisition times at lower laser intensities will generally result in less beam-induced damage than an equal dose through shorter acquisition times at higher laser intensities. Typical values used throughout the experiments discussed in this thesis include ~4-9 mW laser powers and 0.5-5 s acquisition times.

The wavelength-dependent optical properties of the sample must be taken into consideration when choosing the appropriate laser wavelength. In addition to Raman scattering, photon-sample interactions include elastic scattering, transmission, absorption, and reflection. The relative amounts of each of these processes depends on the dispersion relation for the sample material and may result in certain laser wavelengths being more advantageous or disadvantageous than others. Examples of this are provided in Chapter 5. The most commonly used laser wavelength in the work reported in this thesis is 532 nm. Other wavelengths discussed are 633 and 785 nm.

In addition to the SiO_2 substrate Raman peak at 520 cm^{-1}, the most commonly discussed Raman vibrational modes in MoS_2 samples are the E^1_{2g} in-plane and A_{1g} out-of-plane modes at 385 and 403 cm^{-1}, respectively (Figure 2-14, in cyan).[133] The E^1_{2g} and A_{1g} modes are found in WS_2 at 355 and 418 cm^{-1}, respectively, as well as the $LA(M)$ mode at 174 cm^{-1} (Figure 2-14, in

red).[93] In MoS_2 samples, the spectral difference between the A_{1g} and E^1_{2g} modes is highly sensitive to crystal layer number, ranging from 18 to 25 cm^{-1} in bulk crystals, thereby serving as a useful metric to approximate sample thickness.[133] Similarly, the relative intensities of the $LA(M)$ and A_{1g} modes in WS_2 are highly sensitive to crystal quality. The background-subtracted intensity ratio $I_{LA(M)}/I_{A_{1g}}$ is a useful metric to approximate defect densities, correlating to the inverse square of the inter-defect distance.[93,134]

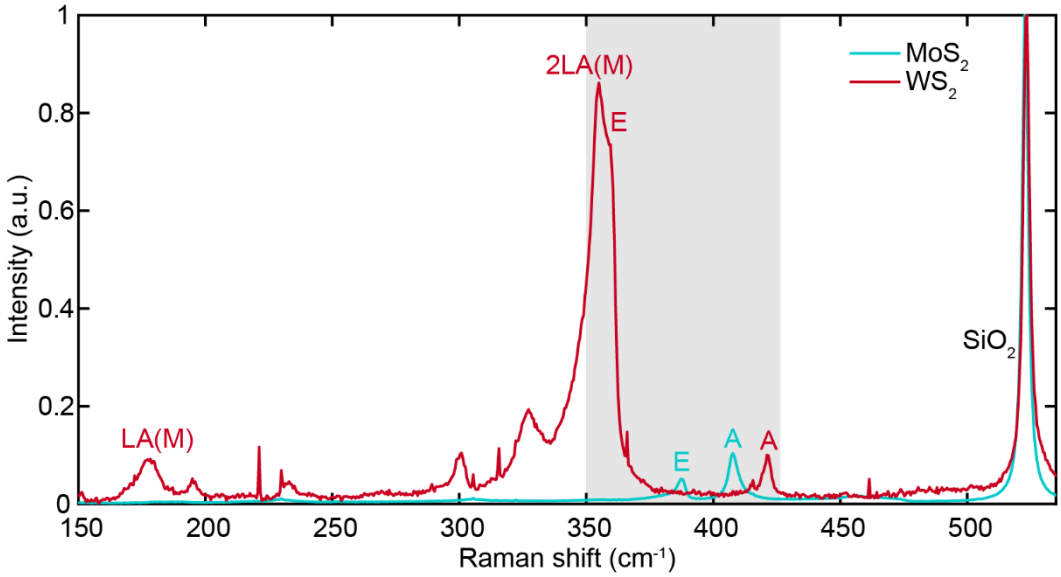

Figure 2-14. Representative Raman spectra for pure monolayer MoS_2 and WS_2. The spectral region of interest for most of the work presented in this thesis is defined by the grey rectangle.

In alloyed samples, the Raman peaks are known to significantly shift as a function of composition change. Measurement of the peak positions can therefore provide a useful metric for calculating the local alloy composition. In the case of the $Mo_xW_{1-x}S_2$ (Figure 2-15), the A_{1g} peak shifts nearly linearly with respect to composition between the MoS_2 A_{1g} value of 403 cm^{-1} and the WS_2 A_{1g} value of 418 cm^{-1}. As the transition metal composition approaches W-rich conditions, the MoS_2 E^1_{2g} peak shifts toward 370 cm^{-1}, a new peak emerges near 390 cm^{-1}, and the WS_2 E^1_{2g} peak emerges near 355 cm^{-1}.[52]

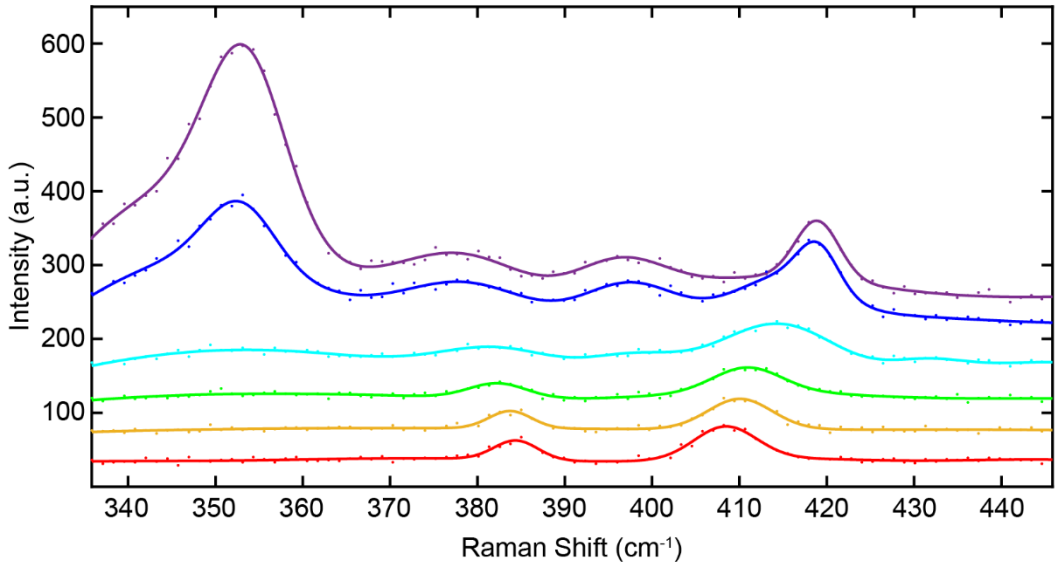

Figure 2-15. Evolution of Raman spectra in $Mo_xW_{1-x}S_2$ from $x \approx 1$ (red) to $x \approx 0$ (purple).

The majority of the Raman data presented in the experimental work of this thesis was originally collected in the form of 2D mapping. In this method, the incident laser is rastered across the sample, collecting a Raman spectrum at every pixel in 2D real space. The resulting output is a three-dimensional data cube with intensity values corresponding to spectral w, real space x, and real space y coordinates. This method allows for a variety of data representations (Figure 2-16), depending upon the relevant parameters.

A 2D cross-section of this data cube corresponding to the x and y values at a given wave number (Figure 2-16a) produces a real space image representing the spatial distribution of the intensities of a particular vibrational mode (Figure 2-16d), thereby identifying the real space location of a particular material. With some data processing, similar 2D real space maps can be produced to visualize the wave number of the local intensity maximum to not only identify the location of a particular material, but to also track composition fluctuations within that material as the spectral peaks shift, as will be demonstrated in Chapter 4. Through the generation of multiple real space maps of the intensity or position of particular Raman vibrational modes from the same

data cube, one can conduct a pixel-by-pixel analysis of, for example, the $A_{1g} - E_{2g}^{1}$ peak position difference of MoS_2 spectra to extract the spatial distribution of layer number or the $I_{LA(M)}/I_{A_{1g}}$ peak intensity ratio of WS_2 spectra to extract the spatial distribution of defect density.

Another method of dimensionality reduction by sampling involves the slicing of 2D cross-sections corresponding to one real space dimension and the spectral dimension, while holding the other real space dimension constant (Figure 2-16c). This method can provide a line scan of the spectral evolution over distance (Figure 2-16e). By sacrificing one spatial dimension, this enhances the visualization and identification of spectral fluctuations across the sample associated with, for example, composition change. In addition to alloying examples, this method can be particularly useful in the analysis of lateral heterostructures in which the spectrum will make a discontinuous jump at the chemical domain interface. Lastly, an individual spectrum at a real space (x, y) coordinate can also be extracted (Figure 2-16c and f), which can sometimes be useful for comparing the spectra between a few disjoint locations (*e.g.*, Figures 2-14 and 2-15).

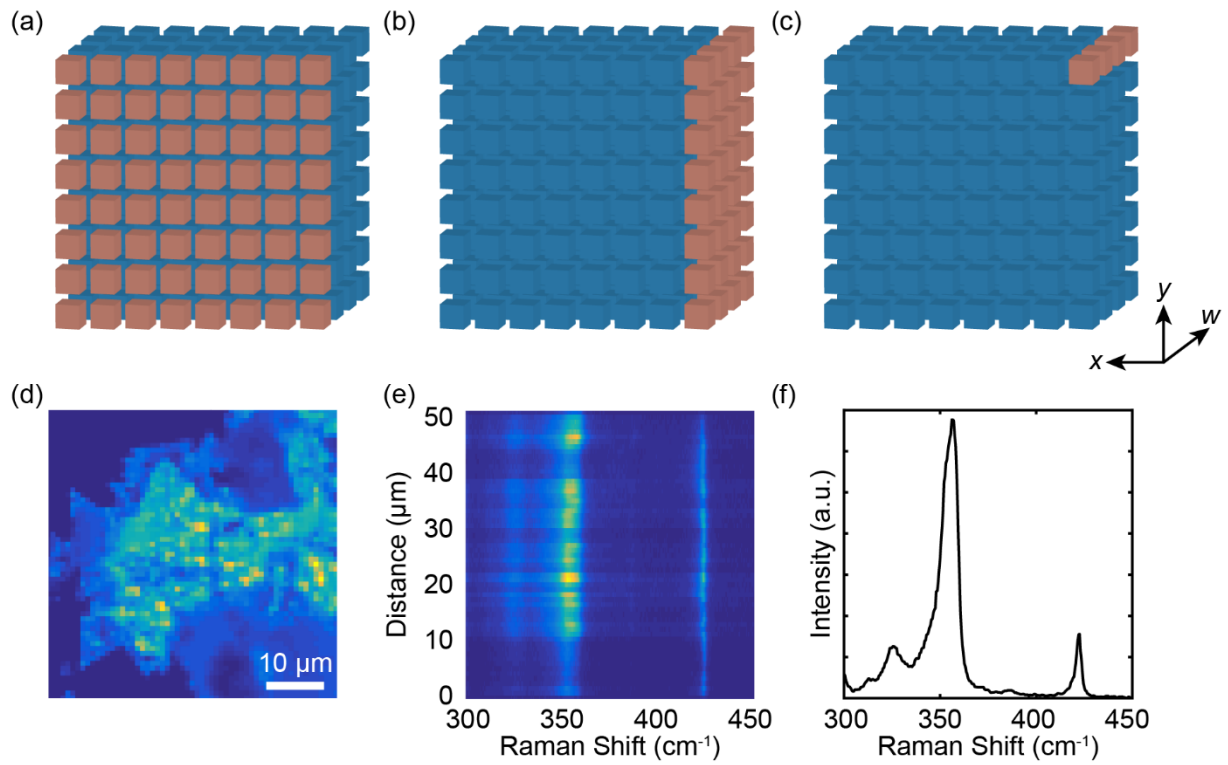

Figure 2-16. Methods of isolating components of a 3D data cube into **(a)** x-y maps at a given w, **(b)** x-w or y-w line scans at a given y or x, respectively, or **(c)** individual spectra at a given (x,y) coordinate. Corresponding examples of a **(d)** map, **(e)** line scan, and **(f)** spectrum of a WS_2 sample.

2.2.2 Photoluminescence

PL spectroscopy is a laser-based spectroscopic technique that measures the optical properties of a sample. When a laser illuminates a semiconducting material in which the energy of the laser is above the energy of the band gap of the material, the laser photons will interact with the valence band electrons in the sample, resulting in photoexcitation of the electrons into the conduction band and the production of an equal number of holes in the valence band (Figure 2-17a). In the case of materials with strong exciton binding energies, such as 2D TMDs, these excited electrons and their respective holes will stay paired together in the form of an electrically neutral quasiparticle (*i.e.*, exciton). The excited electrons and holes will relax to their respective band edges (Figure 2-17b) before recombining (Figure 2-17c and d). In high-quality materials

with clean electronic band structures and a direct band gap, this recombination process will often take the form of radiative recombination (RR, Figure 2-17c), measured as PL. The resulting spectrum of emitted light provides meaningful information regarding any property that affects the local electronic structure of a materials such as chemical composition, local strain, and defect density.

Internal quantum efficiency (IQE) describes the ratio of the emitted photons per photo-excited carrier. This fraction of total recombination events that are RR events is calculated as $\eta_{IQE} = (\frac{1}{\tau_{RR}})/(\frac{1}{\tau_{RR}} + \frac{1}{\tau_{NR}})$ where τ refers to the carrier lifetime during either RR or non-radiative recombination (NR) processes. In highly defective materials, materials with indirect band gaps, or materials with high densities of excited carriers, NR becomes more probable and IQE decreases as either τ_{RR} increases or τ_{NR} decreases. One common form of NR relevant to the work discussed within this thesis is Shockley-Read-Hall (SRH) recombination (Figure 2-17d), also known as trap-assisted recombination. In SRH recombination, the semiconducting sample contains undesirable crystal defects or impurities resulting in stable localized energy states (*i.e.*, trap states) within the band gap. Excited electrons can relax from the conduction band through these trap states to recombine with the holes in the valence band to bypass the radiative band-to-band recombination process. While the spectral position of the PL peak provides information regarding the band gap energy, a proxy for composition, the relative PL intensity provides information regarding the RR rate, a proxy for crystal quality.

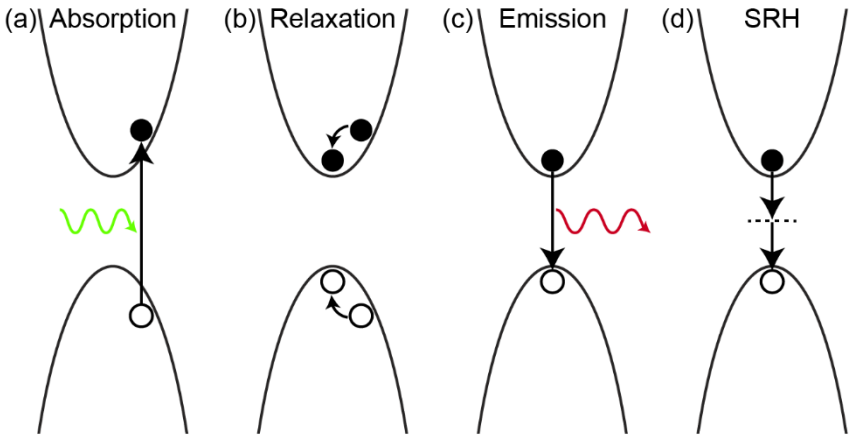

Figure 2-17. (a) Photoexcitation, **(b)** relaxation, **(c)** RR, and **(d)** SRH recombination.

Similar to Raman spectroscopy, the relevant parameters in PL include acquisition time, laser intensity, and laser energy. The considerations for these parameters are similar to those described previously for Raman spectroscopy with the notable exception that the laser energy must be greater than the band gap energy to enable for photoexcitation. A typical PL measurement involves a 0.1-0.5 s acquisition time, ~2 mW laser power, and 532 nm laser wavelength. Also similar to Raman spectroscopy, PL data is often collected as a 3D data cube, enabling 2D spatial mapping of the PL intensity and peak energy as well as line scans along a single spatial dimension and isolation of individual spectra collected at a point.

2.2.3 Atomic force microscopy

AFM is a high-resolution scanning probe technique in which a cantilever rasters across the surface of a sample. The AFM results presented throughout this thesis were conducted using the non-contact (*i.e.*, tapping) mode. In this mode, the cantilever oscillates at a fixed frequency and the atomically sharp tip at the end of the cantilever makes intermittent contact with the sample. A laser reflects off the back of the cantilever toward a photodetector to track the relative amplitude of the cantilever (Figure 2-18). As the sample height changes, the amplitude of the cantilever oscillation will change. Similarly, as the energy dissipation properties (*e.g.*, adhesiveness or

stiffness) of the sample change, the phase of the cantilever oscillation will change. While amplitude change can be trivially converted into a corresponding height map, the phase change information often does not enable unambiguous quantitative analysis as it is a convolution of a variety of factors. In the results presented throughout this thesis, changes in oscillation amplitude correspond to changes in TMD layer number whereas changes in oscillation phase are generally attributed to changes in chemical bonding (*e.g.*, chemical composition or defect density).

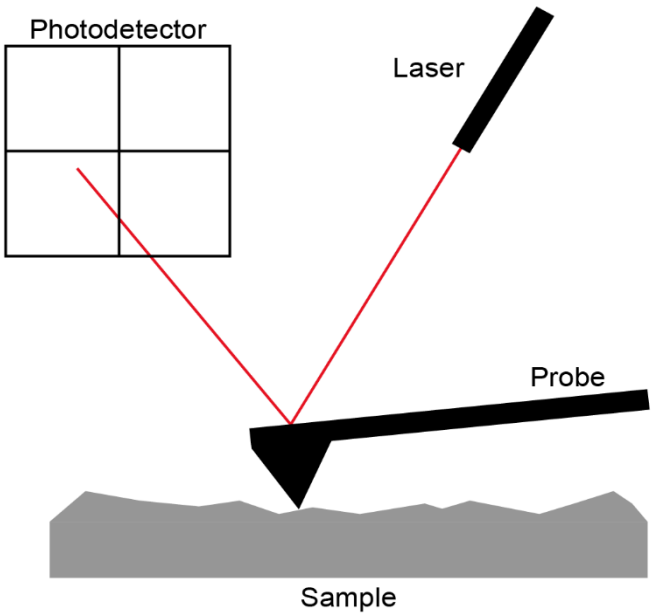

Figure 2-18. Schematic of AFM measurement.

The relevant parameters for AFM in tapping mode include the frequency, amplitude range, and amplitude set point of the oscillating cantilever, the rastering size and frequency, and the dimensions of the output file (measured in number of scanning lines and number of points per line). The optimal cantilever oscillation frequency is determined by the fundamental properties of the cantilever. For the results presented throughout this thesis, this value is typically ~300 kHz. The amplitude range and set point are typically set to 4 V and 1.35-1.70 V, respectively. The rastering size and frequency are intrinsically related through the rastering speed. At high rastering speeds, tapping mode AFM can suffer from reduced spatial resolution and increased

risk of damage to either the AFM probe or the sample. Typical values for rastering size and frequency are 25 μm × 25 μm and 0.5 Hz per line. Larger rastering sizes will benefit from slower rastering frequencies whereas smaller sizes can be measured at faster frequencies. The dimensions of high-quality output files are typically 512 lines and 512 points per line. Smaller values can be chosen for quicker measurements with coarser image quality while higher values can be chosen if higher resolution is desired and the spatial resolution limit of the AFM probe has not yet been reached.

The AFM results presented throughout this thesis were obtained using a Veeco Nanoscope V with Dimension 3100 and a Bruker Dimension Fastscan. Both resulting data sets allow for analysis within Bruker NanoScope Analysis software which has built-in features for removal of spikes and streaks, flattening, Gaussian smoothing, and low-pass filtering. Line scans of arbitrary integration width can be extracted from this data set to measure the vertical and horizontal distances of features such as the abrupt height change associated with a change in TMD layer number.

2.2.4 Scanning transmission electron microscopy

STEM is an electron beam-based technique that can enable atomic resolution characterization of thin samples in a vacuum. In this technique, a high-energy focused beam of electrons is rastered across a sample, generating a variety of signals that contain characteristic information regarding the composition, crystal structure, and electronic structure of the sample (Figure 2-19). Among these signals, the scattered transmitted electrons and the characteristic X-rays are used throughout the work presented in this thesis in the form of high-angle annular dark field (HAADF) STEM imaging and energy-dispersive X-ray spectroscopy (EDS).

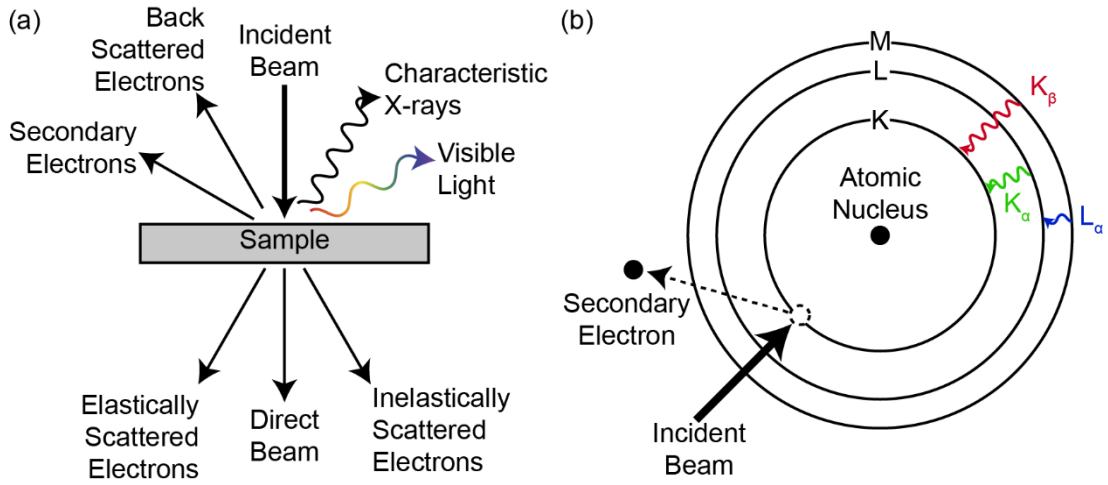

Figure 2-19. (a) Schematic representation of signals generated by electron beam irradiation. Adapted from Ref. 135. **(b)** Shell-to-shell transitions corresponding to the characteristic X-rays measured by EDS.

To perform HAADF STEM imaging, an annular detector is installed within the TEM chamber, below the sample, concentric with the direct transmitted beam. Following the interaction between the incident electron beam and the sample, some electrons will be scattered at high angles toward the detector due to Coulomb interaction with the nuclei of the atoms in the sample. The fraction of electrons scattered at high angles is strongly correlated with the atomic number of the atoms in the sample with heavier elements resulting in more scattering than lighter elements. By correlating the annular detector signal intensity with the position of the rastering electron beam, an image is generated in which high intensity regions indicate the presence of heavier elements, low intensity regions indicate the presence of lighter elements, and zero intensity regions indicate empty space. When properly correcting for electron beam aberrations, HAADF STEM imaging can routinely achieve sub-Å resolution.[136]

Similar to PL, EDS operates on the principle of electron excitation and relaxation at specific energy levels determined by characteristic properties of the material. Whereas the relevant emission energy of PL denotes the band-to-band transition across the band gap of a material, the EDS emission energies correlate to the shell-to-shell transitions within an individual atom. The

exact energies of these shell-to-shell transitions are element-specific, thereby providing a spectrum that can serve as a fingerprint to enable elemental mapping.

As a highly versatile tool, electron microscopy comes with a wide variety of tunable parameters including electron beam current density, probe size, aperture sizes, convergence angles, pixel dimensions, dwell times, and many more. Among these parameters, the most critical to the imaging of 2D TMDs is the beam voltage. Higher beam voltage results in a smaller electron wavelength and better diffraction-limited resolution. However, this resolution comes at a consequence. When the incident electron beam interacts with the sample, inelastic scattering events can happen, resulting in the transfer of energy from the electron beam to the sample. This energy transfer can result in atomic displacement within the sample or, in the case of atoms near the surface of a material, atomic ejection from the sample (Figure 2-20). In the case of monolayer TMDs, every atom of the material is a surface atom and is therefore at risk of atomic ejection by inelastic scattering events. Lighter elements are known to require lower voltages to avoid atomic displacement[137] and the general consensus in the field of 2D TMD microscopy is that beam-induced damage can be adequately minimized without severely affecting resolution when the beam voltage is set at or just below 80 keV.[64,138,139] The majority of the STEM imaging results presented throughout this thesis were obtained using an 80 keV electron beam voltage.

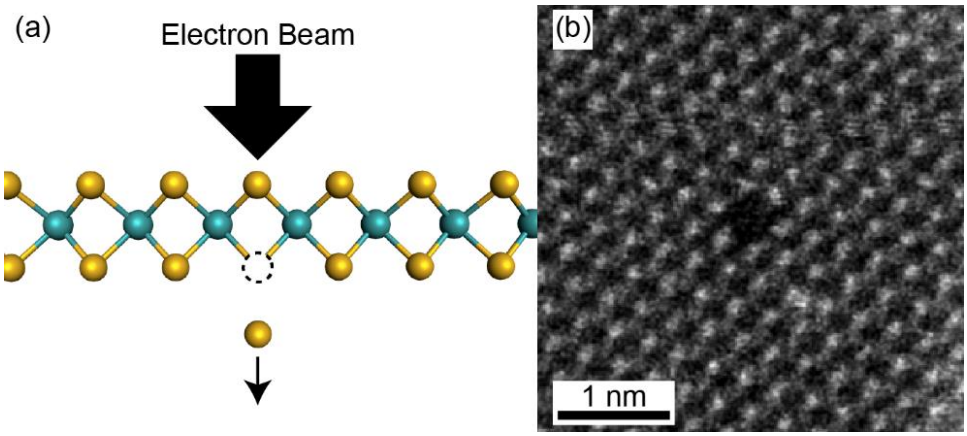

Figure 2-20. (a) Schematic of S ejection from electron beam energy transfer. **(b)** STEM image of defective TMD lattice following electron beam-induced atomic ejection.

2.3 **Conclusions**

TMD semiconductors are an exciting material system due to the novel properties enabled by their 2D structure. However, the sub-nm thickness introduces several challenges to the synthesis and characterization of these materials. In this chapter, we have demonstrated two methods of producing these monolayer materials – mechanical exfoliation and chemical vapor deposition – and one method of carefully handling these materials for arbitrary substrate transfer processes. Additionally, a variety of characterization techniques are described that focus on the localized analysis of the chemical, structural, and optoelectronic properties of these materials. Throughout the next four chapters, these synthesis and characterization techniques will be applied to investigate of the nature of 2D TMDs and address various challenges in the field of 2D TMD processing.

Chapter 3: Diffusion-Mediated Synthesis of MoS_2/WS_2 Heterostructures

This chapter is adapted with permission from Ref. 140:

Bogaert, K., Liu, S., Chesin, J. Titow, D., Gradecak, S., Garaj, S. Diffusion-Mediated Synthesis of MoS_2/WS_2 Lateral Heterostructures. *Nano Lett.* **16**, 5129-5134 (2016).

Controlled growth of 2D TMD lateral heterostructures would enable on-demand tuning of electronic and optoelectronic properties. Prior to the work presented in this chapter, compositional modulations in lateral TMD heterostructures have been considered to depend solely on the growth chronology. In this chapter, we show that in-plane diffusion can play a significant role in the chemical vapor deposition of MoS_2/WS_2 lateral heterostructures leading to a variety of nontrivial structures whose composition does not necessarily follow the growth order. Optical, structural, and compositional studies of TMD crystals captured at different growth temperatures and in different diffusion stages suggest that compositional mixing versus segregation are favored at high and low growth temperatures, respectively. The observed diffusion mechanism will expand the realm of possible lateral heterostructures, particularly ones that cannot be synthesized using traditional methods.

3.1 **Introduction**

As mentioned in the introduction to this thesis, 2D TMDs are a relatively new class of semiconducting materials that have garnered significant interest due to their high carrier mobilities, visible light direct bandgaps, high on/off current ratios, and unique properties.[7,16,141,142] Because of the similarity in their crystal structure and lattice constants, alloyed TMD materials across the entire compositional range have been theoretically predicted[53,143] – and several of these have been synthesized[35,36,49,50,52,53,55,58] – allowing for continuous bandgap modulations.

In analogy to conventional semiconductors, more complex heterostructures based on 2D TMDs would expand the realm of possible device architectures, particularly because different TMD materials could have opposing levels of intrinsic doping. Understanding the mechanisms that govern the growth of pure and multi-phase TMDs will be critical for engineering more advanced heterostructures with controlled properties. In one-step growth processes, two metallic precursors are simultaneously present in the reaction chamber during the growth; after the growth the material with higher vapor pressure and nucleation rate is found in the core of the 2D crystal.[24,29,31,34–37] In two-step growths, the core domain of the first material is grown first, followed by the exchange of precursors and the growth of the ring of the second material.[27,28,30,32,39] It has been suggested that the growth chronology is the determining factor in radial domain distribution and that each subsequent growth step simply adds material onto the existing crystal edge.

The overall goal of the work presented in this chapter was to investigate the role of the various process parameters involved in CVD synthesis of TMD lateral heterostructures and push the limits of spatial and compositional control. We show that the growth chronology is not the sole – and sometimes not the governing – factor that determines the resulting structure. We report a two-step growth process in which MoS_2 is found in the core and it is surrounded by a WS_2 ring, opposite from the order in which the precursors were introduced into the CVD chamber. We propose a new thermodynamically-driven heterostructure synthesis model that utilizes in-plane diffusion to minimize crystal energy at the growth temperature. This micro-scale diffusion process is unique to the synthesis of 2D TMD materials, can enable new opportunities (*e.g.*, synthesis of new heterostructures), and should be considered in optimizing growth of 2D structures that require abrupt interfaces.

3.2 **Results**

3.2.1 Two-step growth process

Our two-step atmospheric pressure CVD heterostructure growth procedure employs a succession of the growth processes developed for the individual growth of high-quality MoS_2 and WS_2 2D crystals. In Stage I, we first synthesized monolayer and few-layer WS_2 crystals at the growth temperature $T_G^{(1)} = 1100°C$ using WO_3 and sulfur powders. The presence of WS_2 crystals and their purity were confirmed by Raman spectroscopy. Figure 3-1a shows a representative WS_2 crystal. In Figure 3-1b, Raman spectra from different crystal locations show similar features associated with WS_2 crystals, indicating that this crystal is uniform.

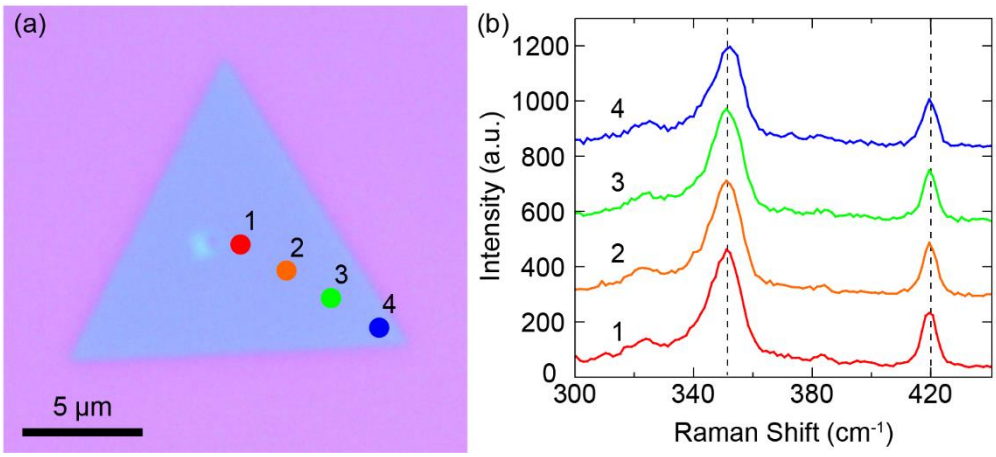

Figure 3-1. (a) Optical image of a WS_2 crystal grown at 1100°C. **(b)** Raman spectra collected in the points marked in Figure 3-1a. Dashed lines show the wavenumbers of the E_{2g}^1 (~355 cm^{-1}) and A_{1g} (~420 cm^{-1}) vibrational modes of WS_2.

The samples were then reintroduced to the CVD reactor. In Stage II, WO_3 was replaced by MoO_3 and the growth processes were performed at temperatures between $T_G^{(2)} = 650 - 710°C$, which would be optimal for single-phase MoS_2 growths. As we discuss later on, the structure of the resulting heterostructures (Figure 3-2) consistently show a strong dependence on the growth temperature: heterostructures grown at $T_G^{(2)} = 650°C$ consisted of a distinct MoS_2 core

surrounded by an $Mo_xW_{1-x}S_2$ ring (Stage III-L), whereas higher growth temperatures between $T_G^{(2)} = 680 - 710°C$ yielded a more evenly distributed $Mo_xW_{1-x}S_2$ alloy throughout the entire crystal (Stage III-H).

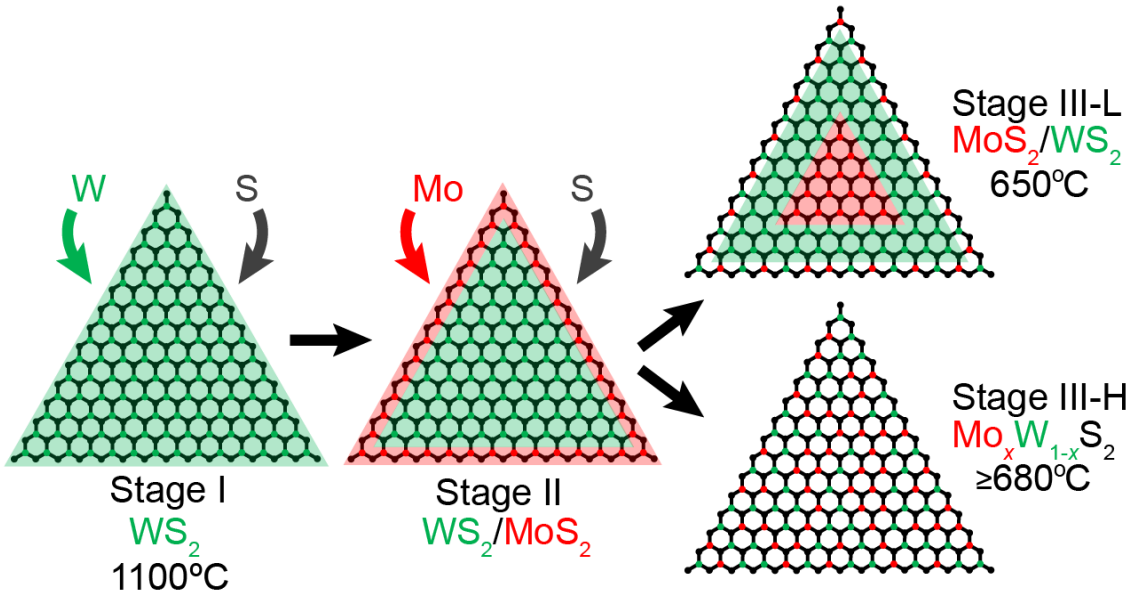

Figure 3-2. Proposed growth stages of $MoS_2/Mo_xW_{1-x}S_2$ heterostructures (W atoms are green, Mo atoms are red, S atoms are black). WS_2 crystals are first grown at 1100°C (Stage I). MoS_2 is then formed at the crystal edge after the growth temperature is reduced and MoO_3 is introduced into the growth chamber (Stage II). Depending on the substrate growth temperature during the MoS_2 growth step, the crystal forms either a phase-segregated heterostructure with a Mo-core at low temperatures (Stage III-L) or a near-uniform $Mo_xW_{1-x}S_2$ alloy at high temperatures (Stage III-H).

3.2.2 Synthesis of phase segregated crystals

An optical image (Figure 3-3a) of a representative Stage III-L heterostructure crystal grown at 650°C shows two domains forming a triangular core-ring structure. The thickness of the crystal measured by AFM (Figure 3-3b) was determined to be approximately 2.5 nm, corresponding to 3 TMD layers, with no significant topological variations between the core and the ring. A scanning electron microscope (SEM, Figure 3-3c) secondary electron image also demonstrates a clear core-shell domain structure. Contrast features by SEM secondary electron imaging indicate that a variation in the work function exists between the core and outer ring,

thereby suggesting a change in composition. This composition variation was directly measured by EDS mapping and EDS point spectra in a similar Stage III-L heterostructure crystal, demonstrated in Figure 3-3d and e. From the EDS results, we can see that the core contains strong Mo and S peaks and the ring contains strong W and S peaks. The K and Cu peaks found throughout mapping are attributable to residual KOH from the crystal transfer process and the Cu-based TEM grid, respectively.

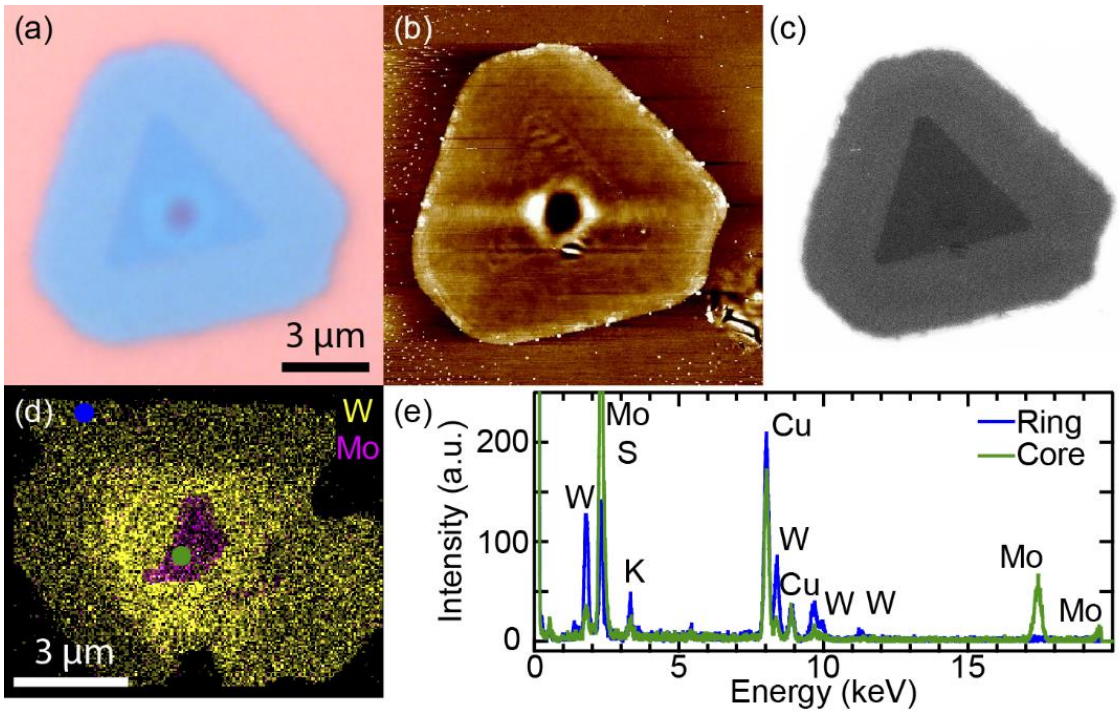

Figure 3-3. (a) Optical, **(b)** AFM, and **(c)** SEM secondary electron images of a typical heterostructure grown at $T_G^{(2)} = 650$°C (Stage III-L). Scale bar in (a) applies to (a-c). **(d)** EDS map of a Stage III-L crystal. Yellow and purple correspond to W and Mo, respectively. Colored circles correspond to the locations of EDS spectra in (e). **(e)** EDS spectra of the ring (blue) and core (green).

While EDS data is useful for elemental analysis, it does not provide direct evidence of crystal structure. To confirm the presence of MoS_2 and WS_2 and to gain addition insight into the spatial distribution of the heterostructure, we performed Raman spectroscopy mapping. Considering the E_{2g}^1 Raman peaks associated with MoS_2 (~385 cm^{-1}), WS_2 (~355 cm^{-1}), and W-rich $Mo_xW_{1-x}S_2$

alloy (~370 cm^{-1})[28,34] shown in Figure 3-4a-c, it is evident that the core domain consists of pure MoS_2, while the outer ring domain is a W-rich $Mo_xW_{1-x}S_2$ alloyed structure. A line scan demonstrating the spectral evolution across the crystal is provided in Figure 3-4d. Moving outward within the ring domain, the relative intensity of WS_2 E^1_{2g} mode (~355 cm^{-1}) decreases, whereas the WS_2 A_{1g} mode (~418 cm^{-1}) increases. Accompanied by the strengthening of the alloy-associated Raman peaks at ~370 cm^{-1} and ~390 cm^{-1}, this indicates a compositional gradient with increasing *x* (increasing Mo composition) while approaching the outer edges of the crystal. A HAADF STEM image of the domain boundary of a similarly produced crystal is provided in Figure 3-4e. The intensity contrast is correlated with the atomic mass of the elements present, indicating a nearly atomically sharp interface.

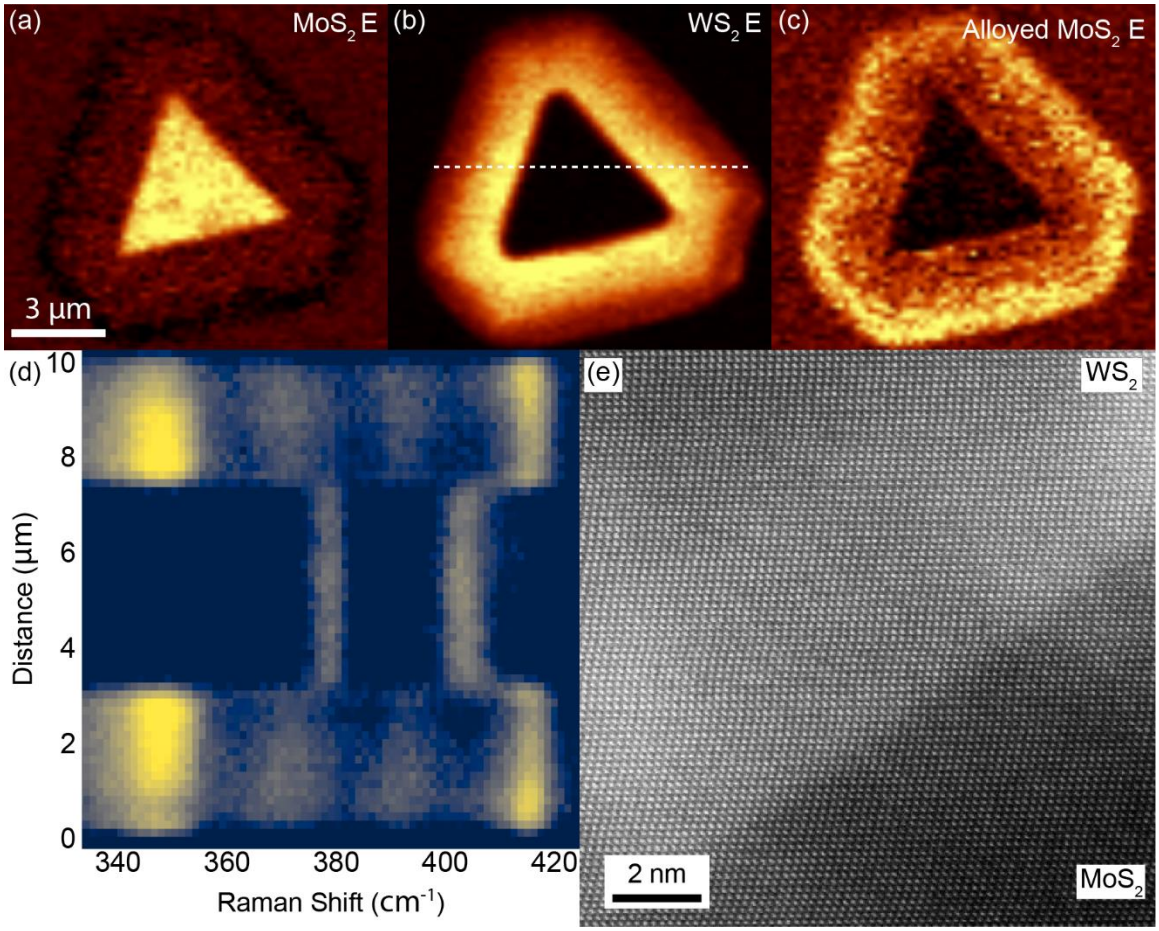

Figure 3-4. Raman intensity maps of the E^1_{2g} vibrational modes associated with **(a)** MoS_2, **(b)** WS_2, and **(c)** W-rich $Mo_xW_{1-x}S_2$ alloys. Scale bar in (a) applies to (a-c). **(d)** Raman intensity line scan corresponding to dashed line in (b). **(e)** HAADF STEM image of the domain interface.

Subsequent CVD parameter exploration has also resulted in the synthesis of phase segregated core-ring heterostructures consisting of a W-rich $Mo_xW_{1-x}S_2$ core and pure WS_2 ring, as demonstrated in the Raman map and line scan shown in Figure 3-5a and b. Measuring the contact potential difference by scanning probe microscopy, it is again evident that there exists an abrupt domain interface in which the Mo-rich TMD phase has segregated to the core, while the W-rich phase remains in the outer ring.

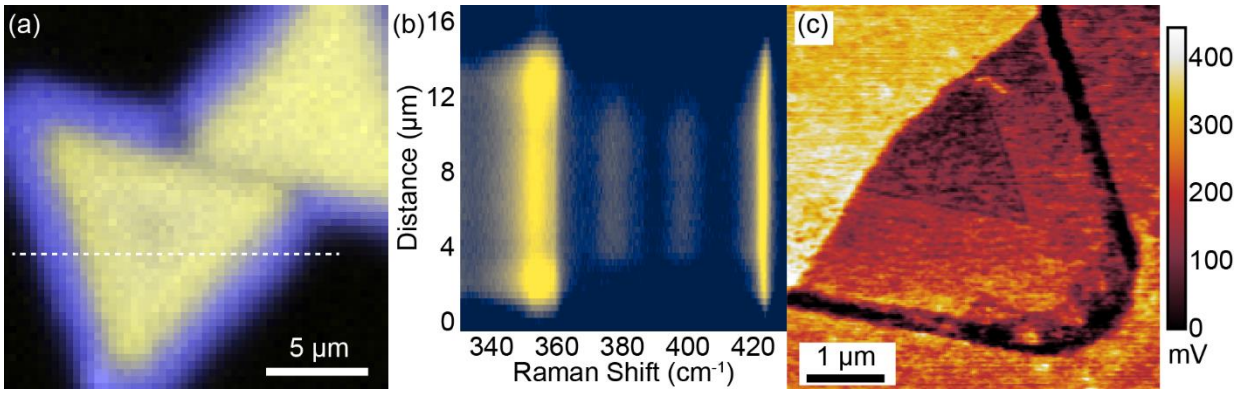

Figure 3-5. (a) Composite Raman intensity map of the W-rich $Mo_{1-x}W_xS_2$ core domain (~373 cm^{-1}, yellow) and WS_2 ring domain (~355 cm^{-1}, blue). **(b)** Raman intensity line scan corresponding to dashed line in (a). **(c)** Contact potential difference mapping of the lateral heterostructure, demonstrating an abrupt interface. The high intensity region in the upper left corner is due to residual PMMA from crystal transfer and should not be considered as a meaningful feature.

Taken together, these results show that the final composition distribution in the TMD heterostructure is independent of the growth order. Similar results were obtained on a number of crystals produced under similar growth conditions (Figure 3-6). Our results are unexpected, as they are the first observation of a micron-scale diffusion of metals in TMD crystals during heterostructure growth. In all of the previously reported two-step CVD growths, the first deposited TMD forms the core of the lateral heterostructure, and the edge atoms serve as preferential sites for epitaxial growth of the second TMD that forms the ring.[27,28,30,32,39] In our case, however, MoS_2 is deposited after WS_2 and yet, an inverted heterostructure is observed.

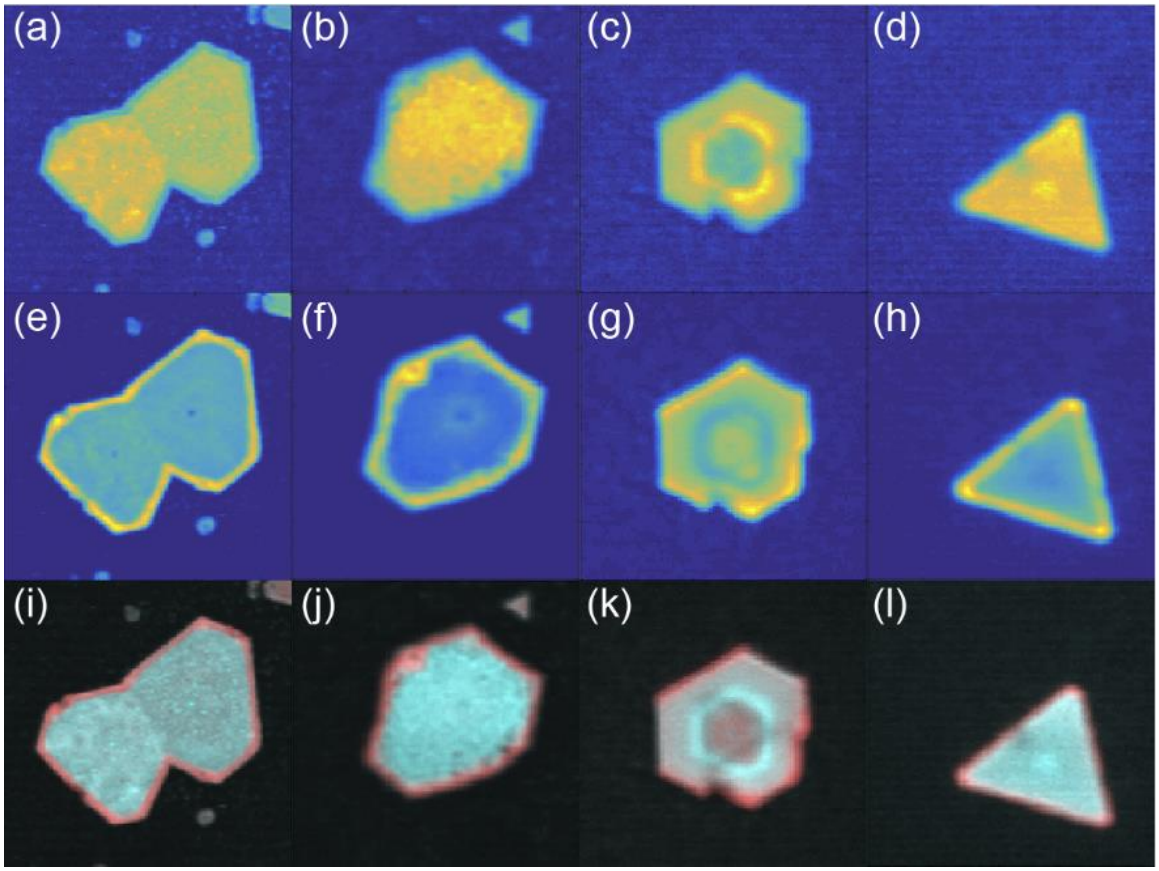

Figure 3-6. Raman intensity maps of the **(a-d)** MoS_2 and **(b-h)** WS_2 E^1_{2g} vibrational modes and **(i-l)** corresponding composite images from the Raman intensity maps indicating the relative positions of MoS_2 (cyan) core and WS_2 (red) ring domains.

3.2.3 Synthesis of alloyed crystals

To gain insights into the growth mechanism and investigate the role of the growth parameters on the apparent substitution of W atoms in the core with Mo, we performed a series of two-step growths with different MoS_2 deposition parameters. Figure 3-7 shows optical, AFM, PL, and EDS results of a sample grown using a higher growth temperature during the MoS_2 deposition ($T_G^{(2)} = 680$°C *vs.* 650°C).

Despite the differences between the fundamental principles of operation in AFM phase (Figure 3-7b) and PL imaging (Figure 3-7c and d), they reveal qualitatively similar results. These methods show a radial wavering distribution of values which likely correlate to different alloy

compositions. In the AFM phase and PL intensity images (Figure 3-7b and c), the radial wavering intensity is attributable to variations in composition-dependent energy dissipation and quantum yield properties, respectively.

PL peak position imaging (Figure 3-7d) allows for more quantitative analysis as it is correlated with the optical band gap. The PL peak positions of pure MoS_2 and WS_2 are at 680 nm and 620 nm, respectively. The deviation from these values can therefore be directly translated into the compositional information.[53] We note that this translation does not account for any additional doping, strain, or other factors that may contribute to shifts in the PL emission peak. Therefore, the computed alloy compositions should be interpreted only qualitatively. The PL data indicates that the entire crystal is a $Mo_xW_{1-x}S_2$ alloy with a MoS_2-dominant center and a slightly higher concentration of WS_2 in the outer regions. In contrast to the segregated core-ring structure of the Stage III-L crystals, these Stage III-H crystals are relatively uniform; the composition only varies over a range of approximately x = 0.44-0.57 in the $Mo_xW_{1-x}S_2$ chemical formula. This claim is further supported by EDS measurements (Figure 3-7e and f) indicating the presence of both W and Mo in the interior as well as near the crystal edge, with slightly higher W concentrations near the edge.

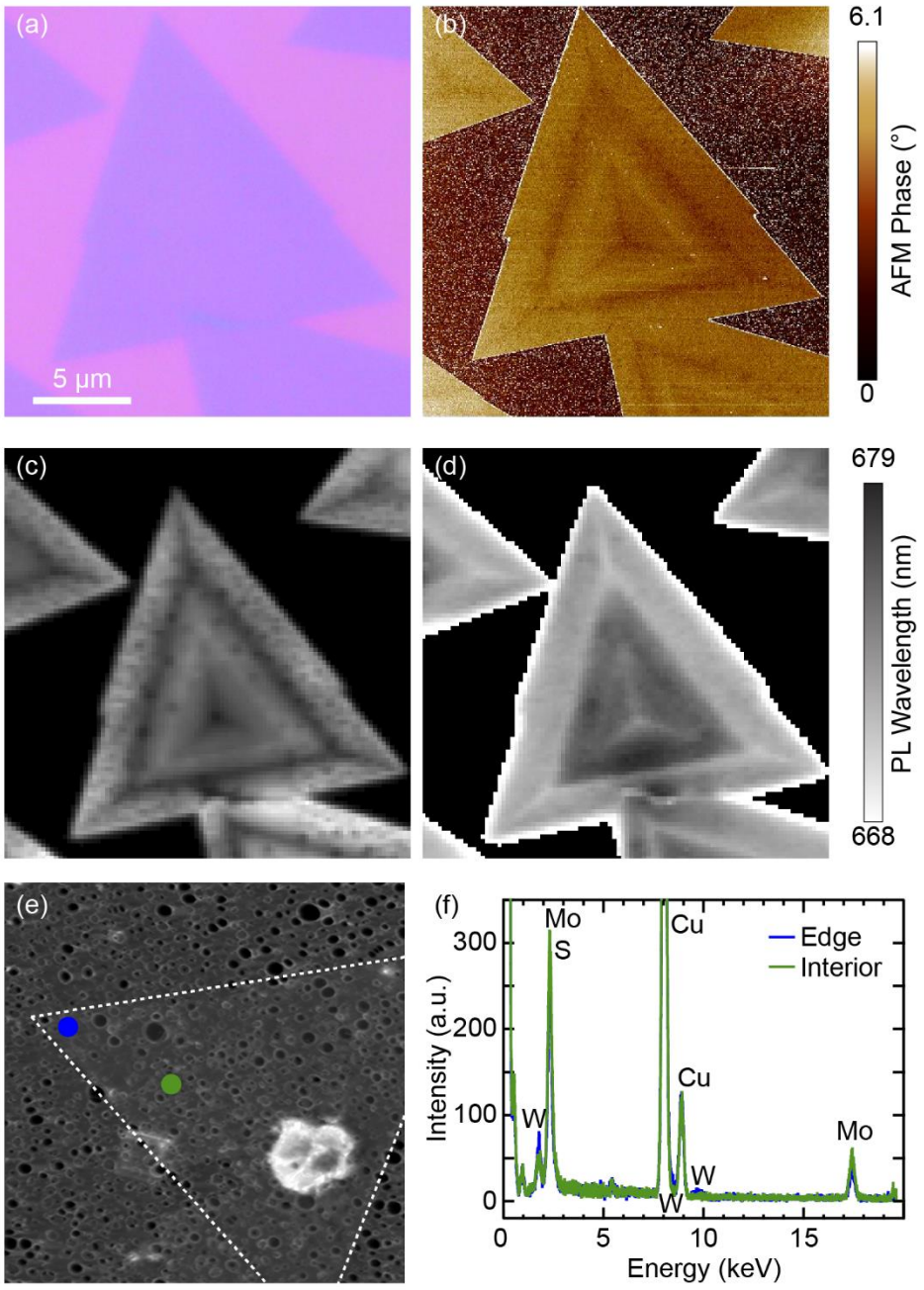

Figure 3-7. (a) Optical, **(b)** AFM phase, **(c)** PL intensity, and **(d)** PL peak wavelength imaging of a representative alloy crystal grown at $T_G^{(2)} = 680$°C (Stage III-H). **(e)** STEM image of a Stage III-H crystal. Colored circles correspond to the locations of EDS spectra in (f). Scale bar in (a) applies to (a-e). **(f)** EDS spectra of the crystal edge (blue) and interior (green).

As in the case of the phase segregated crystals, Raman spectroscopy was performed to complement the EDS results and provide additional information regarding the spatial distribution

within the crystal. Figure 3-8 demonstrates higher concentrations of WS_2 near the edges of the crystal and the presence of the MoS_2 E^1_{2g} vibrational mode throughout, corroborating the claim that this is likely a $Mo_xW_{1-x}S_2$ alloy with wavering composition.

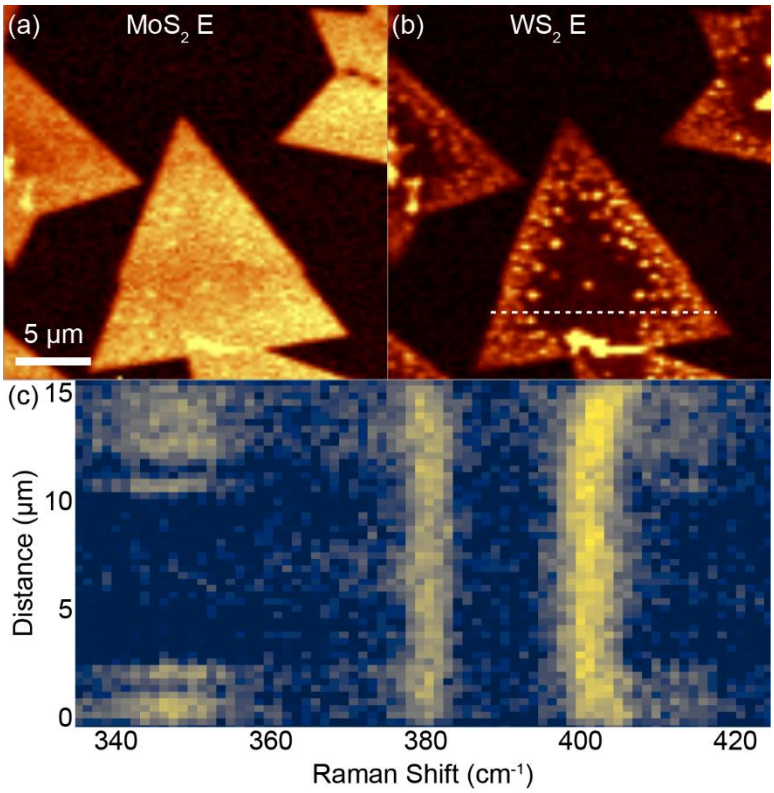

Figure 3-8. Raman intensity maps of the **(a)** MoS_2 and **(b)** WS_2 E^1_{2g} vibrational modes. **(c)** Raman intensity line scan corresponding to dashed line in (b).

Additional examples of the PL intensity and peak position fluctuations demonstrated in Figure 3-7c and d are provided in Figure 3-9. In addition to the radial changes observed in the AFM and PL images shown in Figure 3-7b-d and the PL images shown in Figure 3-9, there is often also the presence of straight lines extending from the center to the corners of the crystals (darker lines in AFM image and PL intensity, lighter in PL peak position). These lines are attributed to strain-related micro-tearing, caused by the difference in the coefficients of thermal expansion between the crystal and its substrate. Intra-grain boundaries are formed during the cooling stage, which affect optical and electronic properties of the crystal observed as a drop in

PL amplitude in pure MoS_2 and WS_2 crystals[144–146]. In the crystals shown in Figures 3-7 and 3-9, we observe not only the drop in PL intensity, but also as a noticeable shift in PL peak wavelength consistent with higher W composition. These results suggest that W preferentially diffuses to these intra-grain boundaries, further supporting our observation of the micro-scale in-plane diffusion of W toward the crystal edges (internal or external).

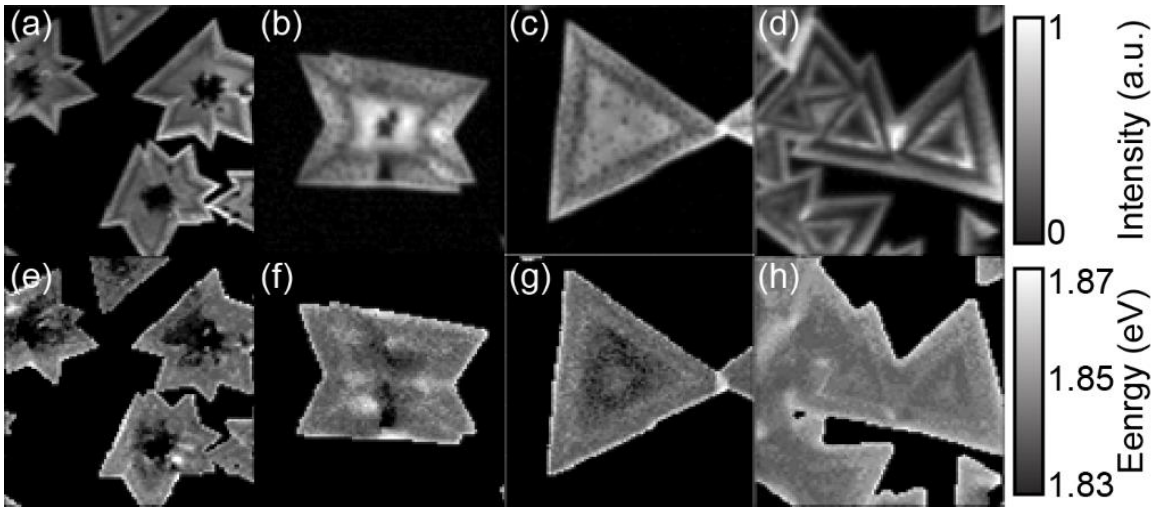

Figure 3-9. Additional examples of PL **(a-d)** intensity and **(e-h)** peak position fluctuations in nearly uniform $Mo_xW_{1-x}S_2$ alloy crystals.

To understand the interplay between the segregation and mixing observed for different MoS_2 growth temperatures, we performed a score of crystal growth experiments with varying MoS_2 growth parameters to capture different stages of the Mo atomic diffusion process. From these experiments detailed in Figures 3-10 and 3-11, we stipulate the following growth model: WS_2 crystals form on the substrate during the first growth step (Stage I in Figure 3-2). In the second growth step, MoS_2 nucleates directly at the activated WS_2 edge but the overall size and thickness of the crystal do not change (Stage II in Figure 3-2). Then, as inter-diffusion occurs, the Mo atoms substitute some or effectively all of the W atoms at the core of the crystal (Stage III-H or III-L in Figure 3-2, respectively). Because the final morphology is determined by the initial WS_2 crystal, regardless of its thickness, it can be concluded that the Mo atoms participate in intra-

layer diffusion, from the edge to the core, substituting W atoms at the M sites of the MX_2 lattice to form a tunable alloy structure.

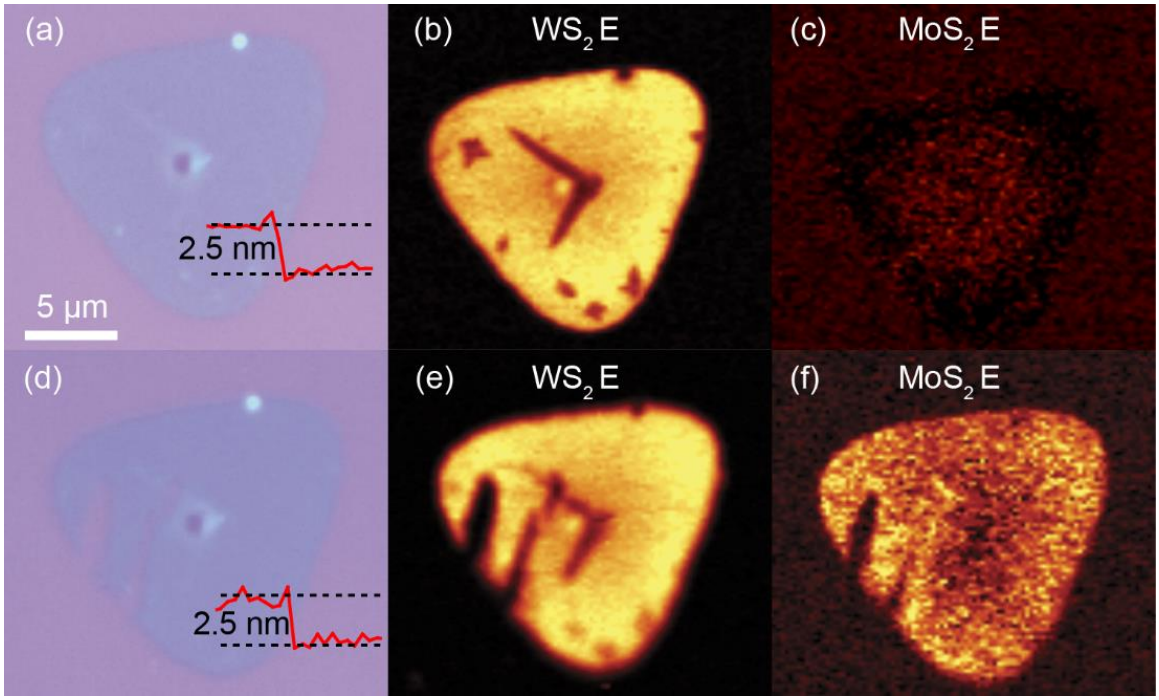

Figure 3-10. (a, d) Optical image and Raman intensity maps corresponding to the E^1_{2g} modes of **(b, e)** WS_2 and **(c, f)** MoS_2. Results are shown following (a-c) WS_2 growth and (d-f) subsequent 710°C MoS_2 growth. WS_2 remains present throughout the crystal following the MoS_2 growth step. However, the MoS_2 Raman map indicates the inter-diffusion of Mo atoms into the TMD lattice. AFM cross-sectional contour plots in (a) and (d) show the height of the crystal to be 2.5 nm after the first and second growth.

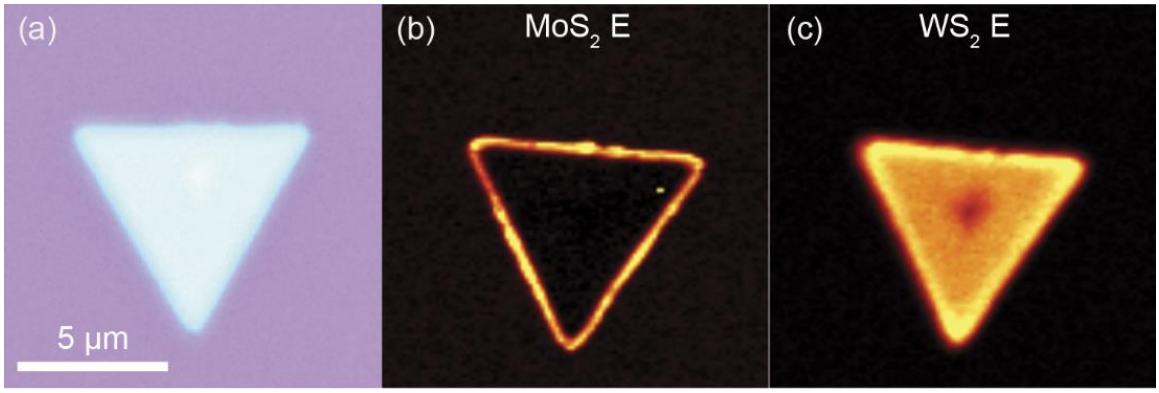

Figure 3-11. (a) Optical image of a thicker lateral heterostructure after the second MoS_2 growth at 710°C. Raman intensity maps of the E^1_{2g} mode of **(b)** MoS_2 and **(c)** WS_2. MoS_2 is initially deposited at the activated WS_2 edge area, described in Stage II in Figure 3-2. The lack of inter-diffusion could be attributable to factors such as insufficient growth time or the crystal thickness.

The substantial effect of the inter-diffusion is sensitive to the growth temperature. Two distinct heterostructures observed at different growth temperatures, as discussed above, indicate that thermodynamic and kinetic effects compete in determining the final structure and composition of the TMD lateral heterostructures. At higher temperatures (*e.g.*, $T_G^{(2)} = 680$°C or 710°C), the alloy has a more even distribution of Mo and W atoms without domain separation (Stage III-H in Figure 3-2). The entropic contribution to the Gibbs free energy becomes increasingly important with the increased temperature. As such, mixing is favored and the crystal approaches a homogeneous $Mo_{0.5}W_{0.5}S_2$ stoichiometry.[147–149] At lower temperatures (*e.g.*, $T_G^{(2)} = 650$°C), MoS_2 forms the core with a sharp interface separating it from the alloyed ring (Stage III-L in Figure 3-2). In that regime, the enthalpic contribution causes segregation into separate domains. Because MoS_2 has a lower Gibbs energy of formation than WS_2, the Mo coalesces into the core to minimize its interfacial energy.[150] We note that similar thermodynamically-driven effects leading to alloying *vs.* phase segregation may play a role in chalcogen-modified systems.[32]

Others have alluded to possible temperature-dependent domain separation in the $Mo_xW_{1-x}S_2$ heterostructure system,[34] but previous experiments involved a one-step growth, thus making it impossible to decouple the WS_2 and MoS_2 growth processes. As such, two-domain lateral heterostructures with a distinct interface were attributed to the different lifetimes of the metal precursors (MoO_3/MoO_2 *vs* WO_3) present during different stages of the sulfurization step, in agreement with the commonly accepted growth mechanism.[24,29,34] Our two-step growth reveals another important mechanism in TMD heterostructure growth in which the final structure is a thermodynamically-driven process and independent of the growth chronology. We note that a two-step WS_2/MoS_2 growth with WS_2 localized in the core was reported by Heo *et al*.[32]

However, their growth was performed at low pressure, whereas our growth was performed at atmospheric pressure, a condition that may affect the nucleation and growth kinetics of the crystal edge, as well as the relative availability of metal and sulfur precursors. For example, the growth rate observed by Heo *et al*. was approximately ten times larger than in our case, allowing the outer ring of MoS_2 to reach a critical size to stabilize before Mo atoms could diffuse inward. Since our publishing of the results described in this chapter, this discovery of thermally-induced phase segregation in 2D TMDs resulting in a Mo-rich core and W-rich outer ring has been corroborated in literature using $Mo_xW_{1-x}S_2$ ternary alloys[151] and $Mo_xW_{1-x}S_{2y}Se_{2-2y}$ quaternary alloys.[152]

3.3 **Conclusions**

In conclusion, we describe a thermodynamically-driven TMD lateral heterostructure synthesis *via* two-step CVD growth. The resulting core-ring crystal structure does not reflect the growth sequence, but is sensitive to temperature, favoring mixing at high temperatures and compositional segregation at lower temperatures. The Mo atoms are absorbed at the edge of a WS_2 crystal and diffused throughout the crystal. The resulting crystals consist of either distinctive MoS_2 core at low growth temperatures, or a rather uniform alloy at higher growth temperatures. The observed atom diffusion from the edge to the center in the structure offers an opportunity to synthesize advanced heterostructure architectures with controlled properties, as will be demonstrated in subsequent chapters. It could also provide an effective method to incorporate new transition metals into TMDs that have been theorized to exist, but impossible to synthesize using current techniques. These materials in turn can introduce unique physical properties to the field of 2D materials and open up exciting opportunities for investigating the contact interaction and carrier dynamics to create high-performance functional devices.

Chapter 4: Two-Dimensional $Mo_xW_{1-x}S_2$ Graded Alloys: Growth and Optical Properties

This chapter is adapted with permission from Ref. 153:

Bogaert, K., Liu, S., Liu, T., Guo, N. Zhang, C., Gradecak, S., Garaj, S. Two-Dimensional $Mo_xW_{1-x}S_2$ Graded Alloys: Growth and Optical Properties. *Sci. Rep.* **8**, 12889 (2018).

2D TMDs can be alloyed by substitution at the metal atom site with negligible effect on lattice strain, but with significant influence on optical and electrical properties. In the work presented in this chapter, we build upon the knowledge gained in the previous chapter and show (1) that point defects promote diffusion and alloying and (2) that these can be engineered through growth to tailor alloy properties. We develop a new defect-driven process for the growth of two-dimensional $Mo_xW_{1-x}S_2$ alloys that span nearly the full composition range within a single crystal. We observe a significant dependence of the optical quantum yield as a function of the alloy composition reaching the maximum intensity for the equicompositional $Mo_{0.5}W_{0.5}S_2$ alloy. Furthermore, we map the growth-induced strain distribution within the alloyed crystals to decouple composition and strain effects on optical properties: at the same composition, we observe significant decrease in quantum yield with induced strain. Our approach is generally applicable to other 2D materials as well as the optimization of other composition-dependent properties within a single crystal.

4.1 **Introduction**

The overall goal of the work presented in this chapter was to build on the results presented in Chapter 3 by determining the scope of the diffusion-mediated MoS_2/WS_2 heterostructure synthesis mechanism. Upon identifying the underlying factors governing this synthesis mechanism, we aimed to apply this knowledge produce 2D TMD crystals with high spatial and compositional tunability.

2D TMDs have a high degree of band structure tunability via surface doping[154–156] and alloying[34,35,55–60,140,157–159,36,48–54] which make them desirable for optical, electronic, and energy generation applications.[8,17,160–164] In analogy to conventional semiconductors, substituting various transition metal (M = Mo, W, etc.) and chalcogen (X = S, Se, Te) atoms into the TMD lattice while maintaining an MX_2 stoichiometry would enable property modulation for specific applications. Whereas spatially uniform TMD alloying offers a choice of material properties within a range given by its pure TMD components, graded TMD alloying – in which the composition gradually varies across the crystal – introduces anisotropic behavior in the bandgap, optical properties and spin-orbit coupling that could be implemented, for example, in future excitonic devices.[21]

Previous studies of alloyed TMDs have demonstrated that the PL bandgap emission energy is tunable as a function of composition, but most of these studies used discrete crystals with a specific alloy composition. This approach hinders understanding of the intrinsic relationship between PL quantum yield and composition as it does not account for non-compositional factors between different crystals (*e.g.*, substrate interactions, strain profile, defect density, etc.) that could influence the optical properties (*e.g.*, charge transfer doping, band structure modification, creation of trap states, etc.).

To circumvent this limitation, we studied the optical properties of 2D TMDs with composition variations within single crystals that were produced using the two-step CVD process based on diffusion-mediated growth described in Chapter 3. Driven by a hypothesis that the alloying is facilitated by point defects, we introduced a graded distribution of point defects into a template WS_2 crystal by mixing the metal precursor (WO_3) with NaCl admixture that is known to reduce its vaporization temperature.[96] The diffusion of Mo in the second CVD step results in a

unique graded alloy structure mirroring the starting defect distribution. By having the ability to tune composition within a single crystal, we demonstrate composition-dependent variations in PL intensity that are intrinsic to the material and not an artifact of the sample preparation. Moreover, we decouple strain- and composition-related optical properties assessing the role of substrate in future applications of 2D TMDs. In this chapter, we focus on $Mo_xW_{1-x}S_2$ alloys, but our approach is generally applicable across various TMD platforms.

4.2 **Results**

4.2.1 Heterostructure growth with mechanically exfoliated crystals

To determine the scope of the diffusion-mediated synthesis mechanism described in Chapter 3, we began by mechanically exfoliating WS_2 or MoS_2 template crystals – having a low defect density – and then employed second stage CVD growth of the complementary material (Figure 4-1) in an effort to mirror the workflow presented in Figure 3-2. Figure 4-1a shows the A_{1g} Raman vibrational mode of a mechanically exfoliated WS2 crystal following MoS2 CVD. As evidenced by the sharp interface between the WS_2 (A_{1g} position ~418 cm^{-1}) and MoS_2 (A_{1g} position ~403 cm^{-1}) regions, no alloying or diffusion has taken place. A comparable sharp interface is observed for crystals with the inverse synthesis order, consisting of a mechanically exfoliated MoS_2 core and a surrounding CVD-grown WS_2 region (Figure 4-1b). Given the inconsistent results in comparison to the results presented in Chapter 3, we can assume that the diffusion-mediated growth process is likely governed by a phenomenon that is more likely to occur in CVD-grown samples than in mechanically exfoliated samples. Given the difference in typical defect densities of these two classes of 2D TMD materials, we hypothesize that the diffusion process requires the presence of point defects.

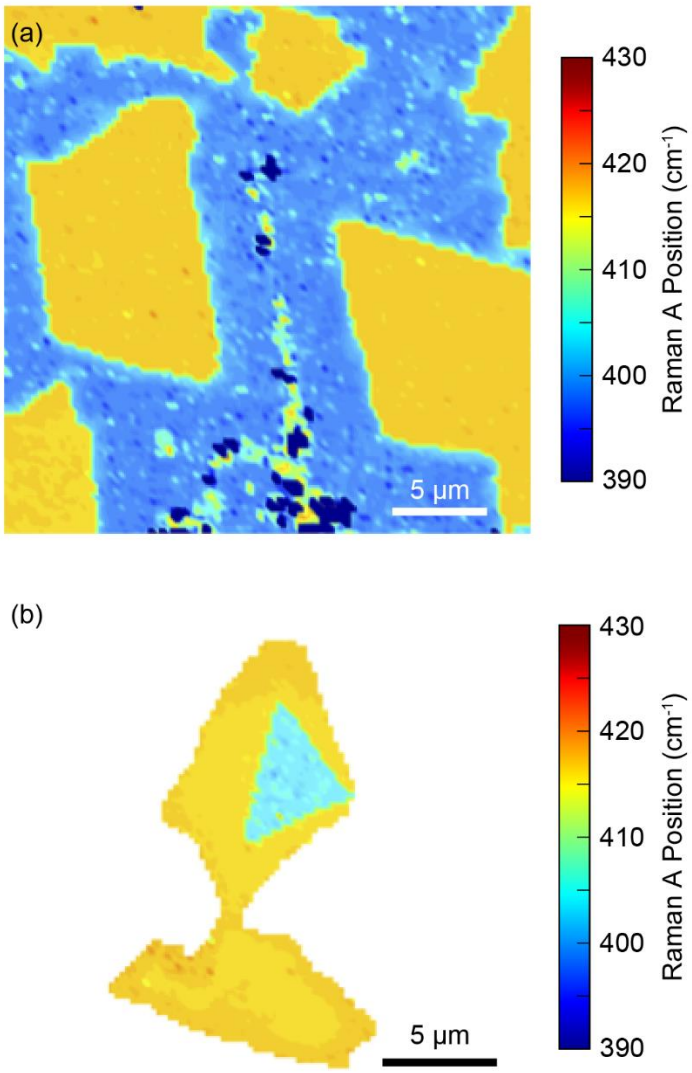

Figure 4-1. Raman position of the A_{1g} vibrational mode for **(a)** exfoliated WS_2 (yellow) followed by CVD-grown MoS_2 (cyan) and **(b)** exfoliated MoS_2 (cyan) followed by CVD-grown WS_2 (yellow). Both growths result in a lateral heterostructure with a sharp interface and chronological core-shell configuration indicating that no significant amount of diffusion occurred.

4.2.2 Correlating crystal defects with composition

To gain microscopic insight into the diffusion process, collaborators Na Guo and Prof. Chung Zhang of the National University of Singapore performed density functional theory (DFT) modeling and explored possible diffusion-exchange mechanisms and energetics of the most likely exchange path for Mo and W atoms. The DFT model consisted of a triangular single-

layer WS_2 crystal with 45 W atoms, 1 Mo adatom, 1 S vacancy, and 103 S atoms (Figure 4-2) and was implemented in Vienna ab-initio Simulation Package.[165,166] The plane-wave basis with the cut-off energy of 400 eV and the generalized gradient approximation in the Perdew-Burke-Ernzerhof format[167] with the projector-augmented wave method[168] were employed in all calculations. The structural relaxations were carried out until the Hellmann-Feynman force on each atom is less than 0.01 eV/Å, and the energy convergence criterion was set to 10^{-5} eV. Gamma-point-only *k* sampling is adopted for calculations.

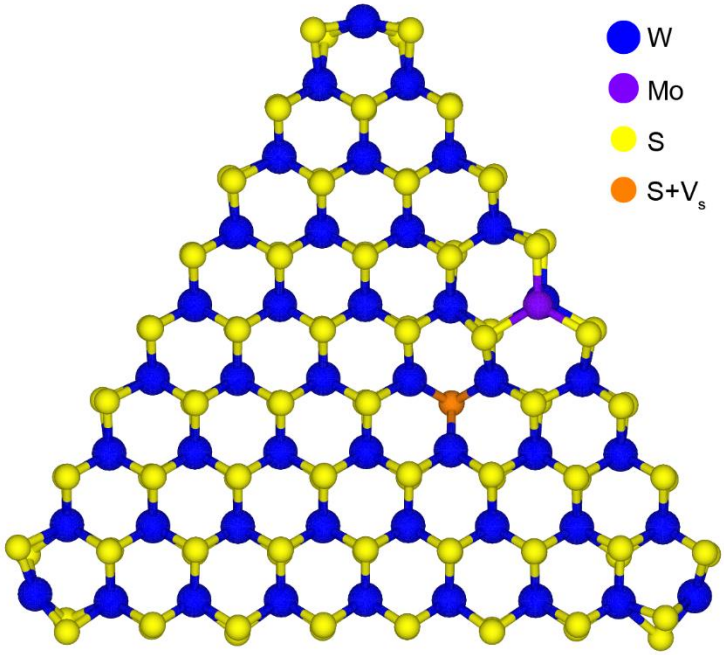

Figure 4-2. Monolayer WS_2 crystal configuration used for DFT calculations. The crystal contains one S vacancy (orange) and one Mo adatom (purple).

A S vacancy, as the most probable point defect in the crystal,[64] was placed in the interior of the WS_2 lattice in the upper plane of chalcogen atoms. The adsorption of a single Mo impurity atom was then tested on all possible sites of the crystal. The most stable adsorption configuration consists of a Mo atom adsorbed on top of an edge W atom in the vicinity of the S vacancy, which displaces the W atom downward. This configuration is depicted as the Initial Stage in Figure 4-3.

In Stage 1, the Mo atom and one neighboring S atom diffuse toward the S vacancy to temporarily form antisite defects until they eventually reach the vacancy in Stage 2. At this point, the S atom fills in the original S vacancy – thereby creating a new vacancy site in the upper plane of chalcogen atoms – and the Mo atom is positioned on top of a different W atom within the crystal. In Stage 3, the S atom moves from the lower plane of chalcogen atoms to the upper plane of chalcogen atoms and the Mo atom moves downward into the plane of metal atoms, forcing the W atom to occupy the S vacancy site in the lower plane of chalcogen atoms. In the Final Stage, the W atom is expelled further toward the crystal edge to the metal site. It is important to note that the system is capable of overcoming the Stage 2 energy barrier at the experimentally tested growth temperatures. Altogether, this process demonstrates a thermodynamically viable mechanism for the inward diffusion of Mo atoms accompanied by an outward diffusion of W atoms and S vacancies, turning a relatively defective WS_2 crystal into a higher quality crystal with a Mo-rich core. This mechanism corroborates and helps to explain the S vacancy-Mo coupling in W-rich $Mo_xW_{1-x}S_2$ reported by Azizi *et al*.[169]

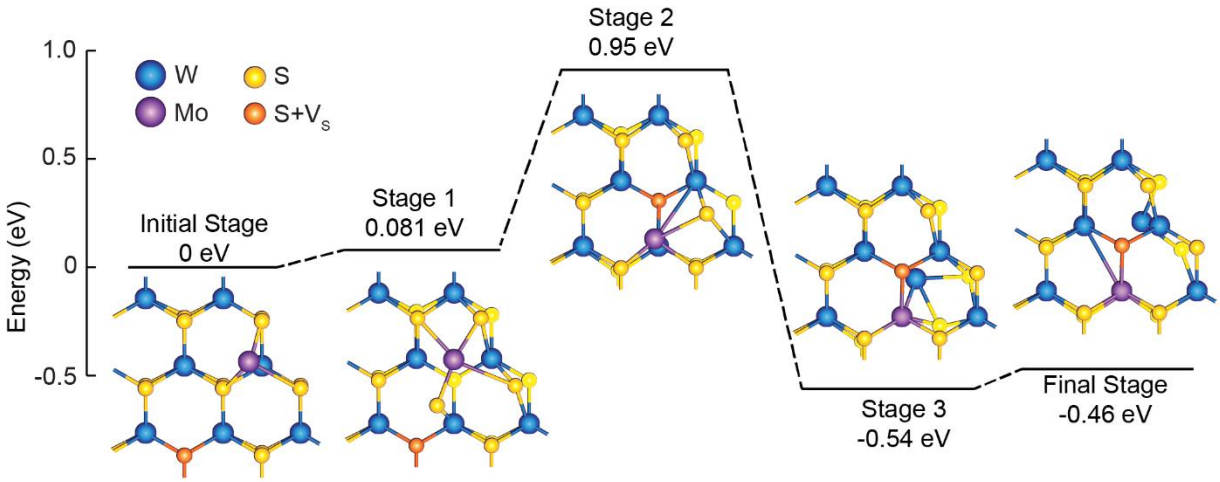

Figure 4-3. DFT-calculated proposed reaction path and schematics of atomic configurations for inward diffusion of a Mo atom and outward diffusion of a W atom and S vacancy. From the Initial Stage to Stage 2, a Mo adatom and S atom diffuse inward together, resulting in the outward diffusion of a S vacancy. From Stage 2 to the Final Stage, the Mo adatom incorporates into the metal plane of atoms, displacing a W atom, which then diffuses outward through the S vacancy site to the crystal edge. This reaction is exothermic.

4.2.3 Defect-driven synthesis of graded alloys

To experimentally test this defect-driven nature of the diffusion process, we engineered a spatially heterogeneous concentration of point defects in CVD-grown WS_2 crystals that were then re-introduced to the CVD furnace for growth of a Stage III-H $Mo_xW_{1-x}S_2$ alloy crystal. The WS_2 crystals were first grown at 825 ºC using WO_3/NaCl precursor. Figure 4-4 shows a representative Raman spectrum and intensity ratio map that compares $LA(M)$ and A_{1g} vibrational modes of a template WS_2 crystal grown using the NaCl-based CVD method. It has been previously shown that the $LA(M)/A_{1g}$ Raman intensity ratio is proportional to the inverse square of the distance between point defects with low-defect crystals having a ratio of 0.10-0.15.[93] WS_2 crystals grown without NaCl show a uniform ratio ≤0.15;[140] in contrast, these WS_2 crystals grown using NaCl are more defective with the ratio ranging from 1.4 at the crystal core

to 0.8 at the edges. The graded $LA(M)/A_{1g}$ intensity ratio present in NaCl-assisted WS_2 crystals is indicative of a graded point defect distribution, with a greater density of defects near the crystal core compared to the exterior. This is likely due to a W-rich atmosphere during early stages of the crystal growth leading to non-stoichiometric crystal growth and formation of sulfur vacancies. This result indicates that the higher density of point defects in the core of the starting WS_2 crystal enhances Mo diffusion and results in the graded Mo concentration in the resulting alloyed structure. Since our publishing of the results described in this chapter, this discovery of S vacancy-assisted cation exchange in 2D TMDs has been corroborated in literature using in Re-doped MoS_2.[170]

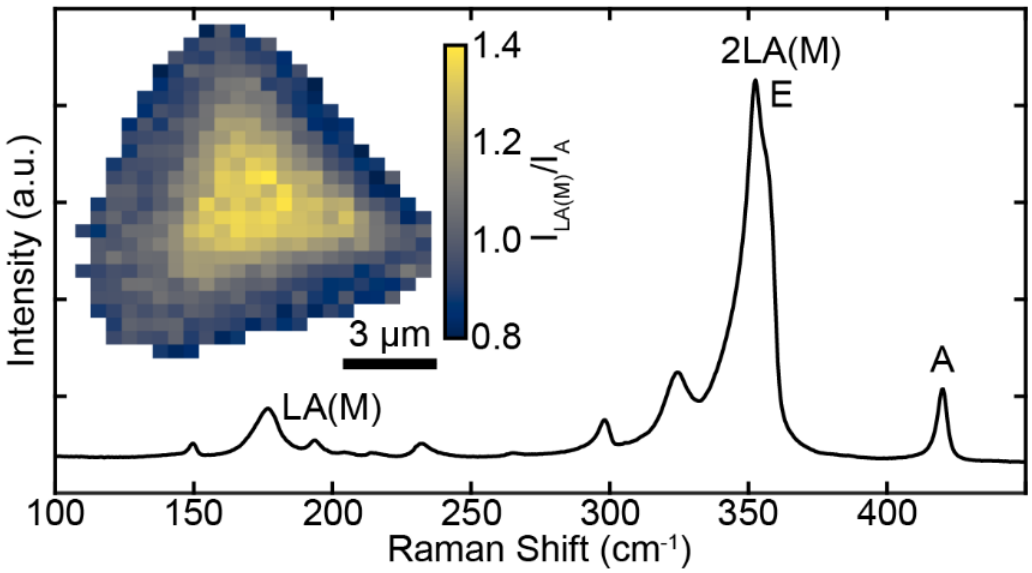

Figure 4-4. Averaged Raman spectrum of a WS_2 crystal grown using NaCl. Inset maps the ratio between intensities of $LA(M)$ (174 cm^{-1}) and A_{1g} (418 cm^{-1}) vibrational modes showing a graded distribution of defects within the crystal with the highest concentration in the center.

Figure 4-5a shows the Raman A_{1g} vibrational mode of a representative single crystal following NaCl-assisted WS_2 growth and subsequent MoS_2 CVD growth at 680 ºC. It has been demonstrated that the position of the A_{1g} vibrational mode shifts linearly over the composition range from ~403 cm^{-1} for pure MoS_2 (x = 1) to ~418 cm^{-1} for pure WS_2 (x = 0).[52] As it can be

seen in Figure 4-5a, the A_{1g} mode in our crystals changes gradually from 400 cm^{-1} in the center of the crystal to 415 cm^{-1} toward the crystal edges, thus demonstrating continuously changing $Mo_xW_{1-x}S_2$ composition. The PL peak energy map of the same crystal (Figure 4-4b) corroborates the Raman results shown in Figure 4-5a. The exciton emission energies of pure MoS_2 and WS_2 are 1.82 eV and 1.97 eV, respectively,[24] whereas the measured PL energy range spans from 1.82 eV to 1.95 eV starting from the crystal core toward edges, respectively. Taken together, these results indicate that the crystal has a three-fold symmetry with pure MoS_2 in the core and gradually-shifted composition toward the crystal edges that are composed of almost pure WS_2. This gradient in composition is quantified in Figure 4-5c, calculated from the Raman data presented in Figure 4-5a.

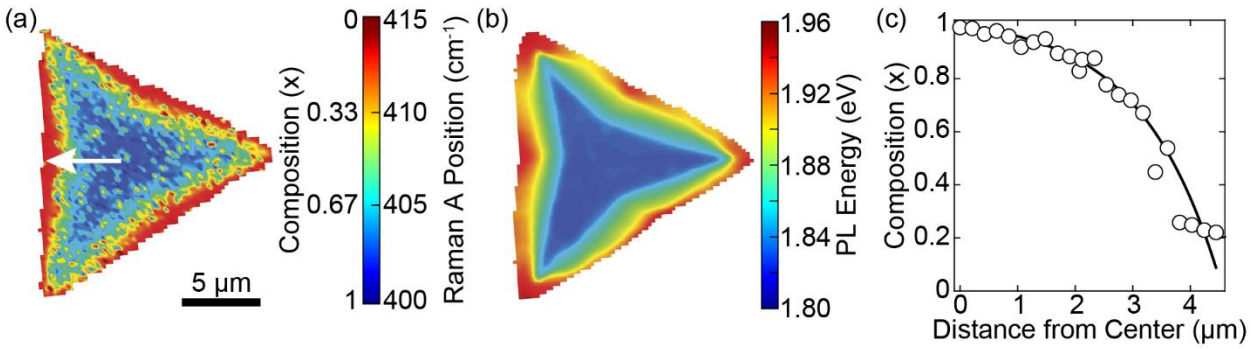

Figure 4-5. (a) Raman position of the A_{1g} vibrational mode (and thus the composition *x*) of a $Mo_xW_{1-x}S_2$ graded alloy crystal. **(b)** Corresponding PL peak energy map. **(c)** Crystal composition as a function of the position along the arrow shown in (a) determined using the Raman A_{1g} vibrational mode. The line is a guide for eye.

Figure 4-6 provides Raman and PL data corresponding to additional crystals with graded alloying produced by the same method described above. All measurements yield similar results, demonstrating the reproducibility of our technique.

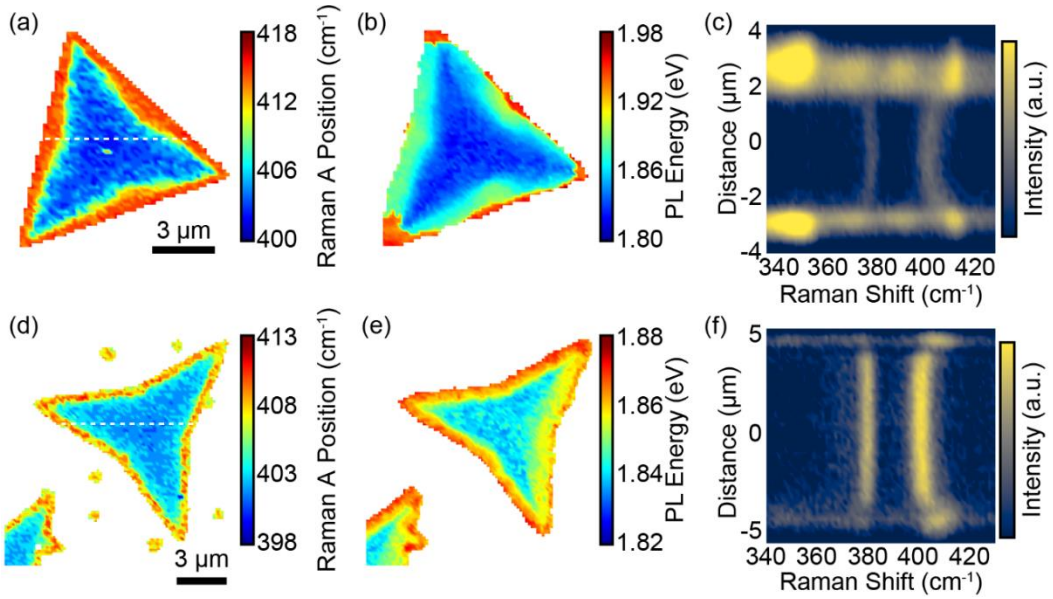

Figure 4-6. (a, d) Raman position maps of the A_{1g} vibrational mode, **(b, e)** PL peak energy maps, and **(c, f)** Raman line scans corresponding to the dashed lines in (a) and (d), respectively, of additional $Mo_xW_{1-x}S_2$ graded alloy crystals.

4.2.4 Correlating optical properties with composition

This unique graded structure now allows us to investigate the material properties as a function of the composition within a single crystal, thus obtained under identical synthesis conditions. Here we focus on developing an understanding of the PL quantum yield as a function of the $Mo_xW_{1-x}X_2$ alloy composition. To do so, we must have a method of correlating the optical properties at a given location with the local composition. Figure 4-7 compares the Raman and PL peak energy maps shown in Figure 4-5a and b, respectively. The results indicate a strong correlation between these two measurements, suggesting that the established relationship[52] between alloy composition and the Raman A_{1g} position can be extended to PL peak energy.

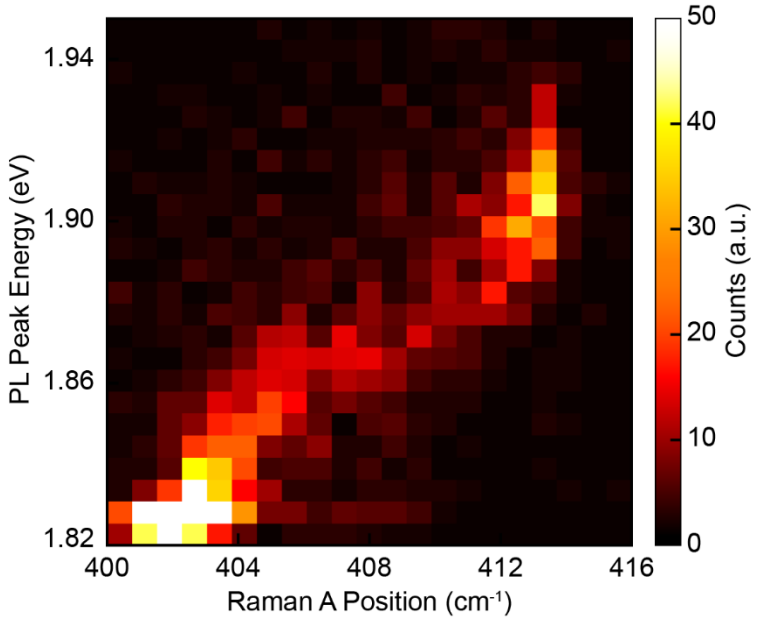

Figure 4-7. Heat map correlating the Raman position of the A_{1g} vibrational mode and the PL peak energy from a single $Mo_xW_{1-x}S_2$ graded alloy crystal, using the data represented in Figure 4-5a and b, respectively.

Figure 4-8a shows an assortment of normalized position-dependent PL spectra of the crystal from Figure 4-5 that demonstrate a continuous transition from MoS_2-like emission near the crystal core to WS_2-like emission near the crystal edges. This composition-dependent PL intensity data gives us an important insight into the relationship between PL quantum yield and the alloy composition. Although PL quantum yield specifically refers to the ratio between electron-hole pairs generated and photons radiated, we can make reasonably accurate relative comparisons from PL intensity fluctuations within a single measurement because the laser power density and acquisition time are constant, the absorbance for monolayer MoS_2 and WS_2 at 532 nm are approximately equal,[171] and the effects of exciton funneling are assumed to be negligible. Figure 4-8b maps the intensity of the PL intensity as a function of the position. By plotting the PL intensity along the lines that connect the crystal core to the triangle sides (sketched blue in Figure 4-8c), it can be observed that PL intensity increases and decreases exponentially as a function of the PL energy, with the maximum PL intensity centered at ~1.87 eV (Figure 4-8d).

This result suggests that the maximum PL quantum yield in $Mo_xW_{1-x}X_2$ system occurs for an alloy (in our case, for $x \approx 0.5$) rather than for either of the pure extrema (MoS_2 or WS_2). In contrast to previous reports that have focused on either pure WS_2 and MoS_2[172] or limited-range, Mo-rich $Mo_xW_{1-x}Se_2$,[57] our results probe the PL quantum yield for nearly the entire $Mo_xW_{1-x}S_2$ alloy spectrum.

Similar PL enhancement has been reported in ternary alloys of III-V semiconductors.[173,174] In those material systems, the enhanced radiative recombination has been attributed to reduced carrier mobility resulting in enhanced carrier localization. However, due to the large exciton binding energy of 2D TMDs,[175] the analogy between the two systems is not straight-forward. Instead, the PL enhancement could be the result of a decrease in concentration of non-radiative point-defect related deep levels in the alloy, as theoretically predicted.[176]

In addition, our results indicate that the PL quantum yield of $Mo_xW_{1-x}X_2$ materials is also sensitive to strain. Figure 4-8d shows that the PL intensity is reduced by more than an order of magnitude for the same PL energy/crystal composition when measured from the crystal core toward the corners (sketched red in Figure 4-8c). Generally, the strain accumulates at the corners due to the significant difference in temperature between growth conditions (825 °C for WS_2 and 680 °C for MoS_2) and room temperature as well as the difference in the coefficient of thermal expansion between TMDs and the substrate, SiO_2.[34,59,92,140,177,178] Given the low PL intensity in the strained regions at all compositions, we can conclude that the strain-dependent effects on PL quantum yield supersede the composition-dependent effects. Therefore, it is evident that strain must be well-controlled, whether through crystal transfer,[179] substrate choice,[180] or other means, to control the luminescence yield regardless of crystal composition.

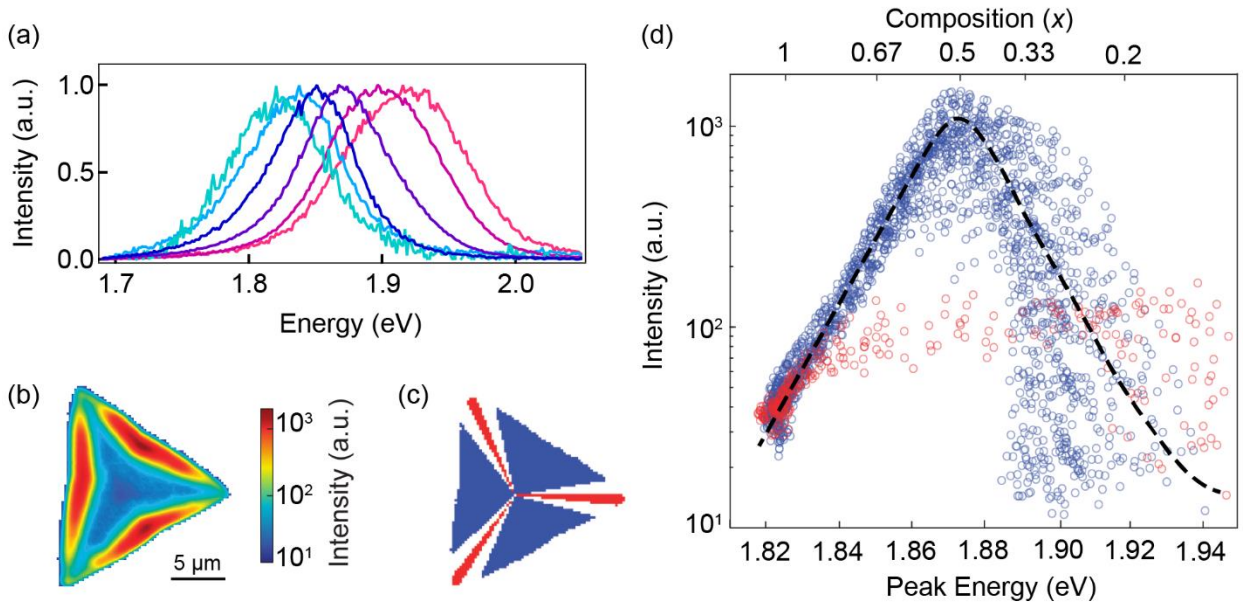

Figure 4-8. (a) Normalized PL spectral evolution from the crystal core (cyan, left-most spectrum) toward the edge (red, right-most spectrum). **(b)** Spatial map of the PL intensity within the crystal shown in Figure 4-5, plotted on a log scale. **(c)** Color-coded map of the crystal indicates PL data points extracted for the unstrained (blue) and strained (red) regions, as shown in (d). From the crystal center, all pixels of the crystal within 1.5 degrees of the symmetry lines connecting the center to the corner are colored red, indicating regions of greatest strain. All pixels greater than 6 degrees away from the symmetry lines are colored blue, indicating regions of least strain. **(d)** PL peak energy *vs.* intensity of the graded alloy crystal. Top scale shows the corresponding composition *x* determined from Raman measurements (we note that the scale is not linear due to non-linear relation between the PL peak energy and the composition). The blue(red) data points in the graph were taken from the blue(red) (*i.e.*, unstrained(strained)) regions of (c). Dashed line is a guide for eye for the unstrained data, which mostly follows the average value of the blue data points.

4.3 **Conclusions**

In conclusion, we have established the relationship between PL intensity and alloy composition (*x*) within single crystals of $Mo_xW_{1-x}S_2$ graded alloys that span nearly the entire composition range. Our results show an exponential increase of the quantum yield with increased alloying, reaching the maximum value for equicompositional alloy $Mo_{0.5}W_{0.5}S_2$ (x=0.5), which is two orders of magnitude enhanced compared to the values for pure MoS_2 (x=1) and pure WS_2 (x=0). Such observation is consistent with theoretical prediction that alloying could suppress the deep in-gap level responsible for non-radiative recombination, and offers the

venue for improving optical performance of TMD materials. Additionally, we demonstrated that the introduction of the strain leads to suppression of PL intensity for all the compositions of the alloys. The synthesis of graded alloys was achieved by diffusion-driven metal exchange in the pure TMD template crystals. DFT calculations reveal a thermodynamically favorable diffusion-exchange reaction path for controlled alloying, controlled by the sulfur vacancies. Our approach can be extended to other TMDs and future experiments to engineer the defect distribution by other means (*e.g.*, laser, O_2 plasma, annealing in air etc.) that would enable a higher degree of control over compositional tuning and patterning in a crystal, as will be demonstrated in Chapter 5. On-demand alloys such as these could be useful in several applications that require controlled, directional anisotropy of optical and/or electrical properties.

Chapter 5: Direct-Write Patterning of Two-Dimensional Heterostructures by Laser-Induced Defect-Engineering

In this chapter we present a direct-write patterning method for 2D TMD heterostructures grown by CVD using laser-induced defect formation as a reliable method for controlling the location of nucleation. We investigate WS_2 defect formation as a function of laser power and wavelength and determine the efficacy of identifying these defects by various characterization techniques. We demonstrate the site selectivity of subsequent MoS_2 growth. This direct-write technique will simplify the process of heterostructure patterning and enable the routine fabrication of complex device architectures necessary for various advanced applications.

5.1 **Introduction**

Chapters 3 and 4 demonstrate the role of point defects in the synthesis of spatially and configurationally tunable 2D TMD crystals. However, those demonstrations involved *in situ* defect formation during CVD growth, which offers limited ability to achieve targeted resolution or more complex, deterministic interfaces. Therefore, in the work presented in this chapter, we demonstrate a laser-based tunable method to directly pattern point defects into TMD crystals with the eventual result of enabling defect-driven synthesis of TMD heterostructures and alloys.

Patterning is often a necessary step to form the desirable junctions and interfaces within a heterostructure. Top-down methods of patterning often involve placement of initial material, creation of a mask, etched removal to form the pattern, and then growth of a second material into the newly created void.[40,41] While this technique is powerful, it does not provide a high degree of control over the growth of the second material. That is, the second material will grow on all exposed substrate, thus potentially necessitating additional patterning steps. By a similar method, the etch and growth steps can be combined into a single replacement step, as demonstrated by

the selective sulfurization of $MoSe_2$ into $MoS_2/MoSe_2$ heterostructures.[42] Although this technique enables greater spatial control of the second material (in this case, MoS_2), it is limited in scope to the sulfurization of transition metal diselenides. In the patterning of non-heterostructure 2D TMDs, etching by laser-irradiation has previously been demonstrated[181,182] as a method for selective thinning of multi-layer crystals and similar methods such as oxidation scanning probe lithography has been reported to create nano-channels, dots, wires, and ribbons in 2D semiconductors.[183]

Heterostructure patterning can also be achieved by bottom-up methods. For example, patterned device fabrication has been demonstrated using surface functionalization by substrate plasma treatment to define regions of TMD nucleation.[43–45] Additionally, 2D crystals can be patterned using lithographically patterned seed holes or materials such as MoO_3 or ammonium heptamolybdate.[46,47] These can be useful steps for patterning a single 2D material, but have not yet been applied to heterostructures.

In this chapter, we report a direct-write patterning method for 2D TMD heterostructures grown by CVD using laser-induced defect formation as a reliable method for controlling the location of nucleation. Figure 5-1 provides a schematic and proof-of-concept example of this three-step process. In the first step (Figure 5-1a and b), an initial crystal is produced. In the second step (Figure 5-1c and d), a diffraction-limited laser with mW-range power is rastered across the crystal, dwelling at each pixel for a few seconds. This locally heats the initial crystal, inducing localized defect formation by thermally-assisted oxidation. Defect sites are preferentially favored for chemical transformation to form heterostructures or alloys (see Chapter 4).[153,184,185] In the third step (Figure 5-1e and f), the sample is placed into a CVD furnace for TMD growth. Through careful control of the nucleation and growth kinetics,[24,32] heterostructure

formation primarily occurs along the laser annealed pattern. For heterostructures discussed throughout this chapter, the initial crystals are always mechanically exfoliated WS_2 and the second TMD material is always MoS_2. However, this technique should be applicable to other methods of producing the initial crystal as well as other TMD chemistries.

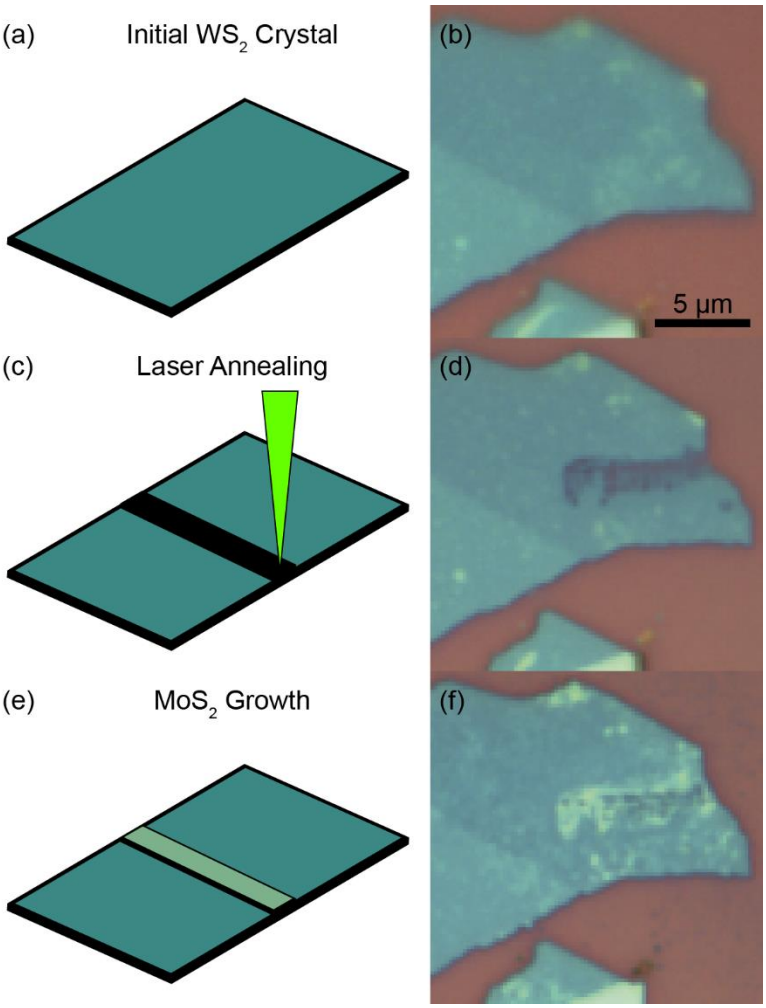

Figure 5-1. (a, c, e) Schematic and **(b, d, e)** proof-of-concept example of three-step heterostructure formation process. (a, b) An initial TMD crystal is identified on a flat substrate. (c, d) Laser exposure results in thermally induced defect formation. (e, f) TMD growth preferentially occurs at the previously exposed location.

5.2 **Results**

5.2.1 Laser-induced local annealing

In an effort to directly pattern point defects into TMD crystals, a variety of chemical and physical defect formation methods (see Section 4.3) coupled with lithographic patterning were considered. Of these, laser-induced annealing appeared to offer a good compromise of feasibility, high throughput, rapid characterization, process parameter tunability, and resolution.

To confirm the feasibility of laser annealing, a CVD-grown MoS_2 sample (Figure 5-2a) was exposed to a 532 nm, 9.29 mW laser with a 1 μm diameter to cause laser-induced damage. A 2 μm × 3 μm area was exposed to a 15 × 15 pixel array of exposures with a dwell time of 1 s/pixel. Raman mapping (Figure 5-2b) was conducted with 25% of that laser power and 0.1 s dwell time to avoid further damage, revealing distinct laser-induced patterning. SEM (Figure 5-2c and d) provides greater detail of the laser-induced damage: arrays of nanopores appear within the region of high-power laser exposure, indicating that the laser can induce significant and permanent damage to the crystal structure.

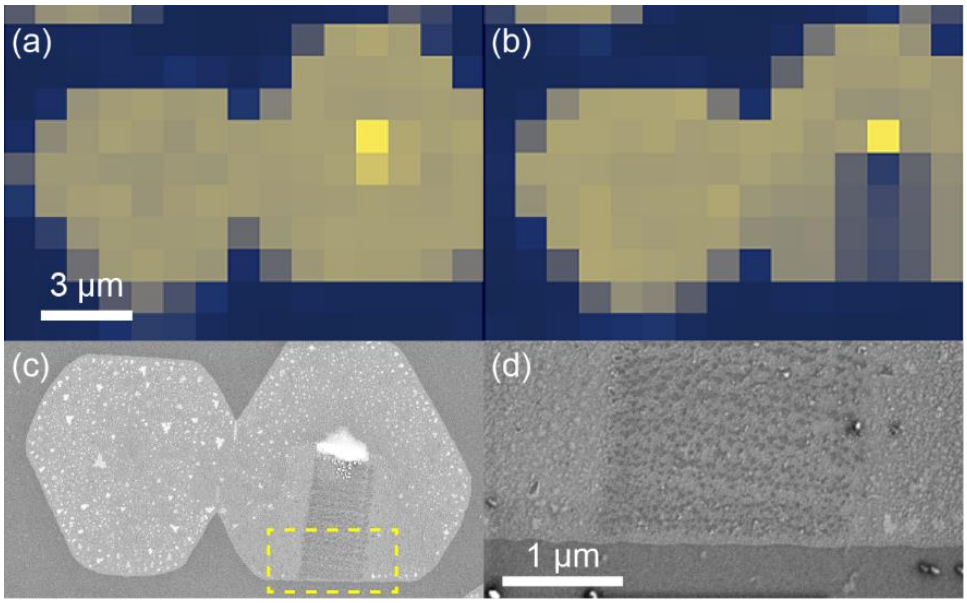

Figure 5-2. Raman mapping of the A_{1g} vibrational mode in MoS_2 crystals **(a)** before and **(b)** after 532 nm laser annealing. **(c)** SEM image of the same crystal after laser annealing and **(d)** a higher magnification SEM image corresponding to the area indicated by the yellow dashed rectangle in (c). Scale bar in (a) applies to (a-c).

With the end goal of creating MoS_2/WS_2 heterostructures and/or alloys, we switched our focus to laser-induced defect formation in WS_2 crystals to match the workflow described in Chapters 3 and 4. We first investigated the laser process parameters during the laser annealing by considering the interaction between a single monolayer WS_2 crystal and three different laser wavelengths: 532, 633, and 785 nm. These have been selected to cover a range of laser energies above and below the WS_2 bandgap. Figure 5-3 demonstrates the optical microscopy, PL intensity, Raman vibrational mode intensity, and AFM height and phase mapping of this crystal before and after laser exposure as well as SEM imaging after laser exposure. The part of the crystal exposed to the 785 nm laser, indicated by the red arrow in Figure 5-3j, does not show any significant effect in any of the images corresponding to the various characterization methods. The part of the crystal exposed to the 532 nm laser, indicated by the green arrow in Figure 5-3j, demonstrates a slight effect in the PL and Raman images, but is clearly visible in the AFM phase image. Finally, the part of the crystal exposed to the 633 nm laser, indicated by the yellow arrow

in Figure 5-3j, demonstrates a pronounced effect in optical microscopy, PL and Raman intensity, and AFM phase imaging.

Despite the evident effects of the 633 nm laser-patterned line in the above mentioned methods, the AFM height and SEM images do not demonstrate signs of significant patterning. The apparent discrepancy can be understood by considering materials properties probed by various methods. PL intensity and optical microscopy are sensitive to the electronic band structure of the material whereas Raman vibrational mode intensity and AFM phase are both sensitive to the vibrational structure of the chemical bonds. Given that the electronic band structure and vibrational chemical structure are altered by the 633 nm laser, as evidenced by the clearly distinguished lines in the corresponding images, but the topology is relatively unchanged in the AFM height and SEM images, we can infer that the laser-induced localized heating is significantly modifying the crystal structure without ablating the material.

We can infer the nature of the interaction by comparing the results at these three wavelengths in the context of the optical properties of WS_2. The 785 nm (1.58 eV) laser is below the band gap energy of monolayer WS_2 (~1.97 eV or 630 nm), resulting in minimal absorption by the WS_2. On the other hand, the 532 nm laser is above the band gap energy, resulting in sufficient absorption and thermalization to damage the crystal to an extent that it clearly affects the AFM phase image. Finally, the 633 nm laser is effectively at the exciton binding energy of monolayer WS_2, resulting in enhanced absorption by the WS_2 monolayer and the clearest effect across a range of characterization methods. Meanwhile, neither the Si nor SiO_2 of the substrate possess any relevant features in this range of wavelengths to meaningfully describe the produced effects. Consequently, we can assume that the choice of substrate is irrelevant as the localized heating is due to an interaction between the TMD crystal and the laser rather than between the substrate

and the laser. Applying this technique to other initial TMD crystals will require selecting the optimal laser wavelength accordingly.

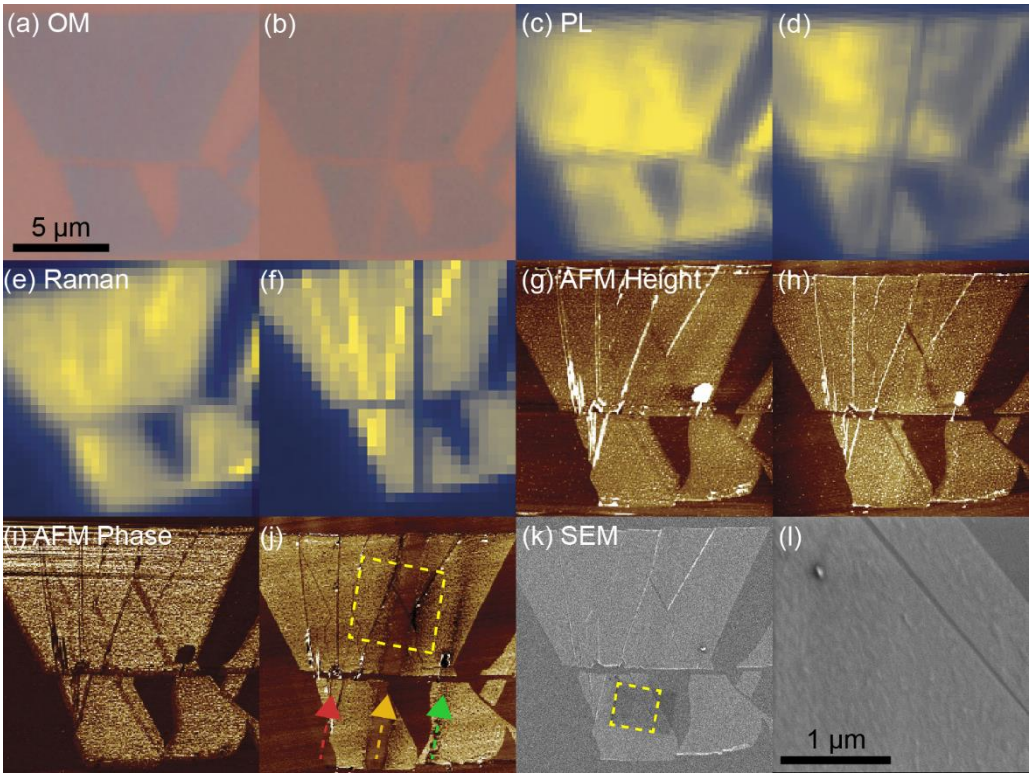

Figure 5-3. (a, b) Optical microscopy, **(c, d)** PL intensity, **(e, f)** Raman WS_2 E^1_{2g} intensity, **(g, h)** AFM height, and **(i, j)** AFM phase images of a WS_2 crystal before (left) and after (right) laser exposure. Laser exposure lines for 785, 633, and 532 nm are marked in (j) by red, yellow, and green arrows, respectively. The location of Figure 5-6 is marked in (l) by the yellow dashed square. **(k, l)** SEM image of the same crystal after laser annealing. The location of (l) is indicated by the yellow dashed square in (k). Scale bar in (a) applies to (a-k).

To clarify the nature of the interaction and the corresponding effects on the crystal, we used HAADF STEM to image a WS_2 crystal annealed with the 633 nm laser (Figure 5-4a and b). The low-intensity line passing through the STEM images from the upper center-right to lower center-left corresponds to the region of patterned laser annealing. In this case, the patterned line contains no TMD material, as demonstrated by EDS mapping (Figure 5-4c and d). However, this is likely due to the harsh conditions of the crystal transfer process which affected the defective laser annealed regions more than the pristine regions. From this imaging, we gain insight into the

spatial resolution of the laser annealing technique, appearing to be on par with the diffraction-limited spatial resolution of the laser itself. Additionally, the high degree of faceting suggests that the defect-inducing laser interaction is thermally-assisted oxidation.

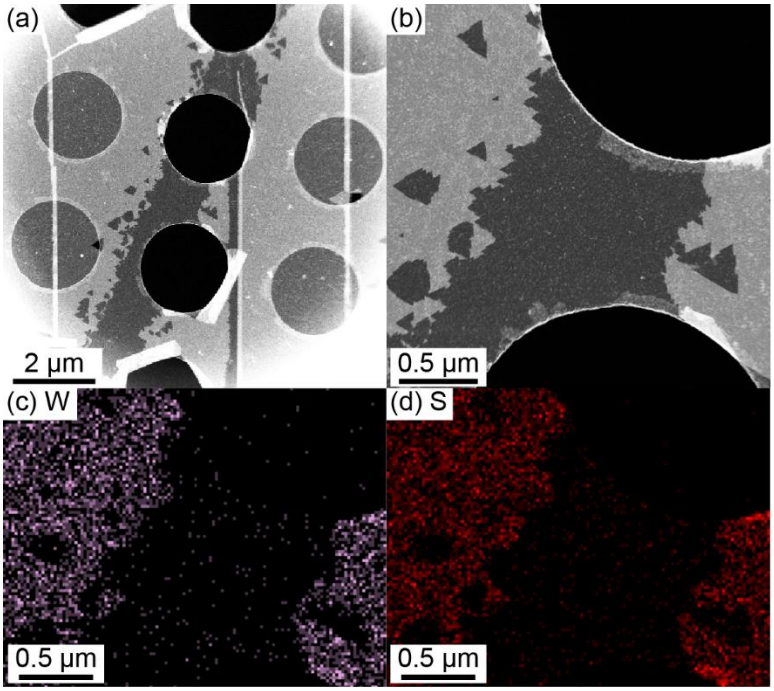

Figure 5-4. (a, b) HAADF STEM image of laser annealed WS_2. EDS mapping of **(c)** W and **(d)** S corresponding to the region shown in (b).

5.2.2 Location-controlled heterostructure formation

Following laser annealing, the sample was placed in a CVD furnace for MoS_2 growth using a procedure that is sufficient for MoS_2 growth, but is not optimized for MoS_2 nucleation, with the goal of preferential MoS_2 growth at the laser-annealed regions of WS_2. This is primarily achieved by placing the target crystals 2 cm upstream from the MoO_3 precursor powder. Figures 5-5 and 5-6 demonstrate the selective growth of MoS_2 along the 633 nm and 532 nm laser annealed lines of the crystals shown in Figure 5-3 and 5-1, respectively. The respective Raman vibrational mode intensity maps indicate higher relative amounts of MoS_2 and lower relative amounts of WS_2 along the laser annealed lines. These maps are corroborated by representative

Raman spectra of the MoS_2-rich and WS_2-rich regions (Figure 5-5d and 5-6c). The presence of two MoS_2 and two WS_2 vibrational mode intensity peaks in the MoS_2-rich regions (red dashed rectangles and spectra) indicates that some WS_2 still remains underneath the newly-grown MoS_2 layers. The presence of the same four intensity peaks in the WS_2-rich regions (cyan dashed rectangles and spectra) indicates that some MoS_2 was able to nucleate away from the laser-induced defective regions. However, the relative intensities of the MoS_2 A_{1g} vibrational mode peaks indicates that MoS_2 growth preferentially occurred along the laser-patterned lines.

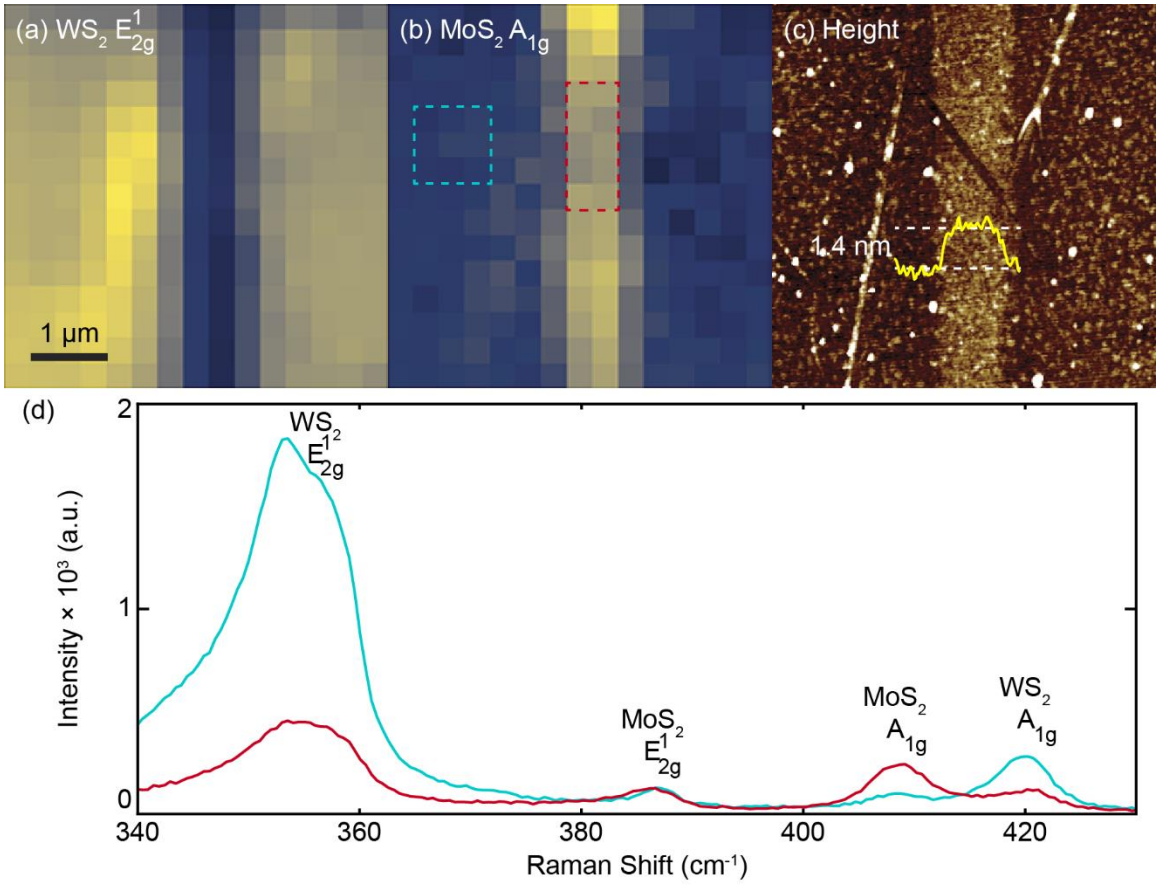

Figure 5-5. Raman intensities maps of **(a)** WS_2 E^1_{2g} and **(b)** MoS_2 A_{1g} vibrational modes corresponding to the region of interest indicated in Figure 5-3j indicated by the yellow dashed square. **(c)** AFM height map and (inset) representative height profile demonstrating the height difference between the initial WS_2 crystal and the newly grown MoS_2 patterned region. **(d)** Average Raman spectra of regions marked by the dashed rectangles in (b).

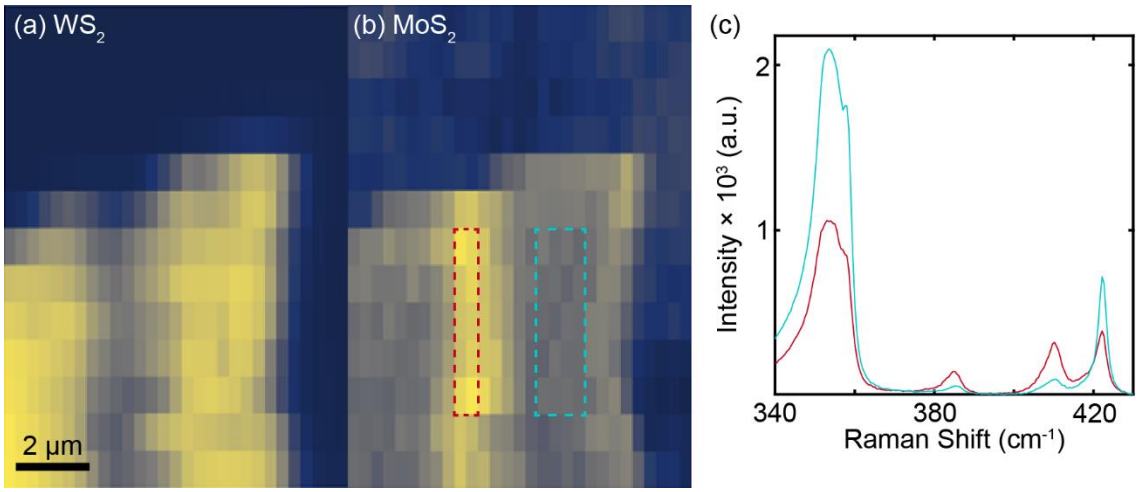

Figure 5-6. Raman mapping of **(a)** WS_2 E^1_{2g} and **(b)** MoS_2 A_{1g} vibrational mode intensities corresponding to the region of interest in Figure 5-1f following 532 nm laser annealing and MoS_2 growth. The MoS_2 intensity is stronger and the WS_2 intensity is weaker along the exposed line that was laser annealed. **(c)** Averaged Raman spectra of the regions marked by the dashed rectangles in (b). Red corresponds to the the spectra of the laser annealed line and cyan corresponds to an unexposed region. The MoS_2-like vibrational mode intensities at approximately 385 and 403 cm^{-1} are stronger in the red spectrum, whereas the WS_2-like vibrational mode intensities at approximately 355 and 420 cm^{-1} are stronger in the cyan spectrum.

Additional examples of laser-induced defect formation resulting in site-selective MoS_2 CVD of MoS_2/WS_2 heterostructures are provided in Figures 5-7 and 5-8. Unlike the 1.4 nm step height at the heterostructure site shown in Figure 5-5c, Figure 5-7i demonstrates negligible positive change in crystal thickness associated with heterostructure formation. Figure 5-8 provides a comprehensive suite of characterization techniques and corroborates the importance of laser wavelength, as originally demonstrated in Figure 5-3 – the 532 and 633 nm lasers are both capable of inducing localized crystal damage, but the 633 nm laser is superior for MoS_2 nucleation.

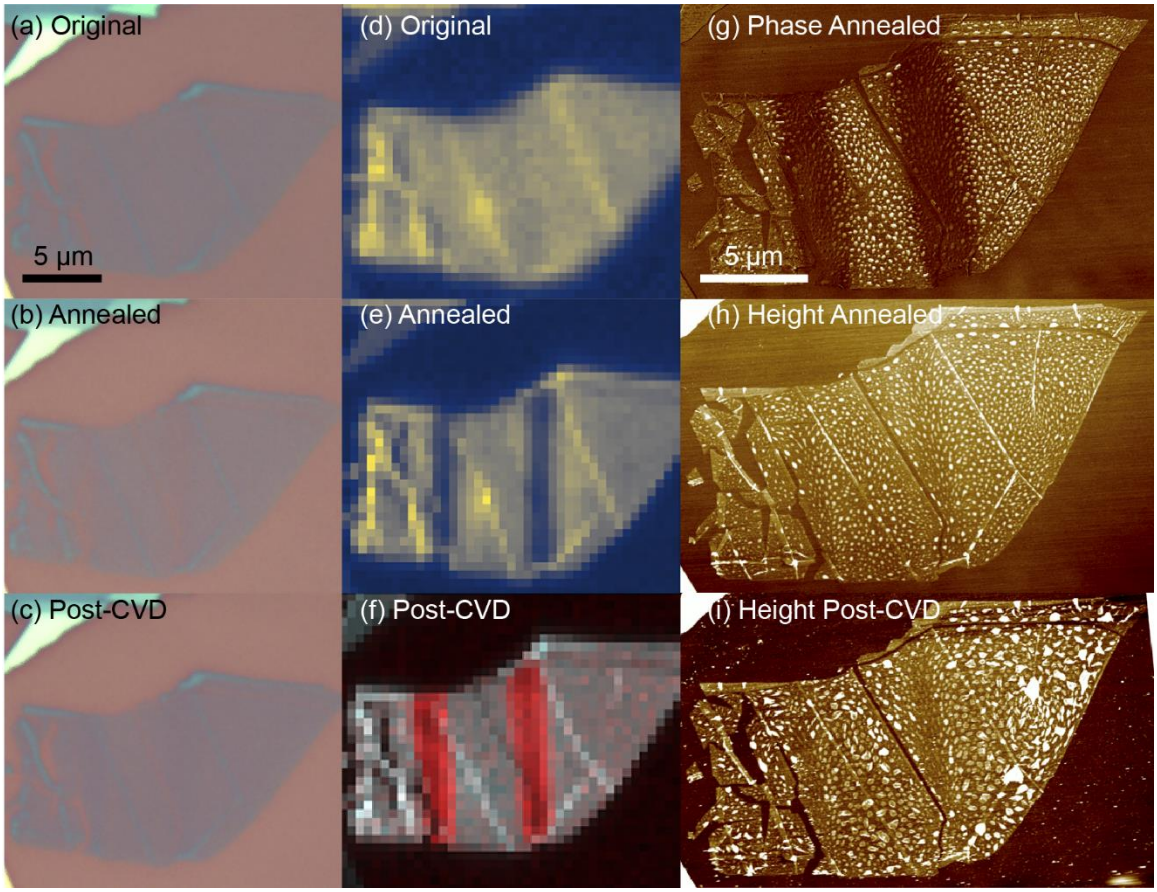

Figure 5-7. (a-c) Optical microscopy and **(d-f)** Raman mapping at each of the three processing stages of defect-driven heterostructure formation. Both laser annealing lines were formed using a 633 nm laser. Raman intensity in (d, e) correspond to the WS_2 E^1_{2g} vibrational mode. Raman intensity in (f) is gray-scale for the WS_2 E^1_{2g} mode and red for the MoS_2 A_{1g} mode. The scale bar in (a) corresponds to (a-f). **(g)** AFM phase and **(h)** height mapping following laser annealing and **(i)** height mapping following MoS_2 growth. Scale bar in (g) applies to (g-i).

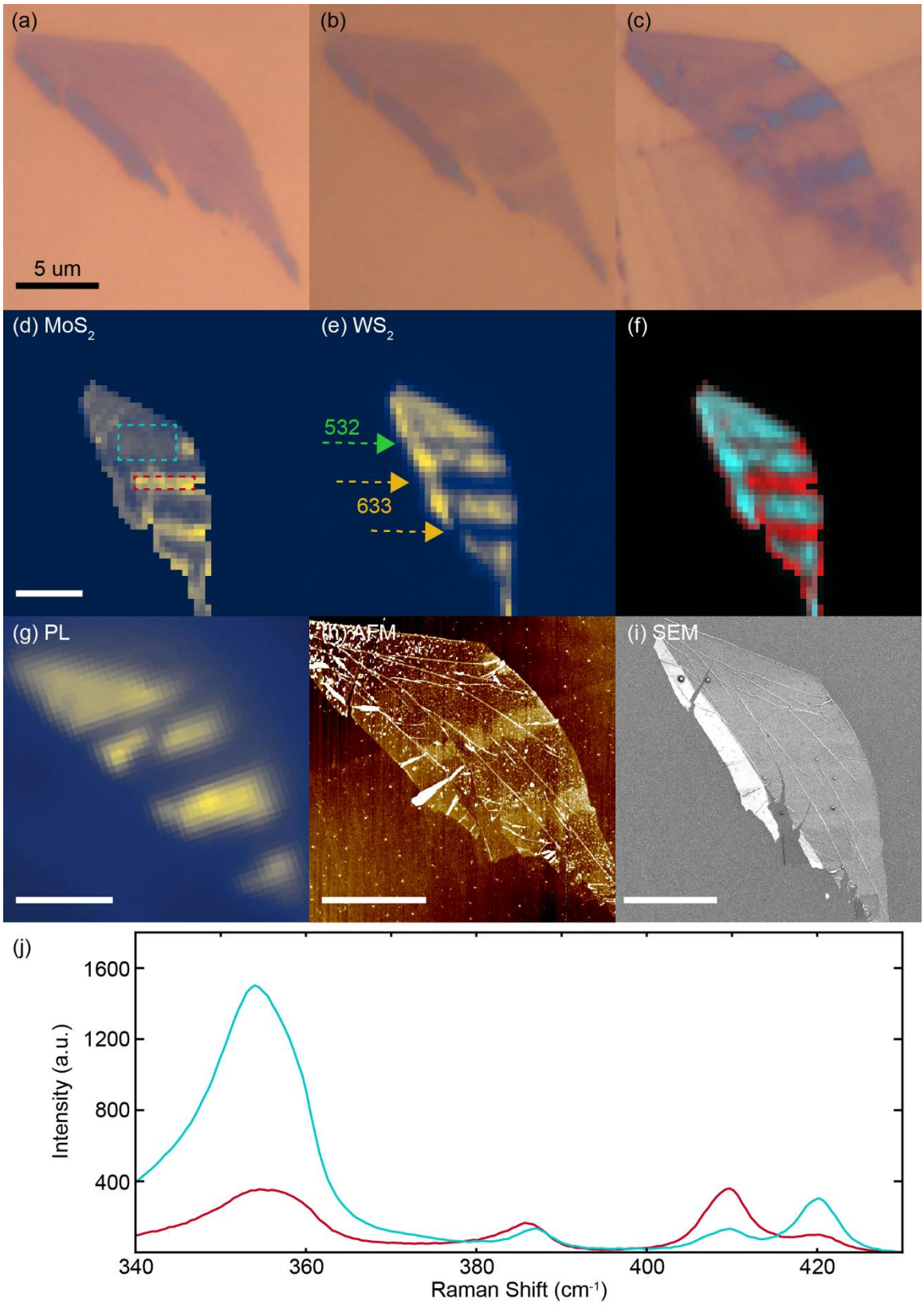
(a)
(b)
(c)
5 um
(d) MoS2
(e) WS2
532
633
(f)
(g) PL
(h) AFM
(i) SEM
(j)
Intensity (a.u.)
1600
1200
800
400
340
360
380
400
420
Raman Shift (cm-1)

Figure 5-8. (a-c) Optical microscopy at each of the three processing stages. Raman mapping of the final crystal at the **(d)** MoS_2 and **(e)** WS_2 E_{2g}^1 vibrational modes. Colored arrows in (e) correspond to the laser wavelengths used to anneal each of the three lines. **(f)** A composite image of (d, e) with the MoS_2 intensity represented in red and the WS_2 intensity represented in cyan. **(g)** PL map following laser annealing. **(h)** AFM height map following MoS_2 growth. **(i)** SEM image following laser annealing. **(j)** Averaged Raman spectra corresponding to a 633 nm laser annealed line (red) and region of unexposed WS_2 crystal (cyan) indicated by dashed rectangles in (d). The laser annealed region indicates higher Raman intensities corresponding to MoS_2 and the unexposed region indicates higher Raman intensities corresponding to WS_2. All scale bars are 5 μm. Scale bar in (a) applies to (a-c). Scale bar in (d) applies to (d-f).

5.2.3 Laser power effects

To investigate the effects of laser power, two different laser powers were each used to expose two lines in a sample WS_2 crystal. Marked by the white arrows in the lower right corner of Figure 5-9a, two lines were exposed using a 532 nm diffraction-limited laser with 9.29 mW. Marked by the black arrows in the upper left corner of Figure 5-9a, two lines were exposed with the same laser set to 4.645 mW, or half of the power of the previous two lines. The rastering step size was fixed at 0.5 μm/pixel in all cases. The two inner lines were exposed with dwell times of 3 s/pixel while the two outer lines were exposed with dwell times of 5 s/pixel.

Following laser annealing, the high-power laser-patterned lines are clearly visible by optical microscopy in Figure 5-9a, whereas the low-power laser-patterned lines are not evident. Considering laser-pattern line visibility as a proxy for crystal damage, this result confirms the intuitive assumption that laser power is positively correlated with crystal damage. Despite the lack of visible lines in the low-power exposure regions, all four lines do appear in the AFM height map in Figure 5-9b following the MoS_2 CVD growth step, thus demonstrating that the threshold level of laser-induced damage necessary for MoS_2 patterning is surpassed prior to detection by optical microscopy. However, the width and thickness of the MoS_2 along the high-power laser-patterned lines are greater than those of the MoS_2 along the low-power laser-patterned lines, indicating that the extent of WS_2 crystal damage beyond the threshold necessary

for selective MoS_2 growth is a relevant parameter in understanding how the MoS_2 will grow. That is, nucleation and growth become increasingly favorable at the laser annealed locations as those locations become increasingly damaged. Finally, by comparing the Raman spectra (Figure 5-9c) along the high- and low-power laser-patterned lines and in an unexposed region, it is evident in that both MoS_2 and WS_2 are present along both laser-patterned lines, while no detectable amounts of MoS_2 are present in the unexposed region—a level of selectivity beyond what has already been demonstrated in previous figures.

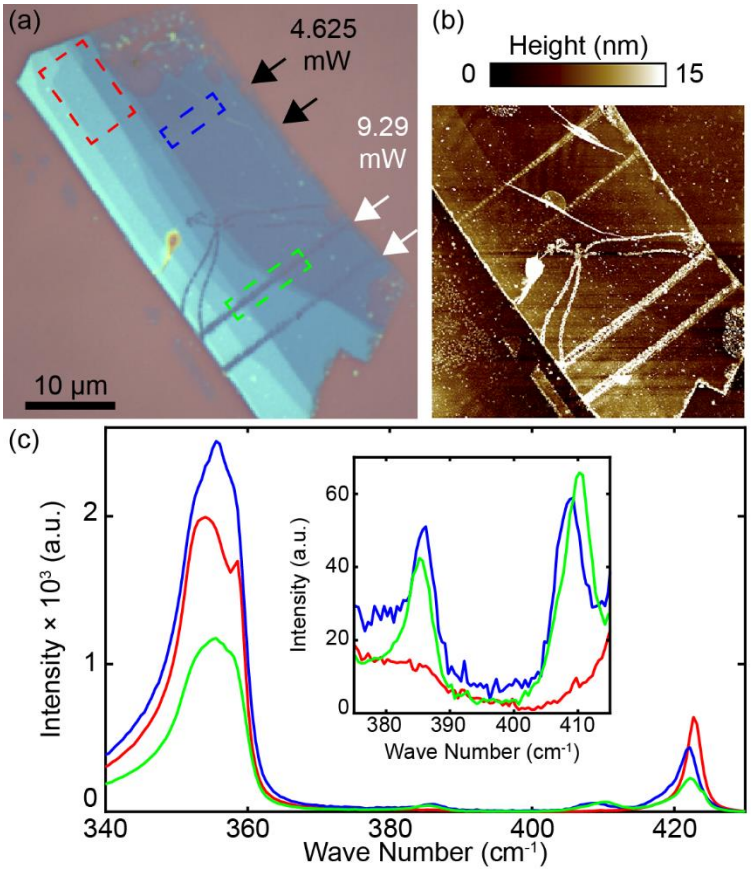

Figure 5-9. (a) Optical microscopy of WS_2 following laser annealing. The black and white arrows mark the laser-patterned lines using 4.625 and 9.29 mW laser powers, respectively. **(b)** AFM height map following patterned growth of MoS_2. **(c)** Average Raman spectra of regions marked in (a) by the dashed rectangles. The green and blue spectra containing both MoS_2 and WS_2 vibrational mode intensity peaks correspond to regions with high- and low-power laser exposure, respectively, while the red spectrum containing only WS_2 vibrational mode intensity peaks corresponds to an unexposed region.

5.3 **Conclusions**

In conclusion, we have demonstrated laser exposure as a reliable method for direct-write patterning of defects in TMD crystals. The spatial distribution of defects is shown to correlate strongly with subsequent MoS_2 nucleation by CVD, enabling site selectivity in heterostructure formation. We establish a relationship between relevant laser parameters (*e.g.*, power and wavelength) and efficacy of defect and heterostructure formation. We also demonstrate the efficacy of identifying threshold levels of defects necessary for heterostructure formation by various characterization techniques. This direct-write technique will simplify the process of heterostructure patterning and enable the routine fabrication of complex device architectures necessary for various advanced applications.

Chapter 6: Nanopores in Transition Metal Dichalcogenides with Controlled Size and Edge Properties

Nanopores in atomically thin membranes have a variety of demonstrated applications including sensing, filtration, energy, and catalysis. The functionality of these devices is governed by the chemistry and geometry of the nanopore edge, but their simultaneous control remains elusive. This chapter begins with analytical and Monte Carlo modeling of nanopore growth in a 2D TMD lattice. This provides a fundamental understanding of the parameter relations that can be applied to experimental data analysis. Next, we discuss the results of *in situ* annealing studies within aberration-corrected STEM in which we experimentally investigate the relationship between annealing temperature, nanopore edge reconstruction, and nanopore growth rate. The study demonstrates a method of controlled production of nanopores with desired chemistries and geometries in 2D TMDs and yields the following results: (1) nanopore edges become more ordered at higher annealing temperatures in the range of 400-700°C yielding two distinct growth regimes and (2) nanopore radius increases linearly with time at an Arrhenius temperature-dependent rate. These results will enable the fabrication of nanopore devices and processing methods for desired geometries and chemistries of nanopore edges in a range of atomically thin materials.

6.1 **Introduction**

In the previous three chapters, defect engineering has been demonstrated in the context of enabling spatial and compositional control in 2D TMD heterostructure and alloy crystals. In this chapter, these defect engineering is investigated in the context of processing suspended 2D TMD nanoporous membranes.

The atomic thinness of 2D materials such as graphene, boron nitride, and layered TMDs represents an ultimate limit of membrane scalability.[186–188] Nanometer-scale pores (nanopores) in 2D membranes have been demonstrated in applications including sensing (DNA translocation),[189–192] filtration and desalination,[193–197] reverse electrodialysis,[198] or catalysis.[199]

While the thinness of membranes is an enabling factor, the most important parameter driving device performance is the atomic-level control of the nanopore size, geometry, and chemical termination.[193,194,197,200] For example, the water desalination performance (*e.g.*, water permeability and salt rejection rate) of MoS_2 nanopores strongly depends of their chemical termination.[197] A scalable production of an ensemble of nanopores with narrow distribution of geometrical and chemical properties is critical for applications where a macroscopic area of the membrane is needed, such as filtration.

The most common technique to form nanopores so far has been electron beam drilling,[189,190,198,200,201] *i.e.*, knock-on damage from an electron beam in a TEM. Although this technique allows for precise positioning of the nanopores and provides control of the number of nanopores created, it is a low-throughput and expensive method with limited control of the nanopore edges. Similarly, the electrical-breakdown method[202,203] is limited to production of a single nanopore with controlled size, but not the shape. An alternative and more scalable method for nanopore formation is based on ion-beam irradiation,[195,204] which offers some control of the pore sizes, but still fails to address the problem of the edge structure. Finally, oxidative annealing[61] in air results in an uncontrollable number of relatively large (hundreds of nm) pores with faceted edges defined by the crystal symmetry. Because each of these methods offers a set of trade-offs, no universal method exists to control pore creation (*e.g.*, number and location) as well as processing (*e.g.*, size, shape, and edge chemistry).

In this chapter, we use modeling and experimental techniques to study the relevant parameters of reproducible processing of nanopores with desirable sizes, shapes, and edge chemistry. We experimentally study the growth and edge reconstruction of vacuum annealed nanopores in 2D TMDs that are initially seeded by a focused electron beam in STEM, but our

methods and findings are generally applicable regardless of the seeding method (electrons, ion irradiation, etc.). We identify two distinct nanopore growth regimes: (a) *isotropic growth* of pores with disordered edges, for annealing temperatures ≤500°C, and (b) *faceted growth* of hexagonal pores with well-defined chemical terminations for annealing temperatures ≥600°C. We establish basic understanding of the underlying processes defining the growth regimes and identify the relevant activation energy for the thermal nanopore growth. Taken together, these insights will enable rational processing of nanopores with targeted size and edge properties.

6.2 **Results**

6.2.1 Analytical modeling

To quantitatively understand TMD nanopore growth dynamics, we developed a simple model to capture the relevant physics of pore evolution. We consider pore growth as an ensemble of stochastic events at the edge of a pore where each edge atom (defined as an atom neighboring an empty atomic column, see Figure 6-1) was assigned a fixed probability of removal per unit time, p_r.

We assume the number of edge atoms is given by $N = 2\pi a * r$ where r is the average radius of the pore, and a is a structural constant that depends on the lattice constant and crystal properties. The number of atoms removed from the edge during time dt is $dN = p_r N(t) dt$.

Atomic removal contributes to the increase in the pore area *via* $dA = \alpha dN$, where α is the average surface area for each atom. Combining the equations and defining $\beta = a\alpha$, we come the equations:

$$\frac{dA}{dt} = p_r N \alpha = 2\pi * r * \beta * p_r \qquad 6\text{-}1$$

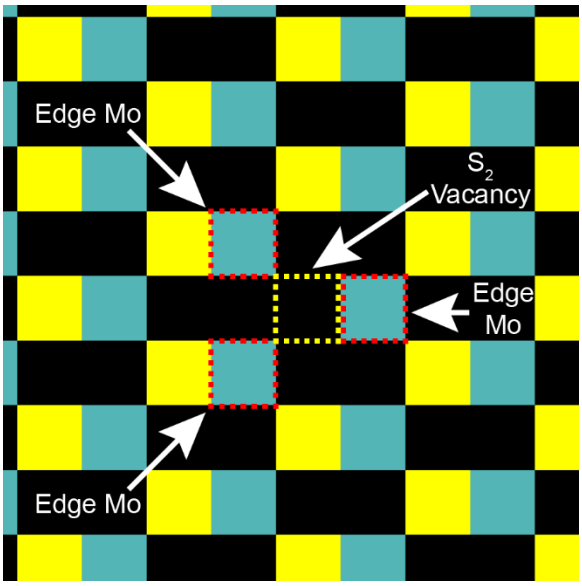

Figure 6-1. Initial state of nanopore growth with one disulfur vacancy (V_{S_2}) and three edge Mo atoms.

From the area of a circle, we can also state:

$$\frac{dA}{dt} = 2\pi * r * \frac{dr}{dt} \tag{6-2}$$

Combining these equations together, we get:

$$\frac{dr}{dt} = \beta * p_r \tag{6-3}$$

These results lead to the following analytical model of a linear evolution of the average nanopore radius:

$$r(t) = \beta \cdot p_r \cdot (t + t_0) = r_0 + \beta \cdot p_r \cdot t \tag{6-4}$$

In this model, the proportionality parameter β is a structural parameter depending only on the details of the crystal structure, $R_0 = \beta \cdot p_r \cdot t_0$ is the initial radius of the pore, and t_0 is initial time needed for pore to grow to its initial value.

6.2.2 Monte Carlo modeling

Putting this analytical model into practice to understand the emergent behavior of the system, we performed Monte Carlo simulations of pore growth in a 2D hexagonal crystal lattice. As demonstrated in Figure 6-1, a single vacancy was created at the center of the lattice and the system was subjected to a simulated annealing process until the pore area encompassed 1,500 atomic columns (30% of simulated crystal area). For simplicity, we consider identical probability of removal for both Mo and S edge atoms. This model is sufficient for describing the relevant processes as the rate limiting step of pore growth is governed by the lower among these two probability values. As will be discussed further in Section 6.2.4, the rate limiting step in MoS_2 pore growth is the removal of Mo because it is more stable.

The Monte Carlo simulations (Figure 6-2a and c) demonstrate the evolution of the pore morphologies as a function of time (*i.e.*, iteration steps) for low ($p_r = 0.05$) and high ($p_r = 0.95$) removal probabilities. At low removal probability, the simulated nanopore edges are rough whereas the nanopore edges appear highly faceted for high removal probability. From the simulations that generated these images, the nanopore perimeter (*i.e.*, number of edge atomic columns) and area (*i.e.*, number of removed atomic columns) were calculated and plotted as a function of time (Figure 6-2b and d). The perimeter and area show linear and quadratic dependence on time, respectively, for both removal probabilities.

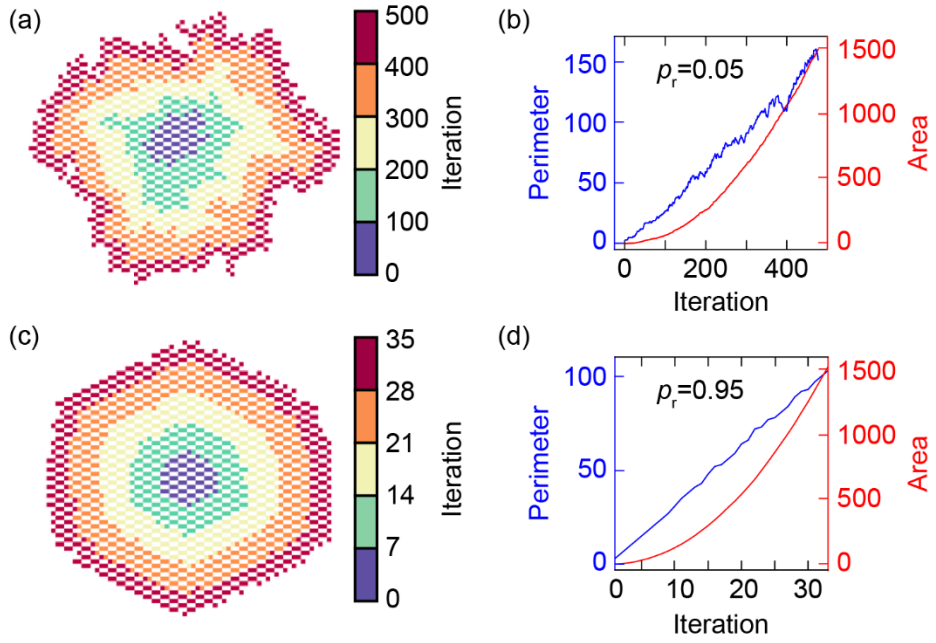

Figure 6-2. (a, b) Monte Carlo simulations of the pore perimeter, area, and morphology evolution during simulated pore growth with $p_r = 0.05$ and **(c, d)** $p_r = 0.95$. Color scales in (a, c) correspond to the iteration step when the atomic column becomes fully removed. Pore area demonstrates less statistical noise, making it a more reliable metric for pore growth. Removal probability has a positive correlation with extent of faceting.

From the Monte Carlo simulations, we calculate the average pore radius as $r = \sqrt{A/\pi}$ and the average radial growth rate as $G_R = \Delta r/\Delta t$ and analyze these results as a function of p_r. As shown in Figure 6-3a, G_R is linearly proportional to p_r across a significant range of p_r values. However, as edge atom removal becomes more likely (*i.e.*, $p_r > 0.8$), faceting becomes inevitable, resulting in a deviation from linearity.

To quantify the faceting effect, we define the faceting parameter, f_p, which calculates the percentage of edge atoms in faceted configuration for each simulated pore shape (Figure 6-3b). For disordered pores, $f_p \approx 0.5$, whereas for fully faceted pores, $f_p \to 1$. An edge atom is labeled as part of a facet if it and its two nearest neighbor edge atoms occupy the same crystallographic axis and have the same coordination number corresponding to either a zigzag (ZZ), armchair (AC), or Klein edge. ZZ and AC edges are described in Figure 1-4. Klein edges are S-terminated

ZZ edges without the edge S atoms, resulting in dangling transition metal atoms. Any atom that does not belong to a facet is labeled as part of a rough edge. Faceted and rough edges are equally distributed for all low probabilities until $p_r \approx 0.80$. As p_r approaches unity, faceting becomes ubiquitous. The ~12% frequency of rough edges at $p_r = 1$ corresponds to two atoms per side nearest to the hexagonal vertices for each of the six sides of the pore while the perimeter was equal to approximately 100. With larger pore perimeters, this value will decrease to zero.

It is worth noting that the faceting is a natural consequence of a large removal probability as many neighboring edge atoms are likely to be removed at the same time and that no additional physical processes or differences in binding energy between faceted and disordered atoms are required to explain the observed pore faceting.

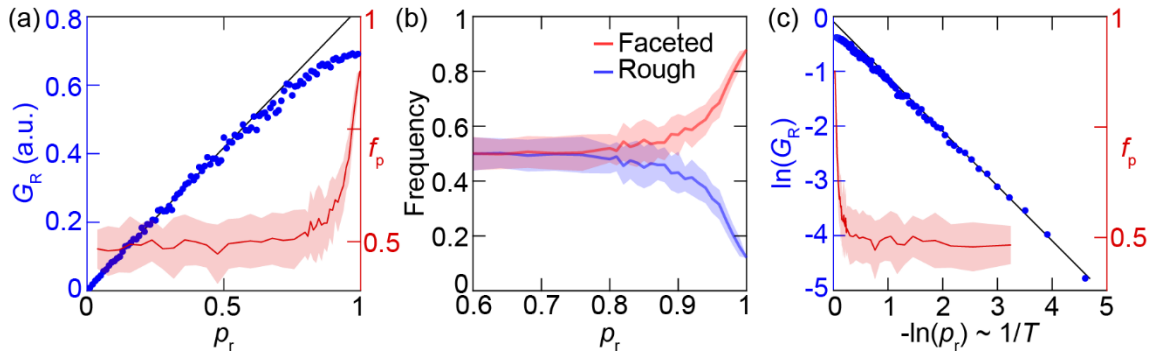

Figure 6-3. (a) Radial growth rate G_R and faceting parameter f_p as a function of removal probability p_r. **(b)** The distribution of rough and faceted edges in the final configuration of Monte Carlo simulated nanopores as a function of removal probability. The solid lines and shaded regions represent the average and standard deviation of 30 simulations at each probability. Probability values are in increments of 0.05 in the range $p_r = 0.6 - 0.8$ and in increments of 0.01 in the range $p_r = 0.8 - 1$. **(c)** Log-log plot of the results shown in (a) such that the *x*-axis is linearly proportional to inverse temperature showing the Arrhenius behavior.

As the pore growth rate is related to edge atom removal probability, which in turn is a thermally-driven property, we can use the Arrhenius equation $p_r = c_1 \exp\left(\frac{-E_a}{k_B T}\right)$ to calculate the activation energy E_a for the pore growth. Figure 6-3c shows the relation between the radial

growth rate and removal probability. Each probability in Figure 6-3c corresponds to a given experimental temperature, thus by observing the pore growth as a function of temperature, the activation energy can be extracted from the slope of the fitted Arrhenius plot. In particular, E_a can be calculated from the slope of the radial growth rate that is equal to $\frac{-E_a}{k_B}$. We next apply the same analysis to experimentally obtained pore growth results to empirically extract the pore growth activation energy, a parameter that is highly relevant for the controlled pore growth process.

6.2.3 Microscopy experimental design

MoS_2 monolayer crystals were first synthesized by CVD. To form nanoscopic pores within as-grown MoS_2 crystals and investigate their temperature-dependent evolution, the crystals were then transferred onto *in situ* heating TEM grids for STEM studies. A statistically significant number of individual nanopores of different sizes (0.2-45 nm^2) were formed in the crystals by sputtering with a focused electron beam (electron-beam drilling) and characterized at room temperature in an aberration-corrected JEOL JEM-ARM200F STEM. For these studies, we used an 80 kV electron beam with a current density of 1.7 nA/cm^2 to minimize the effects of knock-on damage and any associated artifacts. The temperature of the sample was then rapidly increased *in situ* to 400°C at the rate of 1000°C/ms, where it was kept for several minutes and then rapidly cooled down to room temperature for STEM imaging. To decouple any electron beam effects from temperature-dependent processes, the electron beam was blanked during the heating, annealing, and cooling steps. In addition to the 400°C annealing, we repeated the same procedure for 450, 500, 600, and 700°C. Similar sets of measurements were performed on CVD-grown WSe_2 and $Mo_xW_{1-x}S_2$ ($x \approx 0.1$) crystals to ensure that our findings are generally applicable to different TMDs.

Figure 6-4 demonstrates an intermediate step of the experimental data analysis workflow. Figure 6-4a shows a representative STEM image that has been Fourier filtered and contrast adjusted. This image is inputted into the built-in MATLAB Image Segmenter app. The regions of interest (locations of nanopores) are manually selected and then the Active Contours function is used to identify the nanopore edge. Figure 6-4b shows the binary image output such that the white regions correspond to the pixels of the nanopores in Figure 6-4a. This can be inputted into the built-in MATLAB Image Region Analyzer app to calculate object properties such as area and perimeter that can be applied to quantitative analysis. Figure 6-4c overlays the input (Figure 6-4a) and output (Figure 6-4b) to demonstrate the accuracy of the object identification method.

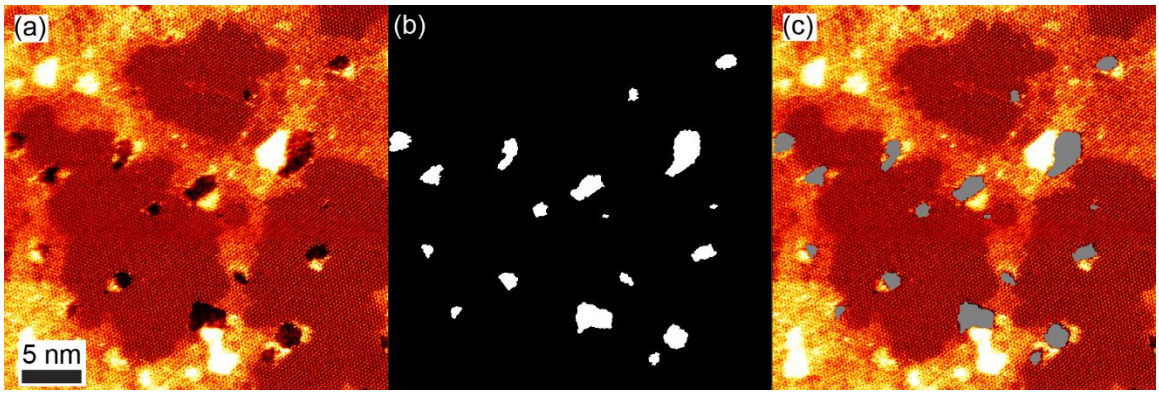

Figure 6-4. (a) Fourier filtered and contrast adjusted STEM image of nanopores in MoS_2. **(b)** Binary image of nanopore objects identified by built-in MATLAB Image Segmenter app. **(c)** Comparison of original STEM image and overlaid nanopore objects identified.

6.2.4 Nanopore edge structure

To assess the relationship between annealing temperature and nanopore edge structure, representative MoS_2 nanopores annealed at 400°C and 700°C are shown in Figure 6-5a and b. A larger sampling at each annealing temperature for MoS_2 is provided in Figure 6-6 and analogous samplings are provided for WSe_2 and $Mo_xW_{1-x}S_2$ ($x \approx 0.1$) in Figures 6-7 and 6-8, respectively. For ease of comparison and to avoid possible size-effects, the pores displayed in Figure 6-5a and b are of comparable size.

In the case of 400°C annealing (Figure 6-5a), pore growth is isotropic, resulting in a relatively circular pore with minimally defined edges (*isotropic growth regime*, analogous to Figure 6-2a). With increasing annealing temperature, however, the pores become increasingly faceted, favoring the ZZ crystal orientation, the most energetically stable edge orientation.[61,205] This transition is demonstrated in Figure 6-6 and results in the formation of a nearly perfect hexagonal nanopore, shown in Figure 6-5b, that was annealed at 700°C for 3 min (*faceted growth regime*, analogous to Figure 6-2c). In this structure, the nanopore has six linear facets corresponding to the three-fold symmetry of the ZZ crystal orientation, as shown in an idealized schematic of the edge structure in Figure 6-5c.

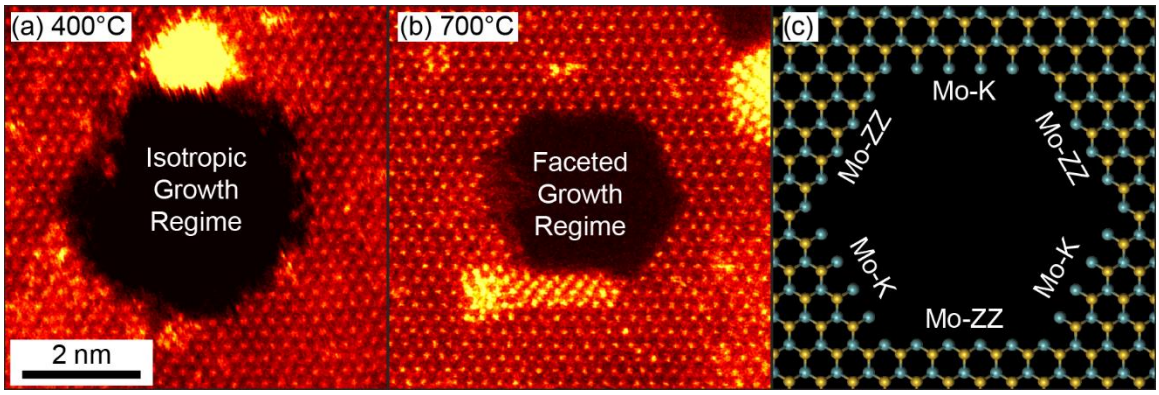

Figure 6-5. Room temperature HAADF STEM images of MoS_2 nanopores annealed at **(a)** 400°C for 6 min and **(b)** 700°C for 3 min. The bright dots correspond to Mo atoms and the fainter dots correspond to pairs of S atoms. Large high-intensity areas at the pore edges are comprised of Mo and/or S atoms that have been displaced out of the monolayer crystal lattice. Mo-Klein and Mo-ZZ edges are predominantly present in (b). **(c)** Schematic of Mo-terminated hexagonal pore faceting demonstrated in (b). Cyan corresponds to Mo and yellow corresponds to S.

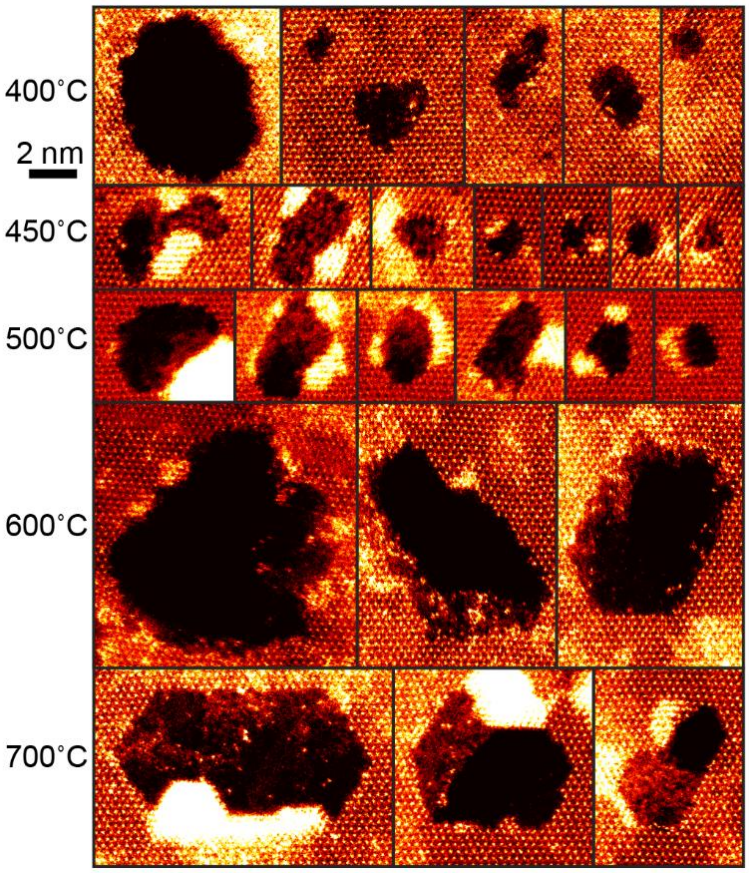

Figure 6-6. MoS_2 nanopores following annealing at 400, 450, 500, 600, and 700°C.

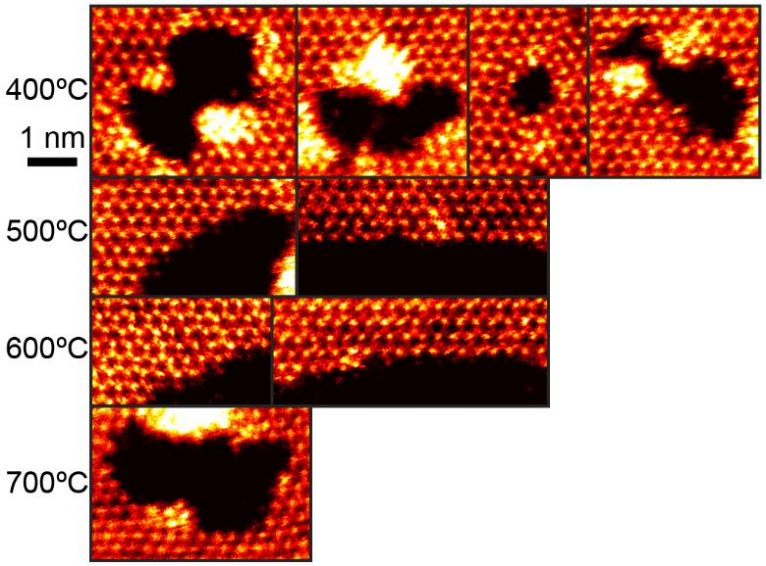

Figure 6-7. WSe_2 nanopores following annealing at 400, 500, 600, and 700°C. Images at 500 and 600°C show stability of both the ZZ and AC edge orientations.

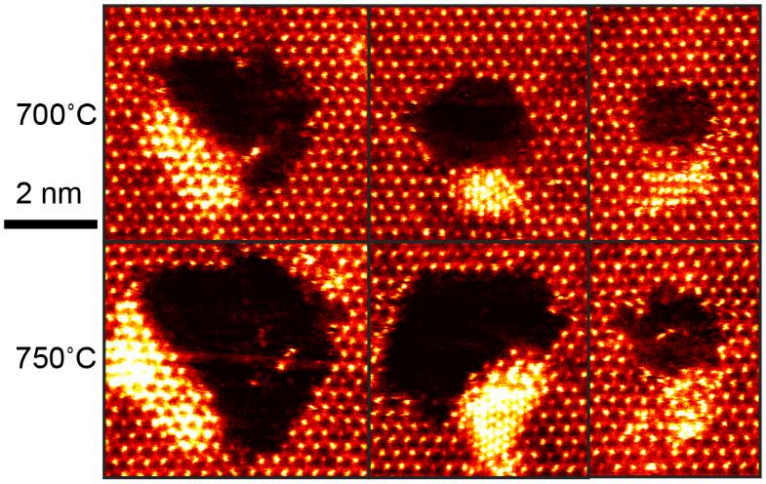

Figure 6-8. $Mo_xW_{1-x}S_2$ ($x \approx 0.1$) nanopores following annealing at 700 and 750°C.

As the unit cell of MoS_2 is comprised of one Mo atom in an atomic column and two S atoms in the neighboring atomic column, the resulting ZZ-terminated nanopore would be assumed to have alternating facets terminated by Mo-ZZ and S-ZZ, as has been demonstrated in 2D hexagonal boron nitride.[206] Instead, we observe that most of the S atoms of the intended S-ZZ facet have been displaced, resulting in an extended Mo-Klein edge,[70,207–209] as shown in Figure 6-5c. DFT calculations[210] and experimental results[211] have demonstrated that extended Klein edges are stable in graphene, so their presence in MoS_2 is not surprising. However, we only observe extended Klein edges in replacement of S-ZZ edges (*i.e.*, not in replacement of Mo-ZZ edges), indicating that S atoms are significantly more susceptible to thermal displacement than Mo atoms. These results are in agreement with DFT[64,70,205,208,209,212] and experimental results[64,70,205,208,209] regarding the formation energies of MoS_2 crystal edges and intrinsic bulk defects: formation of a Mo-Klein edge is up to 0.2 eV/Å more favorable than a S-ZZ edge[208] and the formation of V_s is 2-7 eV more favorable than V_{Mo} over the stable chemical potential range of MoS_2.[64] Furthermore, it has been suggested that the Mo-Klein edge is an intermediate state that reconstructs to a Mo-replaced S edge following high temperature vacuum annealing (800°C)[70] and that TMD pore edge reconstruction is affected by the local chemical environment

(*e.g.*, carbon contamination), which is a function of annealing temperature.[213] Our results expand on these findings by following the pore evolution over a range of temperatures between 400-700°C to demonstrate the onset of faceting and the progression from isotropic edges to the formation of Mo-ZZ and Mo-Klein edges. The identification of 600-700°C as the minimum temperature range required to produce fully faceted and Mo-terminated MoS_2 nanopores, such as the pore shown in Figure 6-5b and c and demonstrated again in greater clarity in Figure 6-9, is important because DFT and molecular dynamics simulation results[192] suggest that this edge structure is optimal for DNA base detection compared to other edge structures of MoS_2 nanopores or any edge structure of graphene nanopores.

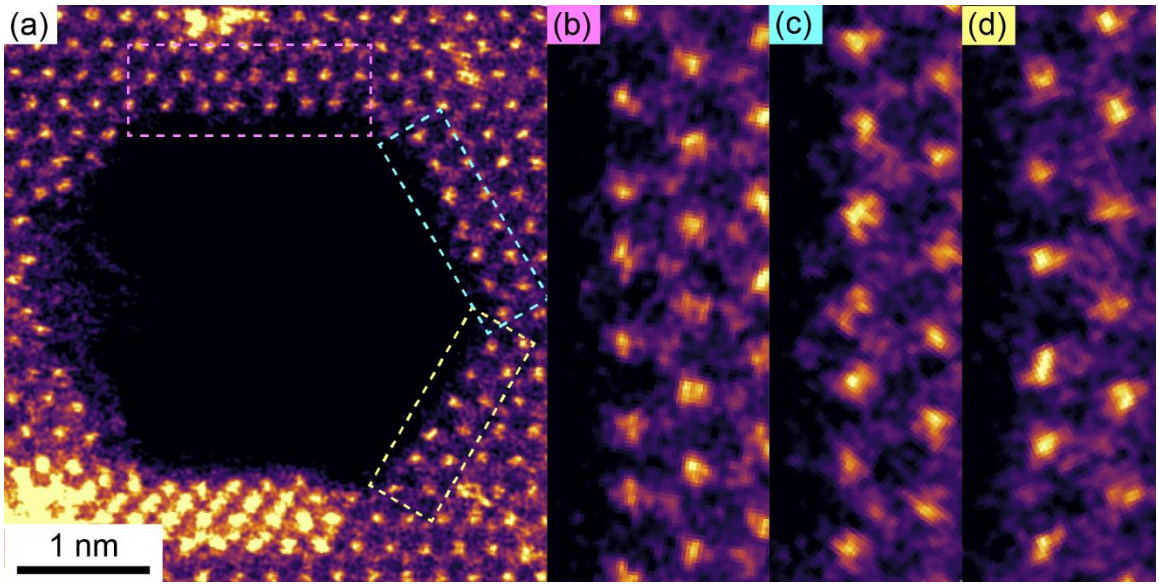

Figure 6-9. (a) High magnification STEM image of MoS_2 nanopore shown in Figure 6-5b. **(b-d)** Higher magnification images corresponding to colored dashed rectangles in (a) demonstrating (b, d) Mo-Klein and (c) Mo-ZZ edges.

6.2.5 Nanopore growth rate

Having investigated the structure of faceted and isotropic nanopores, we next focus on the growth rate to develop a greater understanding of the factors relevant to nanopore size control. Figure 6-10a-c shows a representative set of time-dependent images obtained for a single

nanopore in MoS_2 annealed at 450°C. Using the object identification workflow as previously described, the areas of the pores were measured and compared as a function of the annealing time and temperature. Figure 6-10d shows the measured average radii of seven pores with different starting sizes as a function of annealing time at 450°C. Pore growth was measured until pore-to-pore separation was reduced to within 3 unit cells to avoid any artifacts due to the pore vicinity or possible merging. Because each pore had a different starting size prior to the first annealing stage, the relationship between individual pore radius and time shown in Figure 6-10d represents a set of pore growth snapshots at specific pore sizes. In these limited ranges of growth, nanopore radius appears linearly-dependent on the annealing time for each individual pore, in agreement with the analytical and Monte Carlo models discussed in Sections 6.2.1 and 6.2.2. We further calculate the radial growth rate $G_{\mathrm{R}} = dr/dt$ and show it is independent of the nanopore size (Figure 6-10e).

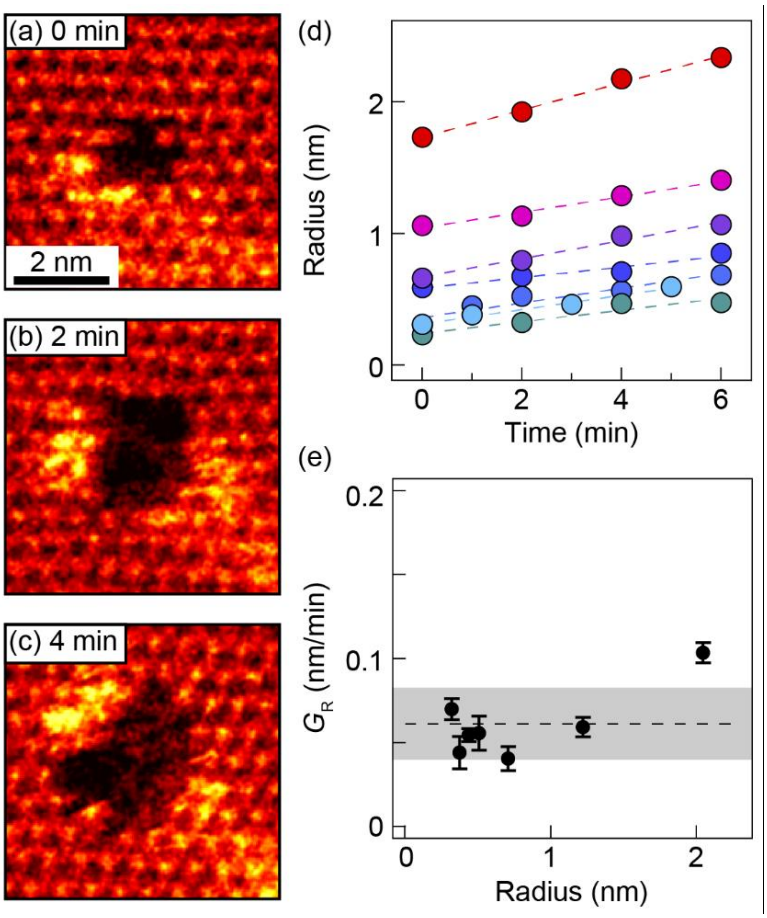

Figure 6-10. (a-c) A representative set of HAADF STEM images of a single nanopore in MoS_2 as a function of the annealing time (indicated in the images) at 450°C. **(d)** Average radii of seven different nanopores (shown in different colors) of different initial sizes as a function of annealing time at 450°C. **(e)** Radial growth rate G_R is independent of pore radius r. Dashed line represents the average growth rate and shaded region represents the standard deviation.

The results obtained from individual pores of different starting sizes and annealed at the same temperature can be combined to create a composite plot of radius *vs.* effective time (Figure 6-11a-c), as simulations and experiments confirmed linear radial growth with time. For example, when considering the growth of smaller pores with the initial radius $r_{\text{small}}^{(i)}$, these will reach the final radius $r_{\text{small}}^{(f)}$ during the annealing step. By simultaneously monitoring and plotting growth of larger pores with the starting radius $r_{\text{large}}^{(i)} = r_{\text{small}}^{(f)}$ under identical annealing conditions, we can access a significantly broader range of annealing times than by monitoring individual pores. In

practice, $r_{\text{small}}^{(f)}$ and $r_{\text{large}}^{(i)}$ are not exactly equal. Therefore, time offsets are introduced (see Equation 6-4) to optimize the linear fit of the pore radius. In effect, this puts pores of similar size at a similar effective time, regardless of the actual chronology of those measurements. The resulting analysis for MoS_2 nanopores annealed at 450, 500, 600, and 700°C is shown in Figure 6-11a-c, respectively. As predicted by the Monte Carlo results shown in Figure 6-3a and c, the radial growth rate G_R increases with temperature, as summarized in an Arrhenius plot shown in Figure 6-11d. From the relationship between pore growth rate and temperature derived in the Monte Carlo analysis, an activation energy of $E_a = 0.39$ eV was calculated by fitting a line to this data.

From these results, we can infer that MoS_2 nanopore radius grows linearly with time over a range of temperatures from 450 to 700°C. The growth rate within this temperature range spans more than an order of magnitude, thus enabling a trade-off of nanopore processing metrics between high growth rate at higher temperatures and control at lower temperatures. Comparable temperature ranges for linear nanopore radius growth and corresponding Arrhenius relations should exist for other 2D materials. For example, these results are corroborated by similar contemporaneous experiments performed by Thomsen *et al.* that study the growth dynamics of graphene nanopores.[214] Through the consideration of nanopore growth rate, as well as other factors such as edge chemistry, the optimal nanopore processing parameters (*e.g.*, annealing temperature and duration) can be selected to produce nanopores with preferred device performance properties. For example, multi-step growth procedures could be developed to benefit initially from the size control of the slower, albeit isotropic, growth at low-temperature and then achieve the edge termination control during high-temperature faceted growth regime.

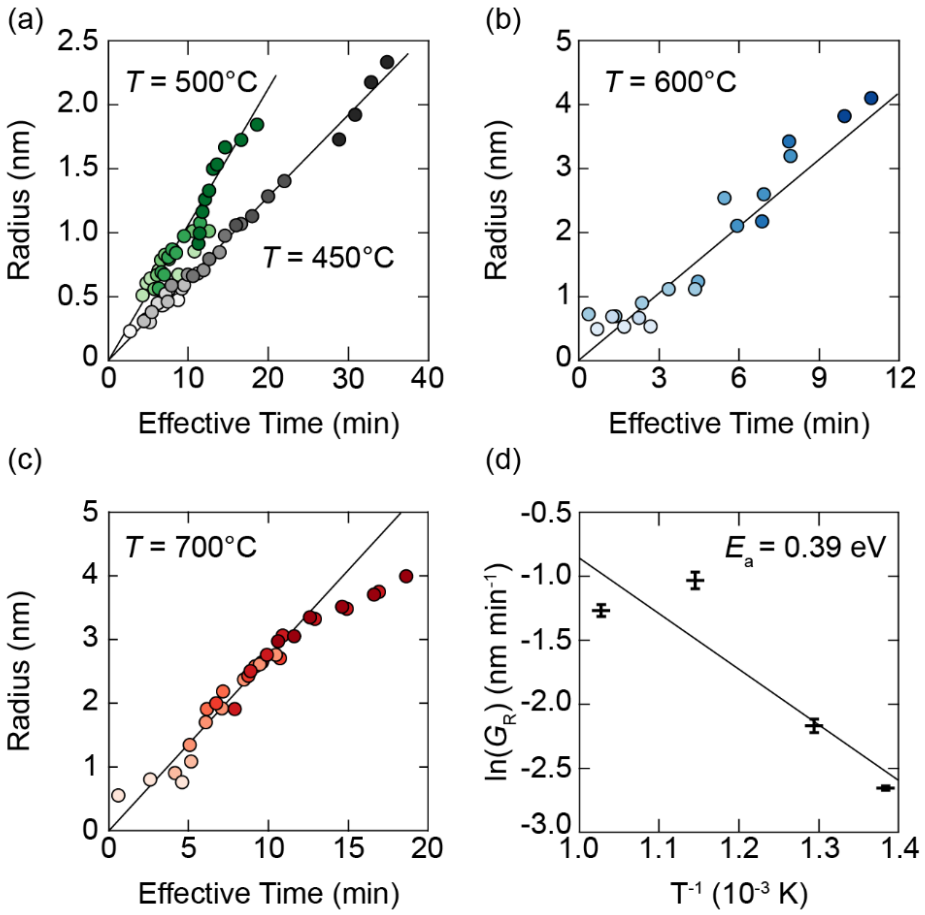

Figure 6-11. Combined data sets and corresponding quadratic fits of MoS_2 nanopore area as a function of annealing time at **(a)** 450 and 500°C, **(b)** 600°C, and **(c)** 700°C. Each marker color corresponds to a different pore. **(d)** Arrhenius plot of the linear fitting coefficients in (a-c) as a function of annealing temperature. The exponential coefficient of the fitted Arrhenius equation is proportional to the activation energy of nanopore growth.

6.3 **Conclusions**

In conclusion, the temperature dependence of nanopore growth in monolayer TMD membranes, and their edge reconstruction during vacuum annealing, was investigated in the range of 400°C to 700°C. The pore edges become increasingly faceted with increasing temperature, terminating with hexagonal nanopores at 700°C with alternating Mo-ZZ and Mo-Klein edges. The observed growth rate was used to calculate the activation energy of $E_a = 0.39$ eV for removal of a Mo atom from the edge of MoS_2. The knowledge of the activation

energy of the growth process can be used to determine the appropriate time and temperature to control the pore growth. The use of these findings in the design of nanopores will allow better control of the geometry and chemistry of their edges, and allow for implementation of new nanopore devices with selectable biosensitivity, sieving selectivity, and chemical activity.

Chapter 7: Conclusions and Future Directions

7.1 **Conclusions**

In this thesis, we investigated and developed techniques to controllably process 2D TMDs to enable the synthesis of advanced structures such as heterostructures, heterogeneous alloys, and nanoporous membranes. The applications benefiting from these advances range from electronics and optics in the case of heterostructures and alloys to DNA sequencing and water purification in the case of nanoporous membranes.

This thesis began by demonstrating the rapid pace of advancement in semiconductor technology over the preceding half-century, thus motivating continued research in semiconductor materials discovery and the development of materials processing methods. As an emerging class of semiconducting materials with a variety of novel properties, 2D TMDs have the potential to advance the state-of-the-art for several device applications.

In Chapter 3, a temperature-dependent two-step CVD process was demonstrated wherein the substrate temperature of the second growth step dictated the compositional configuration of the resulting crystal. WS_2 crystal growth at 1,100°C followed by MoS_2 crystal growth at 650°C resulted in an inverted phase-segregated heterostructure consisting of a MoS_2 core and WS_2 outer ring. The same WS_2 crystal growth step followed by MoS_2 crystal growth at ≥680°C resulted in nearly homogeneous alloying to form $Mo_xW_{1-x}S_2$. The phase segregation and alloying was due to thermodynamically-driven in-plane diffusion and demonstrated that the compositional configuration can differ from the growth chronology.

In Chapter 4, this phase segregation and alloying process was investigated further to identify the underlying factors and atomistic mechanisms that govern the diffusion. Experimental and

computational results suggested a defect-driven process related to the presence of sulfur vacancies. This hypothesis was tested by CVD growth of MoS_2 on a substrate containing WS_2 crystals with heterogeneous defect densities. The resulting heterogeneously alloyed $Mo_xW_{1-x}S_2$ crystals possessed Mo concentrations that matched the distribution of point defects in the template WS_2 crystal. This demonstration of translating defects densities into local alloy concentrations has implications in bespoke configurational processing of TMD alloy systems. Additionally, plotting the PL intensity as a function of composition within a heterogeneous alloy demonstrated the exponential relationship between quantum yield and composition, spanning two orders of magnitude and reaching the maximum value for the equicompositional alloy $Mo_{0.5}W_{0.5}S_2$ ($x = 0.5$). These luminescence yield results may lead to enhanced energy efficiency in lighting applications.

In Chapter 5, the relationship between point defects and composition in 2D TMD crystals was applied to the formation of lithographically patterned heterostructures. Building upon Chapters 3 and 4, laser exposure was demonstrated as a method to enable direct-write patterning of thermal defect formation in WS_2 crystals. These patterned defects then served as nucleation points in CVD of MoS_2 for patterned heterostructure synthesis. The process parameters of laser power and wavelength were investigated to identify the relationships and optimal conditions for defect and consequent heterostructure formation.

In Chapter 6, the fundamental concepts of defect formation in 2D TMDs was applied to the formation of nanoporous membranes. With the end goal of controllably processing nanopores to have desirable radii and edge structures, 2D TMDs with artificially created nanopores were subjected to *in situ* annealing in a TEM chamber. The observation of nanopore growth and edge reconstruction behavior was corroborated by analytical and Monte Carlo modeling to reveal the

following relationship between nanopore processing and vacuum annealing temperature: (1) As annealing temperature increases, nanopores become increasingly faceted, favoring the Mo-ZZ and Mo-Klein edge structures and (2) nanopore radius increases linearly with respect to time at an Arrhenius temperature-dependent rate with 0.39 eV activation energy.

Overall, this thesis studies process parameters relevant to fabrication of advanced structures comprised of 2D TMDs. Through the controlled introduction of crystal defects, the composition and structure of these crystals can be modified to produce materials with a variety of desirable properties and capabilities for a wide range of applications.

7.2 **Recent advances and future directions**

The results presented in this thesis consist of small-scale and proof-of-concept demonstrations of physical phenomena. To make a significant impact on the future of the relevant industries, work must be done to further understand these phenomena, broaden their scope, and demonstrate their robustness when applied to mass-production. This final section of the thesis will summarize some recent advances in the field since the work presented in the preceding chapters and provide an outline of potential follow-up experiments.

7.2.1 In situ observation of diffusion

A DFT-calculated proposed reaction path for S vacancy-driven diffusion of Mo in WS_2 is provided Figure 4-3. The general consequences of this model were corroborated indirectly by production of graded $Mo_xW_{1-x}S_2$ crystals in which the defect density of the template WS_2 crystal matched the final Mo distribution. Han *et al.* have demonstrated MoS_2 encroachment into WSe_2, resulting in the formation of 1D nanochannels. Due to the strain from the lattice mismatch, this process has been attributed to the migration of a 5|7 dislocation (Figure 1-3).[184] Susarla *et al.*

have demonstrated phase separation of $Mo_xW_{1-x}S_{2y}Se_{2-2y}$ following vacuum annealing at 250°C. This has been attributed to the presence of a miscibility gap in the material system, though an atomistic mechanism is not provided.[152] Yang *et al.* have demonstrated Re-Mo direct exchange in Re-doped MoS_2, attributed to a recombination-enhanced process triggered via controlled creation of S vacancies.[170] Despite these corroborating examples of nano-scale reconfiguration in 2D TMD crystals, the exact atomistic mechanism remains unproven.

In pure 2D materials, direct atomic-scale imaging has resulted in definitive demonstrations of the atomistic mechanisms of the motion of dislocations, grain boundaries, and vacancies.[68,88,215] Using a windowed gas cell to introduce precursor vapor during *in situ* aberration-corrected STEM, one could observe the deposition and migration of individual transition metal and chalcogen atoms in real time. Using the electron beam to modulate local defect densities through knock-on damage, this technique could demonstrate atomic-scale direct-write patterning while revealing the fundamental atomistic mechanisms of the vacancy-driven diffusion process.

7.2.2 Expanding the TMD library

Chapter 5 demonstrates the formation of MoS_2/WS_2 heterostructures in which the MoS_2 growth recipe is intentionally unfavorable for MoS_2 nucleation. Consequently, MoS_2 growth is limited to the patterned heterostructure formation *via* a defect-assisted growth process. Although MoS_2 and WS_2 are commonly studied and easily synthesized 2D TMDs, many other TMD materials have been predicted to exist, have been isolated by mechanical exfoliation, but have not yet or only recently been synthesized by bottom-up techniques. Broadening our direct-write heterostructure patterning technique to other 2D TMDs, one could use this technique to grow heterostructures in which the patterned material lacks a controllable synthesis method.

Among these more elusive 2D TMDs, 2D TaS_2 is known to exhibit commensurate charge density waves and has only been chemically synthesized as recently as 2016.[216] Meanwhile, metallic NbS_2 has only been synthesized in lateral heterostructures with semiconducting TMDs as recently as 2018.[217] Also in 2018, Zhou *et al.* published a comprehensive library of synthesis routes for 2D TMDs including 32 binary compounds (based on the transition metals Ti, Zr, Hf, V, Nb, Ta, Mo, W, Re, Pt, Pd, and Fe), 13 alloys (including 11 ternary, 1 quaternary, and 1 quinary), and 2 heterostructures by using a NaCl-assisted method similar to the one described in Chapter 4.[105] From the binary compounds alone, our direct-write heterostructure patterning technique could create nearly 500 heterostructures. Including the alloys, that number approaches 1,000. Although many of these proposed heterostructures may not serve a useful function, their synthesis would demonstrate a manufacturing capability sufficient for the formation of a wide array of all-2D devices incorporating conductors, p-type and n-type semiconductors, insulators, magnets, and a variety of new circuit components for photonics, spintronics, excitonics, etc.

7.2.3 Large-scale patterning of heterostructure and alloy devices

Although Chapter 5 demonstrates an arbitrarily tunable patterning technique beyond the growth-defined patterning demonstrated in Chapters 3 and 4, this direct-write laser exposure method is not optimized for scalability. Similar results have been achieved in literature by replacing the laser exposure with electron beam exposure[41] or focused ion beam patterning[218] followed by an etching step. These processes could be replicated in a scalable manner using masked photolithography. However, unlike the laser exposure technique, these processes result in complete removal of the underlying TMD material, thereby eliminating the possibility of vertical heterostructure or alloy formation.

Modern microelectronic chip manufacturing makes use of excimer laser lithography.[219] Therefore, the incorporation of laser exposure patterning into an industrially scalable process is not necessarily unreasonable. However, to optimize resolution, excimer laser lithography uses significantly shorter wavelength and consequently higher energy than the optimized 633 nm laser wavelength demonstrated in Chapter 5. Consequently, optimal exposure parameters would need to be significantly altered (*e.g.*, lower power and shorter exposure duration).

Alternatively, more scalable methods of patterned defect formation could be investigated to supplant the role of direct laser exposure. As an example, lithographically patterned exposure of TMDs to molecules or elements with strong S affinity could strip the S away from the TMDs resulting in the formation of locally S-deficient TMDs. Additionally, optothermoplasmonic nanolithography can be used as a high-resolution method to locally anneal 2D materials to generate patterned point defects, as was demonstrated by Lin *et al.* in 2018.[220] Regardless of the method of choice, the capability of reliable and controllable processing in mass-production on a wafer-scale is essential for this technology to make an impact in the semiconductor manufacturing industry.

7.2.4 Device testing with processed TMD nanopores

Chapter 6 provides a comprehensive analysis of nanopore growth and edge reconstruction within the vacuum of a TEM chamber. While these experimental results are self-consistent and corroborated by modeling, they have not been tested in device applications. To ensure that all relevant parameters have been considered and to translate processing parameters into device performance properties, a study should be conducted to directly map the relation between annealing time and temperature parameters and relevant device parameters such as ionic conductance and blockage change for DNA translocation applications or permeability and salt

rejection for desalination applications. For example, the hydrophilicity of Mo-terminated nanopores produced in the faceted growth regime are expected to yield enhanced ion rejection and water flux, resulting in superior desalination performance relative to isotropic nanopores.

Appendix: MATLAB Functions

Monte Carlo simulation of nanopore growth

```
function [Area, Perimeter, Lattice, HeatMap, AFit,PFit] =
PoreMC(NumIterations, MetalProb, ChalcProb)
%% Monte Carlo simulation of pore growth treating S atoms as
separate entities occupying the same lattice site
%Inputs:
%NumIterations is a guess of the number of iterations used for
initializing the area, perimeter, and heatmap outputs and
determining x-axis scale in video figure.
%MetalProb is a number between 0 and 1 which corresponds to the
probability that any edge metal atom will be ejected
%ChalcProb is same as MetalProb, but for chalcogen atoms

%Example inputs: PoreMC(1000, 0.03, 0.03)

%Outputs:
%Area is a (NumIterations,2) array. First column is iteration
number, second column is number of vacant atomic columns.
%Perimeter is same as Area, but for the number of edge atoms
%Lattice is the final map of where the remaining atoms are
located.
%HeatMap labels which iteration caused each ejection to occur.
%AFit is a quadratic fit of the Area
%PFit is a linear fit of the Perimeter

%% Create Hexagonal Lattice on a Cartesian grid & Initialize
HeatMap
%Armchair direction is x-axis and 60 degree rotations of it
%Zigzag direction is y-axis and 60 degree rotations of it
%Lattice value of 2 if 2 chalcogen atoms present, 1.5 if 1
chalcogen atom present, 1 = metal atom present, 0 = no atom

Lattice = zeros(100,100); %intialize lattice
for i = 1:50 %rows/2
    for j = 1:25 %columns/4
        Lattice(2*i,4*j-1:4*j)=[2,1]; %X = 2, M = 1
        Lattice(2*i-1,4*j-3:4*j-2)=[2,1]; %X = 2, M = 1
    end
end

HeatMap=zeros(100,100); %initialize HeatMap
for i = 1:100
    for j = 1:100
```

```
        if Lattice(i,j)>0
            HeatMap(i,j)=-1; %if Heatmap(i,j) is never modified
later in the code, we know this atom survives until the end of
the simulation
        else
            HeatMap(i,j)=NaN; %empty index (not part of lattice)
        end
    end
end

%% Begin Measuring Lattice Properties and Initialize Pore
(Vacancy)
TotalAtoms = zeros(NumIterations,1); %initialize count of total
atoms (note: propto area)
TotalEdgeAtoms = zeros(NumIterations,1); %initialize count of
edge atoms (note: propto perimeter)
Area = zeros(NumIterations,2); %initialize area
Perimeter = zeros(NumIterations,2);

i=1; %iteration number
Lattice(50,51)=0; %initialize pore near middle
HeatMap(50,51)=i; %position 50, 51 removed after first iteration

TotalAtoms(1,1) = sum(sum(Lattice~=0)); %store atom count at t=0
--> pore = single atom vacancy
Area(i,1)=i; %iteration number
Area(i,2)=TotalAtoms(1)+1-TotalAtoms(i); %area after ith
iteration

TotalEdgeAtoms(1,1) = sum(sum(isEdgeAtom(Lattice)~=0)); %store
edge atom count at t=0 --> pore = single atom vacancy
Perimeter(i,1)=i; %iteration number
Perimeter(i,2)=TotalEdgeAtoms(i); %perimeter after ith iteration

%% MP4 Video Formatting (un-comment commented lines in this
section to write to mp4 file)
if MetalProb<.099
    Percent = ['0',num2str(100.*MetalProb)];
else
    Percent = num2str(100.*MetalProb);
end
cm = [0, 0, 0; 0, 0, 0; 84, 181, 182; 255, 200, 50; 255, 255,
0]; % Color Map for values 0, 0.5, 1, 1.5, 2 corresponding to
"empty", null, metal, 1chalc, 2chalc
cm = cm./255; %convert to decimal
% v=VideoWriter(['PoreGrowth_p', num2str(Percent),'.mp4'],
'MPEG-4'); %initialize video writer
```

```
% v.Quality = 100; %set quality to max
% v.FrameRate = 2; % adjust based on total number of frames and
desired runtime
% open(v) %open video writer

fig = figure; %open figure
subplot(1,2,1) %left subplot
P = imagesc(Lattice); %heat map
Text = text(50,105,['P = ', Percent,
'%'],'FontSize',14,'HorizontalAlignment', 'center');
colormap(cm); %use colormap cm defined above
caxis([0 2]); %set color axis
colorbar off %remove colorbar
pbaspect([1 1 1]) %set 1:1 aspect ratio
set(gca,'nextplot','replacechildren','visible','off') %turn off
axes
subplot(1,2,2) %right plot
plot(Area(i,1),sqrt(Area(i,2)./pi),'k.');
pbaspect([1 1 1]) %set 1:1 aspect ratio
xlabel('Iterations') %label x axis
xlim([0 NumIterations]) %number of iterations
ylabel('Radius');
ylim([0 25]);
% f = getframe(fig); %get frame
% writeVideo(v,f.cdata); %add frame data to video
i = i+1;

%% Iterate Pore Growth and Store Lattice Properties at Each Step
while TotalAtoms(1)+1-TotalAtoms(i-1)<1500 %pore occupies 30% of
atomic sites
    [Lattice, HeatMap] = MonteCarloPoreGrowth(i, Lattice,
HeatMap, MetalProb, ChalcProb); %Pore growth happens here. New
Lattice and HeatMap replace old ones.
    TotalAtoms(i,1)=sum(sum(Lattice~=0)); %add new atom count
data point to the list
    TotalEdgeAtoms(i,1) = sum(sum(isEdgeAtom(Lattice)~=0)); %add
new edge atom count data point to the list

    Area(i,1)=i; %same area and perimeter steps as above in
Begin Measuring Lattice Properties and Initialize Pore (Vacancy)
section
    Area(i,2)=TotalAtoms(1)+1-TotalAtoms(i);
    Perimeter(i,1)=i;
    Perimeter(i,2)=TotalEdgeAtoms(i);

    subplot(1,2,1) %same plotting steps as above in MP4 Video
Formatting section
```

```
    P = imagesc(Lattice);
    Text = text(50,105,['P = ', Percent, '%'], 'FontSize',14,
'HorizontalAlignment', 'center');
    colormap(cm);
    caxis([0 2]);
    colorbar off
    pbaspect([1 1 1])
    set(gca, 'visible', 'off');
    subplot(1,2,2)
    plot(Area(1:i,1),sqrt(Area(1:i,2)./pi),'k.');
    pbaspect([1 1 1])
    xlabel('Iterations')
    xlim([0 NumIterations])
    ylabel('Radius');
    ylim([0 25]);
    % f= getframe(fig); %un-comment to write to mp4
    % writeVideo(v,f.cdata); %un-comment to write to mp4

    i=i+1; %increase iteration counter
end
% close(v) %un-comment to write to mp4

%% Clean up
HeatMap(HeatMap == -1) = NaN; %any atoms that survive until the
end of the simulation should still have values of -1. To
visualize the pore better, we can remove them now
Area = Area(1:max(Area(:,1)),:); %remove any extra 0's at the
end if NumIterations overestimated
Perimeter = Perimeter(1:max(Perimeter(:,1)),:); %remove any
extra 0's at the end if NumIterations overestimated

%% Fit Area and Perimeter Outputs
if ~isempty(Area(Area(:,2)>50,1)) %if Area is ever bigger than
50 (there tends to be a lot of statistical noise below 50 and
fitting is improved if we ignore that)
    AFit=fit(Area(Area(:,2)>50,1),Area(Area(:,2)>50,2),'poly2');
%only use data from Area > 50 to do a quadratic fit

PFit=fit(Perimeter(Area(:,2)>50,1),Perimeter(Area(:,2)>50,2),'po
ly1'); %only use data from Area > 50 to do a linear fit
else
    AFit.p1=0;
    PFit.p1=0;
end
end
```

```
%% isEdgeAtom Function
%Edge of the pore
function Map = isEdgeAtom(Lattice) %0 if not EdgeAtom, 1 if two-
neighbor edge atom, 2 if one-neighbor edge atom, 3 if zero-
neighbor edge atom
[row, col] = size(Lattice);
Map = zeros(row,col); %initialize output Boolean map

for i = 2:row-1 %ignore perimeter row and col of Lattice because
they of course won't be saturated
    for j = 2:col-1
        if Lattice(i,j)>0 && sum(sum(Lattice(i-1:i+1,j-
1:j+1)~=0))==3 %if there is an atom there and it has two nearest
neighbors
            Map(i,j)=1; %if two-neighbor edge atom (missing 1
neighbor)
        elseif Lattice(i,j)>0 && sum(sum(Lattice(i-1:i+1,j-
1:j+1)~=0))==2 %if there is an atom there and it has one nearest
neighbor
            Map(i,j)=2; %if one-neighbor edge atom (missing 2
neighbors)
        elseif Lattice(i,j)>0 && sum(sum(Lattice(i-1:i+1,j-
1:j+1)~=0))==1 %if there is an atom there and it has zero
nearest neighbors
            Map(i,j)=3; %if zero-neighbor edge atom (missing 3
neighbors)
        end
    end
end
end

%% MonteCarloPoreGrowth Function
function [Lattice, HeatMap] = MonteCarloPoreGrowth(
IterationNumber, Lattice, HeatMap, MetalProb, ChalcProb)
[row, col] = size(Lattice); %generalize function by determining
size of input lattice
EdgeLattice = isEdgeAtom(Lattice); %1 if 2-neighbor edge atom. 2
if 1-neighbor edge atom. 3 if 0-neighbor edge atom. 0 if not an
edge atom

for i = 2:row-1
    for j = 2:col-1
        r1 = rand(1);
        r2 = rand(1);

        %Island
```

```
        %Not perfect -- only applies if it is a single-atom
island and not if there is a floating cluster
        %Could be improved with a simple message passing
algorithm, but may significantly slow down the code
        if EdgeLattice(i,j)==3
            Lattice(i,j)=0; %disconnected floating atoms are
always displaced (100% probability)
            HeatMap(i,j)=IterationNumber; %site becomes vacancy
on iteration number i

        %Edge atom
        elseif EdgeLattice(i,j)==1 || EdgeLattice(i,j)==2

            %Metal
            if Lattice(i,j)==1
                if r1 < MetalProb
                    Lattice(i,j)=0;
                    HeatMap(i,j)=IterationNumber;
                end

            %Dichalcogen
            elseif Lattice(i,j)==2
                if (r1 < ChalcProb || r2 < ChalcProb) %if at
least one of the atoms is removed
                    Lattice(i,j)=1.5;
                    if (r1 < ChalcProb && r2 < ChalcProb) %if
both atoms are removed
                        Lattice(i,j)=0;
                        HeatMap(i,j)=IterationNumber; %only add
iteration number to this index of the HeatMap once atomic column
is fully vacant
                    end
                end

            %Monochalcogen
            elseif Lattice(i,j)==1.5
                if r1 < ChalcProb
                    Lattice(i,j)=0;
                    HeatMap(i,j)=IterationNumber;
                end
            end
        end
    end
end
end
```

Graphical user interface (GUI) for processing hyperspectral data (*e.g.*, Raman, PL)

```
function ISNRamanGUI(inputTXT)
%input a .txt file from a hyperspectral Raman Map collected on
the MIT ISN Horiba Jobin Yvon HR800 Example input:
%ISNRamanGUI('Raman Map.txt')
FID = fopen(inputTXT); %open txt file
line = fgetl(FID); %grab first line
fclose(FID); %close txt file
if strcmp(line(1:3),'Acq')==1 %if there is a header (first line
is "Acq. time (s)")...
    %...ignore header and read tab delimited text starting at 34
lines later
    Raw = dlmread(inputTXT,'\t',34, 0);
else %if no header...
    Raw = dlmread(inputTXT,'\t'); %read tab delimited text
end

Spectrum = Raw(1,3:end); %Spectrum
[Rows, Columns] = size(Raw); %size of 2D matrix

%% Determine Pixels Dimensions
yVal = Raw(2,1);
xVal = Raw(2,2);
for i = 3:Rows
    yValCounter = 0;
    for j = 1:length(yVal)
        if abs(Raw(i,1)-yVal(j))>.01 %if Raw(i,1) contains a
never-before-seen y Value
            yValCounter = yValCounter+1; %increase counter
        end
    end
    if yValCounter == length(yVal) %if counter was increased
        yVal = [yVal,Raw(i,1)]; %add new y Value to variable
yVal
    end

    %do same thing for xVal as was done above for yVal
    xValCounter = 0;
    for j = 1:length(xVal)
        if abs(Raw(i,2)-xVal(j))>.01
            xValCounter = xValCounter+1;
        end
    end
    if xValCounter == length(xVal)
        xVal = [xVal,Raw(i,2)];
    end
```

```
end

%% Convert 2D Matrix into 3D Matrix
%Initialize 3D Matrix yPixels become columns. xPixels become
rows. Columns
%from TwoMatrix is number of wavenumbers + 2 because it includes
the
%coordinate data in the first two columns
ThreeMatrix = zeros(length(yVal), length(xVal), Columns-2);
for i = 1:length(yVal)
    for j = 1:length(xVal)
        for k = 1:Columns-2
            %Convert 2D Matrix to 3D Matrix (xPixels x yPixels x
total wavenumbers)
            ThreeMatrix(i,j,k)=Raw(1+j+(length(xVal)*(i-1)),
k+2);
        end
        ThreeMatrix(i,j,:)=medfilt1(ThreeMatrix(i,j,:));
    end
end

%% Remove all data below 70 cm-1 because the zero loss filter
clips this data anyway
Spectrum = Spectrum(Spectrum>70);
ThreeMatrix = ThreeMatrix(:,:,end-length(Spectrum)+1:end);

%% Create Figure
f = figure;

% Initialize Data
current_data_SPECTRUM =
permute(ThreeMatrix(round(length(yVal)./2),round(length(xVal)./2
),:),[3 1 2]);

% Left Plot: Map at a wave number / range
subplot(1,2,1)
[~,ind] = min(abs(Spectrum-380)); %Default map shows intensity
at 380cm-1
current_data_MAP = ThreeMatrix(:,:,ind);
MAP = imagesc(current_data_MAP,'ButtonDownFcn',
@MAP_ButtonDownFcn);
set(gca,'nextplot','replacechildren')
pbaspect([length(xVal), length(yVal), 1])
clbr=colorbar;
title(clbr,'Intensity at 380 cm-1','FontSize',12);

%Right Plot: Spectrum at a pixel
```

```
subplot(1,2,2)
SPECTRUM =
plot(Spectrum(1,:)',current_data_SPECTRUM,'ButtonDownFcn',
@SPECTRUM_ButtonDownFcn); %Default spectrum is from center pixel
pbaspect([1 1 1])
set(gca,'nextplot','replacechildren');
xlabel('Wave Number (cm-1)','FontSize',12);
ylabel('Intensity (a.u.)','FontSize',12);
title(['Spectrum at (', num2str(round(length(xVal)./2)), ',',
num2str(round(length(yVal)./2)), ')'],'FontSize',12);
xlim([min(Spectrum) max(Spectrum)]);

%Find max intensity for fixed axes in right plot
OneMatrix = sort(reshape(ThreeMatrix(:,:,:),[],1));
SpecMax = 0;
SpecMaxInd = length(OneMatrix);
while SpecMax ==0
    %the "*1.1" is to avoid getting a random cosmic ray spike as
the max value
    if OneMatrix(SpecMaxInd) < (OneMatrix(SpecMaxInd-1)*1.1)
        SpecMax = OneMatrix(SpecMaxInd);
    else
        SpecMaxInd = SpecMaxInd-1;
    end
end
ylim([0 1.05.*SpecMax]);

%Background Subtraction
uicontrol('Style','PushButton','String','Background
Subtract','Position',[20,20,120,20],'CallBack',
@BS_ButtonDownFcn);

%Slider for tunable spectral range
SliderPosition = 0;
uicontrol('Style','Slider','String','Spectral Integral
Width','Position',[20,60,120,20],'Min',0,'Max',20,'CallBack',
@SliderFcn);
txt = uicontrol('Style','text','Position',[20 85 150
20],'String',['Spectral Integration Width: ',
num2str(SliderPosition)]);
f.Name = 'ISN Raman GUI'; % Assign a name to appear in the
window title.
movegui(f,'center') % Move the window to the center of the
screen.
f.Visible = 'on'; % Make the window visible.

%Button for Map Grab
```

```
uicontrol('Style','PushButton','String','Save Map To
File','Position',[160,20,120,20],'CallBack', @MapGrabFcn);

%Button for Spectrum Grab
uicontrol('Style','PushButton','String','Save Spectrum To
File','Position',[440,20,120,20],'CallBack', @SpectrumGrabFcn);

%Button for Plotting Ratios
uicontrol('Style','PushButton','String','Plot
Ratios','Position',[300,20,120,20],'CallBack', @RatioMapFcn);

%Button for Plotting Differences
uicontrol('Style','PushButton','String','Plot
Differences','Position',[300,60,120,20],'CallBack',
@DiffMapFcn);

%Popup Menu for Switching Between Intensity and Position Mapping
uicontrol('Style', 'popup', 'String', {'Intensity', 'Position'},
'Position', [160, 60, 120, 20], 'CallBack', @PopupFcn);
PopupSetting = 'Intensity';

%% ButtonDownFcn Callbacks
  function MAP_ButtonDownFcn(source, eventdata) %if map pixel is
clicked on in left plot
      xPix = round(eventdata.IntersectionPoint(1));
      yPix = round(eventdata.IntersectionPoint(2));
      current_data_SPECTRUM =
permute(ThreeMatrix(yPix,xPix,:),[3 1 2]); %...update spectrum
in right plot
      subplot(1,2,2)
      SPECTRUM =
plot(Spectrum(1,:)',current_data_SPECTRUM,'ButtonDownFcn',
@SPECTRUM_ButtonDownFcn);
      title(['Spectrum at (',num2str(xPix), ',', num2str(yPix),
')'],'FontSize',12);
  end

  function SPECTRUM_ButtonDownFcn(source,eventdata) %if spectrum
value is clicked on in right plot
      WaveNumber = round(eventdata.IntersectionPoint(1));
      Spec = source.XData;
      [~,indLow] = min(abs(Spec-(WaveNumber-
(SliderPosition./2))));
      [~,indHigh] = min(abs(Spec-
(WaveNumber+(SliderPosition./2))));

      %Intensity Mapping
```

```
      if strcmp(PopupSetting,'Intensity')
        current_data_MAP =
sum(ThreeMatrix(:,:,indLow:indHigh),3)./(indHigh-indLow+1);
        subplot(1,2,1)
        MAP = imagesc(current_data_MAP,'ButtonDownFcn',
@MAP_ButtonDownFcn); %update map in left plot
        caxis('auto')
        if indLow == indHigh %if slider set to 0
          title(clbr,['Intensity at ',
num2str(round(WaveNumber)) , ' cm-1'],'FontSize',12);
        else %if slider not set to 0
          title(clbr,['Avg. Intensity from ',
num2str(round(WaveNumber-(SliderPosition./2))), ' to ',
num2str(round(WaveNumber+(SliderPosition./2))), ' cm-
1'],'FontSize',12);
        end

      %Position Mapping
      elseif strcmp(PopupSetting,'Position')
          if indHigh-indLow>0
            [~,PositionIndices] =
max(ThreeMatrix(:,:,indLow:indHigh),[],3);
            for x = 1:length(xVal)
                for y = 1:length(yVal)
                    current_data_MAP(y,x) =
Spec(indLow+PositionIndices(y,x));
                end
            end
            subplot(1,2,1)
            MAP = imagesc(current_data_MAP,'ButtonDownFcn',
@MAP_ButtonDownFcn); %update map in left plot
            caxis([round(WaveNumber-(SliderPosition./2)),
round(WaveNumber+(SliderPosition./2))]);
            title(clbr,['Peak Position from ',
num2str(round(WaveNumber-(SliderPosition./2))), ' to ',
num2str(round(WaveNumber+(SliderPosition./2))), ' cm-
1'],'FontSize',12);
          end
      end
  end

    function BS_ButtonDownFcn(source, eventdata) %background
subtraction
        [a,b,c] = size(ThreeMatrix);
        newThreeMatrix = zeros(a,b,c);
        for x = 1:length(xVal) %iterate through every pixel
            for y = 1:length(yVal)
```

```
                %Perform Convex Hull Method
                ConvexTemp =
convhull(Spectrum,permute(ThreeMatrix(y,x,:),[3 1 2])');
                Convex = ConvexTemp(1);
                for i = 2:length(ConvexTemp)
                    if ConvexTemp(i)>ConvexTemp(i-1)
                        Convex(i)=ConvexTemp(i);
                    end
                end


                ConvexPoint = false;
                for i = 1:length(Spectrum)
                    if ismember(i,Convex) %if this spectral
value is part of the convex hull
                        newThreeMatrix(y,x,i)=0;
                        ConvexPoint = true;
                    elseif ConvexPoint == true %if last spectral
value was part of the convex hull
                        PrevHullSpectrum = Spectrum(i-1);
%spectral value at previous convex hull point
                        [~, PrevHullIndex] = min(abs(i-1-
Convex));
                        NextHullIndex = PrevHullIndex+1;
                        NextHullSpectrum =
Spectrum(Convex(NextHullIndex)); %spectral value at next convex
hull point
                        PrevHullValue = ThreeMatrix(y,x,i-
1);%intensity value at previous convex hull point
                        NextHullValue =
ThreeMatrix(y,x,Convex(NextHullIndex));%intensity value at next
convex hull point
                        Slope = (NextHullValue-
PrevHullValue)./(NextHullSpectrum-PrevHullSpectrum);
                        InterpVal = PrevHullValue +
Slope*(Spectrum(i)-PrevHullSpectrum); %interpolated value from
slope

newThreeMatrix(y,x,i)=ThreeMatrix(y,x,i)-InterpVal;
                        ConvexPoint = false; %set back to false
                    else %can re-use slope the "elseif" above
                        InterpVal = PrevHullValue +
Slope*(Spectrum(i)-PrevHullSpectrum); %interpolated value from
slope

newThreeMatrix(y,x,i)=ThreeMatrix(y,x,i)-InterpVal;
```

```
                    end
                end
            end
        end
        ThreeMatrix=newThreeMatrix;
        OneMatrix = sort(reshape(ThreeMatrix(:,:,:),[],1));
        SpecMax = OneMatrix(SpecMaxInd);
        subplot(1,2,2)
        ylim([0 1.05.*SpecMax]);
    end

    function SliderFcn(source, eventdata) %if slider position
changes
        SliderPosition = round(eventdata.Source.Value);
        txt = uicontrol('Style','text','Position',[20 85 150
20],'String',['Spectral Integration Width: ',
num2str(SliderPosition)]);
    end

    function MapGrabFcn(source, eventdata)
        MapGrab = current_data_MAP; %grabs current map
        varName = ['''',input('Please name this array:
','s'),'.mat''']; %asks user for variable name
        save(varName(2:end-1), 'MapGrab'); %saves map as a .mat
file using variable name. e.g., 'A Peak.mat'
    end

    function RatioMapFcn(source, eventdata)
        NumeratorName = ['''',input('Numerator file name:
','s'),'.mat''']; %asks user for numerator file name
        Numerator = load(NumeratorName(2:end-1));
        DenominatorName = ['''',input('Denominator file name:
','s'),'.mat''']; %asks user for denominator file name
        Denominator = load(DenominatorName(2:end-1));
        [NumeratorRows, NumeratorCols] =
size(Numerator.MapGrab);
        maxNumerator = max(max(Numerator.MapGrab));
        for i = 1:NumeratorRows
            for j = 1:NumeratorCols
                if Numerator.MapGrab(i,j)< 0.15*maxNumerator
                    Numerator.MapGrab(i,j)=0;
                end
            end
        end
        Ratio = (Numerator.MapGrab) ./ (Denominator.MapGrab);
%Divide to calculate ratio
```

```
        RatioFig = figure;
        RatioPlot = imagesc(Ratio); %plot in new figure
        colorbar
        RatioFig.Name = 'Intensity Ratios'; % Assign a name to
appear in the window title.
        pbaspect([NumeratorCols, NumeratorRows, 1])
    end

    function DiffMapFcn(source,eventdata)
        FirstName = ['''',input('First file name:
','s'),'.mat''']; %asks user for first file name
        First = load(FirstName(2:end-1));
        SecondName = ['''',input('Second file name:
','s'),'.mat''']; %asks user for second file name
        Second = load(SecondName(2:end-1));
        [FirstRows, FirstCols] = size(First.MapGrab);
        Difference = (First.MapGrab) - (Second.MapGrab); %First
minus second

        DiffFig = figure;
        DiffPlot = imagesc(Difference); %plot in new figure
        colorbar
        DiffFig.Name = 'Peak Position Difference'; % Assign a
name to appear in the window title.
        pbaspect([FirstCols, FirstRows, 1])
    end

    function PopupFcn(source, eventdata)
        PopupSettingNumber = eventdata.Source.Value;
        PopupSetting =
eventdata.Source.String{PopupSettingNumber};
    end

    function SpectrumGrabFcn(source,eventdata)
        SpectrumGrab(:,1) = Spectrum;
        SpectrumGrab(:,2) = current_data_SPECTRUM; %grabs
current map
        varName = ['''',input('Please name this data:
','s'),'.mat''']; %asks user for variable name
        save(varName(2:end-1), 'SpectrumGrab'); %saves map as a
.mat file using variable name. e.g., 'A Peak.mat'
    end
end
```

Bibliography

(1) https://www.nobelprize.org/prizes/physics/1956/summary/.

(2) Moore, G. E. *Electronics* **1965**, *38*, 114–117.

(3) https://www.nrel.gov/pv/cell-efficiency.html.

(4) *III-Nitride Based Light Emitting Diodes and Applications*, 2nd ed.; Seong, T.-Y., Han, J., Amano, H., Morkoç, H., Eds.; Springer, 2017.

(5) Shulaker, M. M.; Hills, G.; Patil, N.; Wei, H.; Chen, H. Y.; Wong, H. S. P.; Mitra, S. *Nature* **2013**, *501* (7468), 526–530.

(6) Dubey, A.; Adhikari, N.; Mabrouk, S.; Wu, F.; Chen, K.; Yang, S.; Qiao, Q. *J. Mater. Chem. A* **2018**, *6* (6), 2406–2431.

(7) Bhimanapati, G. R.; Lin, Z.; Meunier, V.; Jung, Y.; Cha, J. J.; Das, S.; Xiao, D.; Son, Y.; Strano, M. S.; Cooper, V. R.; Liang, L.; Louie, S. G.; Ringe, E.; Zhou, W.; Sumpter, B. G.; Terrones, H.; Xia, F.; Wang, Y.; Zhu, J.; Akinwande, D.; Alem, N.; Schuller, J. A.; Schaak, R. E.; Terrones, M.; Robinson, J. A. *ACS Nano* **2015**, *9* (12), 11509–11539.

(8) Lin, Z.; McCreary, A.; Briggs, N.; Subramanian, S.; Zhang, K.; Sun, Y.; Li, X.; Borys, N. J.; Yuan, H.; Fullerton-Shirey, S. K.; Chernikov, A.; Zhao, H.; McDonnell, S.; Lindenberg, A. M.; Xiao, K.; LeRoy, B. J.; Drndić, M.; Hwang, J. C. M.; Park, J.; Chhowalla, M.; Schaak, R. E.; Javey, A.; Hersam, M. C.; Robinson, J.; Terrones, M. *2D Mater.* **2016**, *3* (4), 042001.

(9) Dickinson, R. G.; Pauling, L. *J. Am. Chem. Soc.* **1923**, *45* (6), 1466–1471.

(10) Spalvins, T. *ASLE Trans.* **1971**, *14* (4), 267–274.

(11) Lee, W. Y.; Besmann, T. M.; Stott, M. W. *J. Mater. Res.* **1994**, *9* (6), 1474–1483.

(12) Novoselov, K. S.; Geim, A. K.; Morozov, S. V; Jiang, D.; Zhang, Y.; Dubonos, S. V; Grigorieva, I. V; Firsov, A. A. *Science.* **2004**, *306* (5696), 666–669.

(13) https://www.nobelprize.org/prizes/physics/2010/summary/.

(14) Lee, C.; Yan, H.; Brus, L. E.; Heinz, T. F.; Hone, J.; Ryu, S. *ACS Nano* **2010**, *4* (5), 2695–2700.

(15) Splendiani, A.; Sun, L.; Zhang, Y.; Li, T.; Kim, J.; Chim, C. Y.; Galli, G.; Wang, F. *Nano Lett.* **2010**, *10* (4), 1271–1275.

(16) Mak, K. F.; Lee, C.; Hone, J.; Shan, J.; Heinz, T. F. *Phys. Rev. Lett.* **2010**, *105* (13), 136805.

(17) Radisavljevic, B.; Radenovic, A.; Brivio, J.; Giacometti, V.; Kis, A. *Nat. Nanotechnol.* **2011**, *6* (3), 147–150.

(18) Newaz, A. K. M.; Burger, A.; Caudel, D.; Ivanov, B. L.; Mandrus, D. G.; Tolk, N. H.;

Bolotin, K. I.; Ghimire, N. J.; Prasai, D.; Klots, A. R.; Pantelides, S. T.; Yan, J.; Velizhanin, K. A.; Lin, J.; Wang, B.; Krzyzanowska, H. *Sci. Rep.* **2014**, *4*, 6608.

(19) Chernikov, A.; Berkelbach, T. C.; Hill, H. M.; Rigosi, A.; Li, Y.; Aslan, O. B.; Reichman, D. R.; Hybertsen, M. S.; Heinz, T. F. *Phys. Rev. Lett.* **2014**, *113* (7), 076802.

(20) Ugeda, M. M.; Bradley, A. J.; Shi, S. F.; Da Jornada, F. H.; Zhang, Y.; Qiu, D. Y.; Ruan, W.; Mo, S. K.; Hussain, Z.; Shen, Z. X.; Wang, F.; Louie, S. G.; Crommie, M. F. *Nat. Mater.* **2014**, *13* (12), 1091–1095.

(21) Onga, M.; Zhang, Y.; Ideue, T.; Iwasa, Y. *Nat. Mater.* **2017**, *16*, 1193–1197.

(22) Grosso, G.; Graves, J.; Hammack, A. T.; High, A. A.; Butov, L. V.; Hanson, M.; Gossard, A. C. *Nat. Photonics* **2009**, *3* (10), 577–580.

(23) Xia, F.; Wang, H.; Xiao, D.; Dubey, M.; Ramasubramaniam, A. *Nat. Photonics* **2014**, *8* (12), 899–907.

(24) Gong, Y.; Lin, J.; Wang, X.; Shi, G.; Lei, S.; Lin, Z.; Zou, X.; Ye, G.; Vajtai, R.; Yakobson, B. I.; Terrones, H.; Terrones, M.; Tay, B. K.; Lou, J.; Pantelides, S. T.; Liu, Z.; Zhou, W.; Ajayan, P. M. *Nat. Mater.* **2014**, *13* (12), 1135–1142.

(25) Susarla, S.; Kutana, A.; Hachtel, J. A.; Kochat, V.; Apte, A.; Vajtai, R.; Idrobo, J. C.; Yakobson, B. I.; Tiwary, C. S.; Ajayan, P. M. *Adv. Mater.* **2017**, 29, *1702457*.

(26) Yun, W. S.; Han, S. W.; Hong, S. C.; Kim, I. G.; Lee, J. D. *Phys. Rev. B* **2012**, *85* (3), 033305.

(27) Duan, X.; Wang, C.; Shaw, J. C.; Cheng, R.; Chen, Y.; Li, H.; Wu, X.; Tang, Y.; Zhang, Q.; Pan, A.; Jiang, J.; Yu, R.; Huang, Y.; Duan, X. *Nat. Nanotechnol.* **2014**, *9*, 1024–1030.

(28) Li, M.-Y.; Shi, Y.; Cheng, C.-C.; Lu, L.-S.; Lin, Y.-C.; Tang, H.-L.; Tsai, M.-L.; Chu, C.-W.; Wei, K.-H.; He, J.-H.; Chang, W.-H.; Suenaga, K.; Li, L.-J. *Science.* **2015**, *349* (6247), 524–528.

(29) Huang, C.; Wu, S.; Sanchez, A. M.; Peters, J. J. P.; Beanland, R.; Ross, J. S.; Rivera, P.; Yao, W.; Cobden, D. H.; Xu, X. *Nat. Mater.* **2014**, *13*, 1096–1101.

(30) Gong, Y.; Lei, S.; Ye, G.; Li, B.; He, Y.; Keyshar, K.; Zhang, X.; Wang, Q.; Lou, J.; Liu, Z.; Vajtai, R.; Zhou, W.; Ajayan, P. M. *Nano Lett.* **2015**, *15* (9), 6135–6141.

(31) Zhang, X.; Lin, C.; Tseng, Y.; Huang, K.; Lee, Y.; Nmr, H. *Nano Lett.* **2015**, *15*, 410–415.

(32) Heo, H.; Sung, J. H.; Jin, G.; Ahn, J.-H.; Kim, K.; Lee, M.-J.; Cha, S.; Choi, H.; Jo, M.-H. *Adv. Mater.* **2015**, *27*, 3803–3810.

(33) Kang, J.; Tongay, S.; Zhou, J.; Li, J.; Wu, J. *Appl. Phys. Lett.* **2013**, *102* (2013).

(34) Kobayashi, Y.; Mori, S.; Maniwa, Y.; Miyata, Y. *Nano Res.* **2015**, *8* (10), 3261–3271.

(35) Lin, Z.; Thee, M. T.; Elías, A. L.; Feng, S.; Zhou, C.; Fujisawa, K.; Perea-López, N.; Carozo, V.; Terrones, H.; Terrones, M. *APL Mater.* **2014**, *2* (9), 092514.

(36) Zheng, S.; Sun, L.; Yin, T.; Dubrovkin, A. M.; Liu, F.; Liu, Z.; Shen, Z. X.; Fan, H. J.

Appl. Phys. Lett. **2015**, *106* (6), 063113.

(37) Chen, K.; Wan, X.; Xie, W.; Wen, J.; Kang, Z.; Zeng, X.; Chen, H.; Xu, J. *Adv. Mater.* **2015**, *27* (41), 6431–6437.

(38) Chiu, K. C.; Huang, K. H.; Chen, C. A.; Lai, Y. Y.; Zhang, X. Q.; Lin, E. C.; Chuang, M. H.; Wu, J. M.; Lee, Y. H. *Adv. Mater.* **2018**, 30, *1704796*.

(39) Chen, K.; Wan, X.; Wen, J.; Xie, W.; Kang, Z.; Zeng, X.; Chen, H.; Xu, J.-B. *ACS Nano* **2015**, *9* (10), 9868–9876.

(40) Guimaraes, M. H. D.; Gao, H.; Han, Y.; Kang, K.; Xie, S.; Kim, C. *ACS Nano* **2016**, *10* (6), 6392–6399.

(41) Ling, X.; Lin, Y.; Ma, Q.; Wang, Z.; Song, Y.; Yu, L.; Huang, S.; Fang, W.; Zhang, X.; Hsu, A. L.; Bie, Y.; Lee, Y.-H.; Zhu, Y.; Wu, L.; Li, J.; Jarillo-Herrero, P.; Dresselhaus, M. S.; Palacios, T.; Kong, J. *Adv. Mater.* **2015**, *28* (12), 2322–2329.

(42) Mahjouri-Samani, M.; Lin, M.-W.; Wang, K.; Lupini, A. R.; Lee, J.; Basile, L.; Boulesbaa, A.; Rouleau, C. M.; Puretzky, A. A.; Ivanov, I. N.; Xiao, K.; Yoon, M.; Geohegan, D. B. *Nat. Commun.* **2015**, *6*, 7749.

(43) Chen, X.; Park, Y. J.; Das, T.; Jang, H.; Lee, J. B.; Ahn, J. H. *Nanoscale* **2016**, *8* (33), 15181–15188.

(44) Godin, K.; Kang, K.; Fu, S.; Yang, E.-H. *J. Phys. D. Appl. Phys.* **2016**, *49* (32), 325304.

(45) Bersch, B. M.; Eichfeld, S. M.; Lin, Y. C.; Zhang, K.; Bhimanapati, G. R.; Piasecki, A. F.; Labella, M.; Robinson, J. A. *2D Mater.* **2017**, *4*, 025083.

(46) Han, G. H.; Kybert, N. J.; Naylor, C. H.; Lee, B. S.; Ping, J.; Park, J. H.; Kang, J.; Lee, S. Y.; Lee, Y. H.; Agarwal, R.; Johnson, A. T. C. *Nat. Commun.* **2015**, *6*, 6128.

(47) Sun, D.; Nguyen, A. E.; Barroso, D.; Zhang, X.; Preciado, E.; Bobek, S.; Klee, V.; Mann, J.; Bartels, L. *2D Mater.* **2015**, *2* (4), 45014.

(48) Chen, F.; Wang, L.; Ji, X.; Zhang, Q. *ACS Appl. Mater. Interfaces* **2017**, *9* (36), 30821–30831.

(49) Li, H.; Zhang, Q.; Duan, X.; Wu, X.; Fan, X.; Zhu, X.; Zhuang, X.; Hu, W.; Zhou, H.; Pan, A.; Duan, X. *J. Am. Chem. Soc.* **2015**, *137* (16), 5284–5287.

(50) Mann, J.; Ma, Q.; Odenthal, P. M.; Isarraraz, M.; Le, D.; Preciado, E.; Barroso, D.; Yamaguchi, K.; Von Son Palacio, G.; Nguyen, A.; Tran, T.; Wurch, M.; Nguyen, A.; Klee, V.; Bobek, S.; Sun, D.; Heinz, T. F.; Rahman, T. S.; Kawakami, R.; Bartels, L. *Adv. Mater.* **2014**, *26*, 1399–1404.

(51) Wu, X.; Li, H.; Liu, H.; Zhuang, X.; Wang, X.; Fan, X.; Duan, X.; Zhu, X.; Zhang, Q.; Meixner, A. J.; Duan, X.; Pan, A. *Nanoscale* **2017**, *9* (14), 4707–4712.

(52) Chen, Y.; Dumcenco, D. O.; Zhu, Y.; Zhang, X.; Mao, N.; Feng, Q.; Zhang, M.; Zhang, J.; Tan, P.-H.; Huang, Y.-S.; Xie, L. *Nanoscale* **2014**, *6* (5), 2833–2839.

(53) Chen, Y.; Xi, J.; Dumcenco, D. O.; Liu, Z.; Suenaga, K.; Wang, D.; Shuai, Z.; Huang, Y.-

S.; Xie, L. *ACS Nano* **2013**, *7* (5), 4610–4616.

(54) Feng, Q.; Zhu, Y.; Hong, J.; Zhang, M.; Duan, W.; Mao, N.; Wu, J.; Xu, H.; Dong, F.; Lin, F.; Jin, C.; Wang, C.; Zhang, J.; Xie, L. *Adv. Mater.* **2014**, *26* (17), 2648–2653.

(55) Fu, Q.; Yang, L.; Wang, W.; Han, A.; Huang, J.; Du, P.; Fan, Z.; Zhang, J.; Xiang, B. *Adv. Mater.* **2015**, *27* (32), 4732–4738.

(56) Huang, J.; Wang, W.; Fu, Q.; Yang, L.; Zhang, K.; Zhang, J.; Xiang, B. *Nanotechnology* **2016**, *27* (13), 13LT01.

(57) Li, X.; Puretzky, A. A.; Sang, X.; KC, S.; Tian, M.; Ceballos, F.; Mahjouri-Samani, M.; Wang, K.; Unocic, R. R.; Zhao, H.; Duscher, G.; Cooper, V. R.; Rouleau, C. M.; Geohegan, D. B.; Xiao, K. *Adv. Funct. Mater.* **2016**, *27* (19), 1603850.

(58) Liu, H.; Antwi, K.; Chua, S.; Chi, D. *Nanoscale* **2014**, *6* (1), 624–629.

(59) Wang, Z. Q.; Liu, P.; Ito, Y.; Ning, S. C.; Tan, Y. W.; Fujita, T.; Hirata, A.; Chen, M. W. *Sci. Rep.* **2016**, *6*, 21536.

(60) Li, H.; Wu, X.; Liu, H.; Zheng, B.; Zhang, Q.; Zhu, X.; Wei, Z.; Zhuang, X.; Zhou, H.; Tang, W.; Duan, X.; Pan, A. *ACS Nano* **2017**, *11* (1), 961–967.

(61) Yamamoto, M.; Einstein, T. L.; Fuhrer, M. S.; Cullen, W. G. *J. Phys. Chem. C* **2013**, *117* (48), 25643–25649.

(62) van der Zande, A. M.; Huang, P. Y.; Chenet, D. a; Berkelbach, T. C.; You, Y.; Lee, G.-H.; Heinz, T. F.; Reichman, D. R.; Muller, D. A; Hone, J. C. *Nat. Mater.* **2013**, *12* (6), 554–561.

(63) Najmaei, S.; Liu, Z.; Zhou, W.; Zou, X.; Shi, G.; Lei, S.; Yakobson, B. I.; Idrobo, J.-C.; Ajayan, P. M.; Lou, J. *Nat. Mater.* **2013**, *12* (8), 754–759.

(64) Zhou, W.; Zou, X.; Najmaei, S.; Liu, Z.; Shi, Y.; Kong, J.; Lou, J.; Ajayan, P. M.; Yakobson, B. I.; Idrobo, J. C. *Nano Lett.* **2013**, *13* (6), 2615–2622.

(65) Komsa, H. P.; Kurasch, S.; Lehtinen, O.; Kaiser, U.; Krasheninnikov, A. V. *Phys. Rev. B - Condens. Matter Mater. Phys.* **2013**, *88*, 035301.

(66) Le, D.; Rawal, T. B.; Rahman, T. S. *J. Phys. Chem. C* **2014**, *118* (10), 5346–5351.

(67) Ryu, G. H.; France-Lanord, A.; Wen, Y.; Zhou, S.; Grossman, J. C.; Warner, J. H. *ACS Nano* **2018**, *12* (11), 11638–11647.

(68) Chen, Q.; Li, H.; Zhou, S.; Xu, W.; Chen, J.; Sawada, H.; Allen, C. S.; Kirkland, A. I.; Grossman, J. C.; Warner, J. H. *ACS Nano* **2018**, *12* (8), 7721–7730.

(69) He, Z.; Wang, X.; Xu, W.; Zhou, Y.; Sheng, Y.; Rong, Y.; Smith, J. M.; Warner, J. H. *ACS Nano* **2016**, *10* (6) 5847–5855.

(70) Chen, Q.; Li, H.; Xu, W.; Wang, S.; Sawada, H.; Allen, C. S.; Kirkland, A. I.; Grossman, C.; Warner, J. H.; Grossman, J. C.; Warner, J. H. *Nano Lett.* **2017**, *17* (9), 5502–5507.

(71) Novoselov, K. S.; Jiang, D.; Schedin, F.; Booth, T. J.; Khotkevich, V. V; Morozov, S. V;

Geim, A. K. *Proc. Natl. Acad. Sci. U. S. A.* **2005**, *102* (30), 10451–10453.

(72) Haigh, S. J.; Gholinia, A.; Jalil, R.; Romani, S.; Britnell, L.; Elias, D. C.; Novoselov, K. S.; Ponomarenko, L. a.; Geim, A. K.; Gorbachev, R. V. *Nat. Mater.* **2012**, *11* (9), 764–767.

(73) Rosenberger, M. R.; Chuang, H. J.; McCreary, K. M.; Hanbicki, A. T.; Sivaram, S. V.; Jonker, B. T. *ACS Appl. Mater. Interfaces* **2018**, *10* (12), 10379–10387.

(74) Shi, Y.; Li, H.; Li, L. *Chem. Soc. Rev.* **2014**, *44*, 2744–2756.

(75) Lee, Y. H.; Zhang, X. Q.; Zhang, W.; Chang, M. T.; Lin, C. Te; Chang, K. Di; Yu, Y. C.; Wang, J. T. W.; Chang, C. S.; Li, L. J.; Lin, T. W. *Adv. Mater.* **2012**, *24* (17), 2320–2325.

(76) Cain, J. D.; Hanson, E. D.; Dravid, V. P. *J. Appl. Phys.* **2018**, *123*, 204304.

(77) Shi, Y.; Zhou, W.; Lu, A.-Y.; Fang, W.; Lee, Y.-H.; Hsu, A. L.; Kim, S. M.; Kim, K. K.; Yang, H. Y.; Li, L.-J.; Idrobo, J.-C.; Kong, J. *Nano Lett.* **2012**, *12*, 2784–2791.

(78) Lee, Y. H.; Yu, L.; Wang, H.; Fang, W.; Ling, X.; Shi, Y.; Lin, C. Te; Huang, J. K.; Chang, M. T.; Chang, C. S.; Dresselhaus, M.; Palacios, T.; Li, L. J.; Kong, J. *Nano Lett.* **2013**, *13* (4), 1852–1857.

(79) Shim, G. W.; Yoo, K.; Seo, S.-B.; Shin, J.; Jung, D. Y.; Kang, I.-S.; Ahn, C. W.; Cho, B. J.; Choi, S.-Y. *ACS Nano* **2014**, *7*, 6655–6662.

(80) Kobayashi, Y.; Sasaki, S.; Mori, S.; Hibino, H.; Liu, Z.; Watanabe, K.; Taniguchi, T.; Suenaga, K.; Maniwa, Y.; Miyata, Y. *ACS Nano* **2015**, *9* (4), 4056–4063.

(81) Desai, S. B.; Seol, G.; Kang, J. S.; Fang, H.; Battaglia, C.; Kapadia, R.; Ager, J. W.; Guo, J.; Javey, A. *Nano Lett.* **2014**, *14* (8), 4592–4597.

(82) Yun, S. J.; Chae, S. H.; Kim, H.; Park, J. C.; Park, J.; Han, G. H.; Lee, J. S.; Kim, S. M.; Oh, H. M.; Seok, J.; Jeong, M. S.; Kim, K. K.; Lee, Y. H. *ACS Nano* **2015**, *9* (5), 5510–5519.

(83) Okada, M.; Sawazaki, T.; Watanabe, K.; Taniguch, T.; Hibino, H.; Shinohara, H.; Kitaura, R. *ACS Nano* **2014**, No. Xx, 2–6.

(84) Gong, Y.; Ye, G.; Lei, S.; Shi, G.; He, Y.; Lin, J.; Zhang, X.; Vajtai, R.; Pantelides, S. T.; Zhou, W.; Li, B.; Ajayan, P. M. *Adv. Funct. Mater.* **2016**, *26*, 2009–2015.

(85) Sahoo, P. K.; Memaran, S.; Xin, Y.; Balicas, L.; Gutiérrez, H. R. *Nature* **2018**, *553* (7686), 63–67.

(86) Zhang, Y.; Zhang, Y.; Ji, Q.; Ju, J.; Yuan, H.; Shi, J.; Gao, T.; Ma, D.; Liu, M.; Chen, Y.; Song, X.; Hwang, H. Y.; Cui, Y.; Liu, Z. *ACS Nano* **2013**, *7* (10), 8963–8971.

(87) Liu, Z.; Kan, M.; Zhang, Y.; Gao, T.; Qiao, X.; Chen, Y.; Ma, D.; Ji, Q.; Feng, J.; Liu, M.; Sun, Q.; Tan, P.-H.; Zhang, Y. *Nano Lett.* **2013**, *13* (8), 3870–3877.

(88) Azizi, A.; Zou, X.; Ercius, P.; Zhang, Z.; Elías, A. L.; Perea-López, N.; Stone, G.; Terrones, M.; Yakobson, B. I.; Alem, N. *Nat. Commun.* **2014**, *5*, 4867.

(89) Park, J.; Choudhary, N.; Smith, J.; Lee, G.; Kim, M.; Choi, W. *Appl. Phys. Lett.* **2015**, *106*, 012104.

(90) Chen, W.; Zhao, J.; Zhang, J.; Gu, L.; Yang, Z.; Li, X.; Yu, H.; Zhu, X.; Yang, R.; Shi, D.; Lin, X.; Guo, J.; Bai, X.; Zhang, G. *J. Am. Chem. Soc.* **2015**, *137* (50), 15632–15635.

(91) Song, X.; Gao, T.; Nie, Y.; Zhuang, J.; Sun, J.; Ma, D.; Shi, J.; Lin, Y.; Ding, F.; Zhang, Y.; Liu, Z. *Nano Lett.* **2016**, *16* (10), 6109–6116.

(92) Meng, L.; Zhang, Y.; Hu, S.; Wang, X.; Liu, C.; Guo, Y.; Wang, X.; Yan, X. *Appl. Phys. Lett.* **2016**, *108* (26), 263104.

(93) McCreary, A.; Berkdemir, A.; Wang, J.; Nguyen, M. A.; Fujisawa, K.; Kabius, B.; Carozo, V.; Cullen, D. A.; Mallouk, T. E.; Zhu, J.; Terrones, M. *J. Mater. Res.* **2016**, *31* (7), 931–944.

(94) Wang, S.; Rong, Y.; Fan, Y.; Pacios, M.; Bhaskaran, H.; He, K.; Warner, J. H. *Chem. Mater.* **2014**, *26*, 6371–6379.

(95) Xu, Z.; Zhang, Y.; Lin, S.; Zheng, C.; Zhong, Y. L.; Xia, X.; Li, Z.; Sophia, P. J.; Fuhrer, M. S.; Cheng, Y.-B.; Bao, Q. *ACS Nano* **2015**, *9* (6), 6178–6187.

(96) Li, S.; Wang, S.; Tang, D.-M.; Zhao, W.; Xu, H.; Chu, L.; Bando, Y.; Golberg, D.; Eda, G. *Appl. Mater. Today* **2015**, *1* (1), 60–66.

(97) Wang, S.; Pacios, M.; Bhaskaran, H.; Warner, J. H. *Nanotechnology* **2016**, *27* (8), 85604.

(98) Liu, X.; Wu, J.; Yu, W.; Chen, L.; Huang, Z.; Jiang, H.; He, J.; Liu, Q.; Lu, Y.; Zhu, D.; Liu, W.; Cao, P.; Han, S.; Xiong, X.; Xu, W.; Ao, J.-P.; Ang, K.-W.; He, Z. *Adv. Funct. Mater.* **2017**, *27* (13), 1606469.

(99) Ohring, M. *Materials Science of Thin Films*, 2nd ed.; Elsevier Inc.: Hoboken, New Jersey, 2002.

(100) Zhang, J.; Yu, H.; Chen, W.; Tian, X.; Liu, D.; Cheng, M.; Xie, G.; Yang, W.; Yang, R.; Bai, X.; Shi, D.; Zhang, G. *ACS Nano* **2014**, *8* (6), 6024–6030.

(101) Rong, Y.; Fan, Y.; Leen Koh, A.; Robertson, A. W.; He, K.; Wang, S.; Tan, H.; Sinclair, R.; Warner, J. H. *Nanoscale* **2014**, *6* (20), 12096–12103.

(102) Rong, Y.; He, K.; Pacios, M.; Robertson, A. W.; Bhaskaran, H.; Warner, J. H. *ACS Nano* **2015**, *9* (4), 3695–3703.

(103) Nan, T.; Jiang, T.; Ma, X.; Xie, Y.; Yang, M.; Wang, Z.; Hao, Y.; Zhao, Y.; Lei, Y.; Zhan, Y.; Zhu, Q.; Wang, H.; Wu, R.; Sun, J.; Wang, W. *Nanotechnology* **2017**, *28* (32), 325602.

(104) Li, S.; Lin, Y. C.; Zhao, W.; Wu, J.; Wang, Z.; Hu, Z.; Shen, Y.; Tang, D. M.; Wang, J.; Zhang, Q.; Zhu, H.; Chu, L.; Zhao, W.; Liu, C.; Sun, Z.; Taniguchi, T.; Osada, M.; Chen, W.; Xu, Q. H.; Wee, A. T. S.; Suenaga, K.; Ding, F.; Eda, G. *Nat. Mater.* **2018**, *17* (6), 535–542.

(105) Zhou, J.; Lin, J.; Huang, X.; Zhou, Y.; Chen, Y.; Xia, J.; Wang, H.; Xie, Y.; Yu, H.; Lei,

J.; Wu, D.; Liu, F.; Fu, Q.; Zeng, Q.; Hsu, C.-H.; Yang, C.; Lu, L.; Yu, T.; Shen, Z.; Lin, H.; Yakobson, B. I.; Liu, Q.; Suenaga, K.; Liu, G.; Liu, Z. *Nature* **2018**, *556* (7701), 355–359.

(106) Rajan, A. G.; Warner, J. H.; Blankschtein, D.; Strano, M. S. *ACS Nano* **2016**, *10* (4), 4330–4344.

(107) Liu, K.-K.; Zhang, W.; Lee, Y.-H.; Lin, Y.-C.; Chang, M.-T.; Su, C.-Y.; Chang, C.-S.; Li, H.; Shi, Y.; Zhang, H.; Lai, C.-S.; Li, L.-J. *Nano Lett.* **2012**, *12*, 1538–1544.

(108) Zhan, Y.; Liu, Z.; Najmaei, S.; Ajayan, P. M.; Lou, J. *Small* **2012**, *8* (7), 966–971.

(109) Yu, Y.; Li, C.; Liu, Y.; Su, L.; Zhang, Y.; Cao, L. *Sci. Rep.* **2013**, *3*, 1866.

(110) Kang, K.; Xie, S.; Huang, L.; Han, Y.; Huang, P. Y.; Mak, K. F.; Kim, C.-J.; Muller, D.; Park, J. *Nature* **2015**, *520* (7549), 656–660.

(111) Eichfeld, S. M.; Hossain, L.; Lin, Y.; Piasecki, A. F.; Kupp, B.; Birdwell, A. G.; Burke, R. A.; Lu, N.; Peng, X.; Li, J.; Azcatl, A.; McDonnell, S.; Wallace, R. M.; Kim, M. J.; Mayer, T. S.; Redwing, J. M.; Robinson, J. A. *ACS Nano* **2015**, *9* (2), 2080–2087.

(112) Azizi, A.; Eichfeld, S.; Geschwind, G.; Zhang, K.; Jiang, B. *ACS Nano* **2015**, *9* (5), 4882–4890.

(113) Loh, K. P.; Poh, S. M.; Zhao, X.; Rong Tan, S. J.; Fu, D.; Fei, W.; Chu, L.; Jiadong, D.; Zhou, W.; Pennycook, S. J.; Castro Neto, A. H. *ACS Nano* **2018**, *12* (8), 7562–7570.

(114) Liu, H.; Chen, J.; Yu, H.; Yang, F.; Jiao, L.; Liu, G.; Ho, W.; Gao, C.; Jia, J.; Yao, W.; Xie, M. *Nat. Commun.* **2015**, *6*, 8180.

(115) Vishwanath, S.; Liu, X.; Rouvimov, S.; Mende, P. C.; Azcatl, A.; McDonnell, S.; Wallace, R. M.; Feenstra, R. M.; Furdyna, J. K.; Jena, D.; Xing, H. G. *2D Mater.* **2015**, 024007.

(116) Liu, H. J.; Jiao, L.; Xie, L.; Yang, F.; Chen, J. L.; Ho, W. K.; Gao, C. L.; Jia, J. F.; Cui, X. D.; Xie, M. H. *2D Mater.* **2015**, 034004.

(117) Roy, A.; Movva, H. C. P.; Satpati, B.; Kim, K.; Dey, R.; Rai, A.; Pramanik, T.; Guchhait, S.; Tutuc, E.; Banerjee, S. K. *ACS Appl. Mater. Interfaces* **2016**, *8*, 7396–7402.

(118) Poh, S. M.; Zhao, X.; Jun, S.; Tan, R.; Fu, D.; Fei, W. *ACS Nano* **2018**, *12*, 7562–7570.

(119) Dumcenco, D.; Ovchinnikov, D.; Marinov, K.; Lazic, P.; Gibertini, M.; Marzari, N.; Sanchez, O. L.; Kung, Y.; Krasnozhon, D.; Chen, M.; Bertolazzi, S.; Gillet, P.; Fontcuberta i Morral, A.; Radenovic, A.; Kis, A. *ACS Nano* **2015**, *9* (4), 4611–4620.

(120) Cho, K.; Eichfeld, S. M.; Smyth, C. M.; Redwing, J. M.; Addou, R.; Wallace, R. M.; Fölsch, S.; Fullerton-Shirey, S. K.; Haque, M. A.; Zhang, X.; Jariwala, B.; Nie, Y.; Li, J.; Bersch, B. M.; Lin, Y.-C.; Feenstra, R. M.; Xu, K.; Zhang, K.; Pan, Y.; Choudhury, T. H.; Wang, B.; Robinson, J. A. *ACS Nano* **2018**, *12* (2), 965–975.

(121) Zhang, K.; Feng, S.; Wang, J.; Azcatl, A.; Lu, N.; Addou, R.; Wang, N.; Zhou, C.; Lerach, J.; Bojan, V.; Kim, M. J.; Chen, L. Q.; Wallace, R. M.; Terrones, M.; Zhu, J.; Robinson, J.

A. *Nano Lett.* **2015**, *15* (10), 6586–6591.

(122) Zhang, X.; Choudhury, T. H.; Chubarov, M.; Xiang, Y.; Jariwala, B.; Zhang, F.; Alem, N.; Wang, G.-C.; Robinson, J. A.; Redwing, J. M. *Nano Lett.* **2018**,*18* (2), 1049–1056.

(123) Ji, H. G.; Lin, Y.-C.; Nagashio, K.; Maruyama, M.; Solís-Fernández, P.; Sukma Aji, A.; Panchal, V.; Okada, S.; Suenaga, K.; Ago, H. *Chem. Mater.* **2017**, *30* (2), 403–411.

(124) Chen, J.; Zhao, X.; Tan, S. J. R.; Xu, H.; Wu, B.; Liu, B.; Fu, D.; Fu, W.; Geng, D.; Liu, Y.; Liu, W.; Tang, W.; Li, L.; Zhou, W.; Sum, T. C.; Loh, K. P. *J. Am. Chem. Soc.* **2017**, *139* (3), 1073–1076.

(125) Ago, H.; Endo, H.; Solís-Fernández, P.; Takizawa, R.; Ohta, Y.; Fujita, Y.; Yamamoto, K.; Tsuji, M. *ACS Appl. Mater. Interfaces* **2015**, *7* (9), 5265–5273.

(126) Li, J.; Browning, P. N.; Lin, Z.; Terrones, M.; Lin, Y.-C.; Calderin, L.; Peng, X.; Lee, C. H.; Robinson, J. A.; Kim, M. J.; Perea-Lopez, N.; Mayer, T. S.; Sun, C.; Bresnehan, M. S.; Lu, N. *ACS Nano* **2014**, *8* (4), 3715–3723.

(127) Zhang, F.; Wang, Y.; Erb, C.; Wang, K.; Moradifar, P.; Crespi, V.; Alem, N. *arXiv* **2018**, 1801.00487.

(128) Li, B.; Gong, Y.; Hu, Z.; Brunetto, G.; Yang, Y.; Ye, G.; Zhang, Z.; Lei, S.; Jin, Z.; Bianco, E.; Zhang, X.; Wang, W.; Lou, J.; Galvão, D. S.; Tang, M.; Yakobson, B. I.; Vajtai, R.; Ajayan, P. M. *Angew. Chemie* **2016**, *128* (36), 10814–10819.

(129) Liu, Y.; Weiss, N. O.; Duan, X.; Cheng, H.-C.; Huang, Y.; Duan, X. *Nat. Rev. Mater.* **2016**, *1* (9), 16042.

(130) Suk, J. W.; Kitt, A.; Magnuson, C. W.; Hao, Y.; Ahmed, S.; An, J.; Swan, A. K.; Goldberg, B. B.; Ruoff, R. S. *ACS Nano* **2011**, *5* (9), 6916–6924.

(131) Her, M.; Beams, R.; Novotny, L. *Phys. Lett. Sect. A Gen. At. Solid State Phys.* **2013**, *377* (21–22), 1455–1458.

(132) Gomez De Arco, L.; Zhang, Y.; Schlenker, C. W.; Ryu, K.; Thompson, M. E.; Zhou, C. *ACS Nano* **2010**, *4* (5), 2865–2873.

(133) Li, H.; Zhang, Q.; Yap, C. C. R.; Tay, B. K.; Edwin, T. H. T.; Olivier, A.; Baillargeat, D. *Adv. Funct. Mater.* **2012**, *22* (7), 1385–1390.

(134) Mignuzzi, S.; Pollard, A. J.; Bonini, N.; Brennan, B.; Gilmore, I. S.; Pimenta, M. A.; Richards, D.; Roy, D. *Phys. Rev. B* **2015**, *91*, 195411.

(135) Williams, D. B.; Carter, C. B. *Transmission Electron Microscopy*, 2nd ed.; Springer, 2009.

(136) Krivanek, O. L.; Chisholm, M. F.; Nicolosi, V.; Pennycook, T. J.; Corbin, G. J.; Dellby, N.; Murfitt, M. F.; Own, C. S.; Szilagyi, Z. S.; Oxley, M. P.; Pantelides, S. T.; Pennycook, S. J. *Nature* **2010**, *464* (7288), 571–574.

(137) Egerton, R. F.; Li, P.; Malac, M. *Micron* **2004**, *35* (6), 399–409.

(138) Komsa, H. P.; Kotakoski, J.; Kurasch, S.; Lehtinen, O.; Kaiser, U.; Krasheninnikov, A. V.

Phys. Rev. Lett. **2012**, *109* (3), 1–5.

(139) Zhao, X.; Kotakoski, J.; Meyer, J. C.; Sutter, E.; Sutter, P.; Krasheninnikov, A. V.; Kaiser, U.; Zhou, W. *MRS Bull.* **2017**, *42* (9), 667–676.

(140) Bogaert, K.; Liu, S.; Chesin, J.; Titow, D.; Gradecak, S.; Garaj, S. *Nano Lett.* **2016**, *16* (8), 5129–5134.

(141) Tan, C.; Zhang, H. *J. Am. Chem. Soc.* **2015**, *137*, 12162–12174.

(142) Wang, Q. H.; Kalantar-Zadeh, K.; Kis, A.; Coleman, J. N.; Strano, M. S. *Nat. Nanotechnol.* **2012**, *7* (11), 699–712.

(143) Kang, J.; Tongay, S.; Li, J.; Wu, J. *J. Appl. Phys.* **2013**, *113*, 143703.

(144) Ogletree, D. F.; Schuck, P. J.; Weber-Bargioni, A. F.; Borys, N. J.; Aloni, S.; Bao, W.; Barja, S.; Lee, J.; Melli, M.; Munechika, K.; Whitelam, S.; Wickenburg, S. *Adv. Mater.* **2015**, *27* (38), 5693–5719.

(145) Bao, W.; Borys, N. J.; Ko, C.; Suh, J.; Fan, W.; Thron, A.; Zhang, Y.; Buyanin, A.; Zhang, J.; Cabrini, S.; Ashby, P. D.; Weber-Bargioni, A.; Tongay, S.; Aloni, S.; Ogletree, D. F.; Wu, J.; Salmeron, M. B.; Schuck, P. J. *Nat. Commun.* **2015**, *6*, 7993.

(146) Kobayashi, Y.; Sasaki, S.; Mori, S.; Hibino, H.; Liu, Z.; Watanabe, K. *ACS Nano* **2015**, *9* (4), 4056–4063.

(147) Gan, L.-Y.; Zhang, Q.; Zhao, Y.-J.; Cheng, Y.; Schwingenschlögl, U. *Sci. Rep.* **2014**, *4*, 6691.

(148) Song, J.-G.; Ryu, G. H.; Lee, S. J.; Sim, S.; Lee, C. W.; Choi, T.; Jung, H.; Kim, Y.; Lee, Z.; Myoung, J.-M.; Dussarrat, C.; Lansalot-Matras, C.; Park, J.; Choi, H.; Kim, H. *Nat. Commun.* **2015**, *6*, 7817.

(149) Wei, X.-L.; Zhang, H.; Guo, G.-C.; Li, X.-B.; Lau, W.-M.; Liu, L.-M. *J. Mater. Chem. A* **2014**, *2* (7), 2101–2109.

(150) Schaefer, S. C. Report of Investigation 8405; U.S. Department of the Interior, Bureau of Mines, U.S. Government Printing Office: Washington, DC, 1980.

(151) Susarla, S.; Kochat, V.; Kutana, A.; Hachtel, J. A.; Idrobo, J. C.; Vajtai, R.; Yakobson, B. I.; Tiwary, C. S.; Ajayan, P. M. *Chem. Mater.* **2017**, *29* (17), 7431–7439.

(152) Susarla, S.; Hachtel, J. A.; Yang, X.; Kutana, A.; Apte, A.; Jin, Z.; Vajtai, R.; Idrobo, J. C.; Lou, J.; Yakobson, B. I.; Tiwary, C. S.; Ajayan, P. M. *Adv. Mater.* **2018**, *30*, 1804218.

(153) Bogaert, K.; Liu, S.; Liu, T.; Guo, N.; Zhang, C.; Gradečak, S.; Garaj, S. *Sci. Rep.* **2018**, *8*, 12889.

(154) Nguyen, E. P.; Carey, B. J.; Ou, J. Z.; van Embden, J.; Gaspera, E. Della; Chrimes, A. F.; Spencer, M. J. S.; Zhuiykov, S.; Kalantar-Zadeh, K.; Daeneke, T. *Adv. Mater.* **2015**, *27* (40), 6225–6229.

(155) Pierucci, D.; Henck, H.; Aziza, Z. Ben; Naylor, C. H.; Balan, A.; Rault, J. E.; Silly, M. G.; Dappe, Y. J.; Bertran, F.; Fèvre, P. Le; Sirotti, F.; Johnson, A. T. C.; Ouerghi, A. *ACS*

Nano **2017**, *11* (2), 1755–1761.

(156) Kang, M.; Kim, B.; Ryu, S. H.; Jung, S. W.; Kim, J.; Moreschini, L.; Jozwiak, C.; Rotenberg, E.; Bostwick, A.; Kim, K. S. *Nano Lett.* **2017**, *17* (3), 1610–1615.

(157) Azizi, A.; Wang, Y.; Lin, Z.; Wang, K.; Elías, A. L.; Terrones, M.; Crespi, V. H.; Alem, N. *Nano Lett.* **2016**, *16* (11), 6982–6987.

(158) Rhodes, D.; Chenet, D. A.; Janicek, B. E.; Nyby, C.; Lin, Y.; Jin, W.; Edelberg, D.; Mannebach, E.; Finney, N.; Antony, A.; Schiros, T.; Klarr, T.; Mazzoni, A.; Chin, M.; Chiu, Y. C..; Zheng, W.; Zhang, Q. R.; Ernst, F.; Dadap, J. I.; Tong, X.; Ma, J.; Lou, R.; Wang, S.; Qian, T.; Ding, H.; Osgood, R. M.; Paley, D. W.; Lindenberg, A. M.; Huang, P. Y.; Pasupathy, A. N.; Dubey, M.; Hone, J.; Balicas, L. *Nano Lett.* **2017**, *17* (3), 1616–1622.

(159) Ullah, F.; Sim, Y.; Le, C. T.; Seong, M.; Jang, J. I.; Rhim, S. H.; Tran Khac, B. C.; Chung, K.; Park, K.; Lee, Y.; Kim, K.; Jeong, H. Y.; Kim, Y. S. *ACS Nano* **2017**, *11* (9), 8822–8828.

(160) Withers, F.; Del Pozo-Zamudio, O.; Mishchenko, A.; Rooney, A. P.; Gholinia, A.; Watanabe, K.; Taniguchi, T.; Haigh, S. J.; Geim, A. K.; Tartakovskii, A. I.; Novoselov, K. S. *Nat. Mater.* **2015**, *14*, 301–306.

(161) Jariwala, D.; Sangwan, V. K.; Lauhon, L. J.; Marks, T. J.; Hersam, M. C. *ACS Nano* **2014**, *8* (2), 1102–1120.

(162) Pospischil, A.; Furchi, M. M.; Mueller, T. *Nat. Nanotechnol.* **2014**, *9*, 257–261.

(163) Ross, J. S.; Klement, P.; Jones, A. M.; Ghimire, N. J.; Yan, J.; Mandrus, D. G.; Taniguchi, T.; Watanabe, K.; Kitamura, K.; Yao, W.; Cobden, D. H.; Xu, X. *Nat. Nanotechnol.* **2014**, *9*, 268–272.

(164) Chhowalla, M.; Shin, H. S.; Eda, G.; Li, L.-J.; Loh, K. P.; Zhang, H. *Nat. Chem.* **2013**, *5* (4), 263–275.

(165) Kresse, G.; Hafner, J. *Phys. Rev. B* **1993**, *47*, 558.

(166) Kresse, G.; Furthmu, J. *Phys. Rev. B* **1996**, *54*, 16.

(167) Perdew, J. P.; Chevary, J. A.; Vosko, S. H.; Jackson, K. A.; Pederson, M. R.; Singh, D. J.; Fiolhais, C. *Phys. Rev. B* **1992**, *46*, 11.

(168) Blöchl, P. E. *Phys. Rev. B* **1994**, *50*, 24.

(169) Azizi, A.; Wang, Y.; Stone, G.; Elías, A. L.; Lin, Z.; Terrones, M.; Crespi, V. H.; Alem, N. *Nano Lett.* **2017**, *17* (5), 2802–2808.

(170) Yang, S.-Z.; Sun, W.; Zhang, Y.-Y.; Gong, Y.; Oxley, M. P.; Lupini, A. R.; Ajayan, P. M.; Chisholm, M. F.; Pantelides, S. T.; Zhou, W. *Phys. Rev. Lett.* **2019**, *122* (10), 106101.

(171) Li, Y.; Chernikov, A.; Zhang, X.; Rigosi, A.; Hill, H. M.; Van Der Zande, A. M.; Chenet, D. A.; Shih, E. M.; Hone, J.; Heinz, T. F. *Phys. Rev. B* **2014**, *90* (20), 205422.

(172) Amani, M.; Taheri, P.; Addou, R.; Ahn, G. H.; Kiriya, D.; Lien, D.-H. H.; Ager, J. W.;

Wallace, R. M.; Javey, A. *Nano Lett.* **2016**, *16* (4), 2786–2791.

(173) Schubert, E. F.; Göbel, E. O.; Horikoshi, Y.; Ploog, K.; Queisser, H. J. *Phys. Rev. B* **1984**, *30* (2), 813–820.

(174) Collins, C. J.; Sampath, A. V.; Garrett, G. A.; Sarney, W. L.; Shen, H.; Wraback, M.; Nikiforov, A. Y.; Cargill, G. S.; Dierolf, V. *Appl. Phys. Lett.* **2005**, *86* (3), 031916.

(175) Cheiwchanchamnangij, T.; Lambrecht, W. R. L. *Phys. Rev. B* **2012**, *85* (20), 205302.

(176) Huang, B.; Yoon, M.; Sumpter, B. G.; Wei, S.-H.; Liu, F. *Phys. Rev. Lett.* **2015**, *115* (12), 126806.

(177) Alharbi, A.; Shahrjerdi, D. *Appl. Phys. Lett.* **2016**, *109* (19), 193502.

(178) McCreary, K. M.; Hanbicki, A. T.; Singh, S.; Kawakami, R. K.; Jernigan, G. G.; Ishigami, M.; Ng, A.; Brintlinger, T. H.; Stroud, R. M.; Jonker, B. T. *Sci. Rep.* **2016**, *6*, 35154.

(179) Amani, M.; Burke, R. A.; Ji, X.; Zhao, P.; Lien, D. H.; Taheri, P.; Ahn, G. H.; Kirya, D.; Ager, J. W.; Yablonovitch, E.; Kong, J.; Dubey, M.; Javey, A. *ACS Nano* **2016**, *10* (7), 6535–6541.

(180) Ahn, G. H.; Amani, M.; Rasool, H.; Lien, D.-H.; Mastandrea, J. P.; Joel W., A.; Dubey, M.; Chrzan, D. C.; Minor, A. M.; Javey, A. *Nat. Commun.* **2017**, *8* (1), 608.

(181) Kim, S.; Kim, J. H.; Kim, D.; Hwang, G.; Baik, J.; Yang, H.; Cho, S. *2D Mater.* **2017**, *4* (2), 024004.

(182) Castellanos-Gomez, A.; Barkelid, M.; Goossens, A. M.; Calado, V. E.; Van Der Zant, H. S. J.; Steele, G. A. *Nano Lett.* **2012**, *12* (6), 3187–3192.

(183) Dago, A. I.; Ryu, Y. K.; Garcia, R. *Appl. Phys. Lett.* **2016**, *109* (16), 18–22.

(184) Han, Y.; Li, M.-Y. Y.; Jung, G.-S. S.; Marsalis, M. A.; Qin, Z.; Buehler, M. J.; Li, L.-J.; Muller, D. A. *Nat. Mater.* **2018**, *17* (2), 128–133.

(185) Zhang, X.; Zhang, F.; Wang, Y.; Schulman, D. S.; Zhang, T.; Bansal, A.; Alem, N.; Das, S.; Crespi, V. H.; Terrones, M.; Redwing, J. M. *ACS Nano* **2019**, *13* (3), 3341–3352.

(186) Dervin, S.; Dionysiou, D. D.; Pillai, S. C. *Nanoscale* **2016**, *8* (33), 15115–15131.

(187) Zheng, Z.; Grünker, R.; Feng, X. *Adv. Mater.* **2016**, *28* (31), 6529–6545.

(188) Aliprandi, A.; Pakulski, D.; Ciesielski, A.; Samor, P. *ACS Nano* **2017**, *11* (11), 10654–10658.

(189) Garaj, S.; Hubbard, W.; Reina, A.; Kong, J.; Branton, D.; Golovchenko, J. A. *Nature* **2010**, *467* (7312), 190–193.

(190) Garaj, S.; Liu, S.; Golovchenko, J. A.; Branton, D. *Proc. Natl. Acad. Sci.* **2013**, *110* (30), 12192–12196.

(191) Danda, G.; Das, P. M.; Chou, Y.-C.; Mlack, J. T.; Parkin, W. M.; Naylor, C. H.; Fujisawa, K.; Zhang, T.; Fulton, L. B.; Terrones, M.; Johnson, A. T. C.; Drndić, M. *ACS Nano* **2017**,

11 (2), 1937–1945.

(192) Farimani, A. B.; Min, K.; Aluru, N. R. *ACS Nano* **2014**, *8* (8), 7914–7922.

(193) Sint, K.; Wang, B. Y.; Kral, P. *J. Am. Chem. Soc.* **2008**, *130*, 16448–16449.

(194) Cohen-Tanugi, D.; Grossman, J. C. *Nano Lett.* **2012**, *12* (7), 3602–3608.

(195) O'Hern, S. C.; Boutilier, M. S. H.; Idrobo, J. C.; Song, Y.; Kong, J.; Laoui, T.; Atieh, M.; Karnik, R. *Nano Lett.* **2014**, *14* (3), 1234–1241.

(196) Surwade, S. P.; Smirnov, S. N.; Vlassiouk, I. V; Unocic, R. R.; Veith, G. M.; Dai, S.; Mahurin, S. M. *Nat. Nanotechnol.* **2015**, *10* (5), 459–464.

(197) Heiranian, M.; Farimani, A. B.; Aluru, N. R. *Nat. Commun.* **2015**, *6*, 8616.

(198) Feng, J.; Graf, M.; Liu, K.; Ovchinnikov, D.; Dumcenco, D.; Heiranian, M.; Nandigana, V.; Aluru, N. R.; Kis, A.; Radenovic, A. *Nature* **2016**, *536*, 197–200.

(199) Ye, G.; Gong, Y.; Lin, J.; Li, B.; He, Y.; Pantelides, S. T.; Zhou, W.; Vajtai, R.; Ajayan, P. M. *Nano Lett.* **2016**, *16* (2), 1097–1103.

(200) Liu, K.; Lihter, M.; Sarathy, A.; Caneva, S.; Qiu, H.; Deiana, D.; Tileli, V.; Alexander, D. T. L.; Hofmann, S.; Dumcenco, D.; Kis, A.; Leburton, J. P.; Radenovic, A. *Nano Lett.* **2017**, *17* (7), 4223–4230.

(201) Russo, C. J.; Golovchenko, J. A. *Proc. Natl. Acad. Sci.* **2012**, *109* (16), 5953–5957.

(202) Feng, J.; Liu, K.; Graf, M.; Lihter, M.; Bulushev, R. D.; Dumcenco, D.; Alexander, D. T. L.; Krasnozhon, D.; Vuletic, T.; Kis, A.; Radenovic, A. *Nano Lett.* **2015**, *15* (5), 3431–3438.

(203) Kuan, A. T.; Lu, B.; Xie, P.; Szalay, T.; Golovchenko, J. A. *Appl. Phys. Lett.* **2015**, *106* (20), 203109.

(204) Thiruraman, J. P.; Fujisawa, K.; Danda, G.; Das, P. M.; Zhang, T.; Bolotsky, A.; Perea-López, N.; Nicolaï, A.; Senet, P.; Terrones, M.; Drndić, M. *Nano Lett.* **2018**, *18* (3), 1651–1659.

(205) Schweiger, H.; Raybaud, P.; Kresse, G.; Toulhoat, H. *J. Catal.* **2002**, *207* (1), 76–87.

(206) Pham, T.; Gibb, A. L.; Li, Z.; Gilbert, S. M.; Song, C.; Louie, S. G.; Zettl, A. *Nano Lett.* **2016**, *16* (11), 7142–7147.

(207) Klein, D. J. *Chem. Phys. Lett.* **1994**, *217* (3), 261–265.

(208) Zhu, D.; Shu, H.; Jiang, F.; Lv, D.; Asokan, V.; Omar, O.; Yuan, J.; Zhang, Z.; Jin, C. *npj 2D Mater. Appl.* **2017**, *1*, 8.

(209) Zhao, X.; Fu, D.; Ding, Z.; Zhang, Y. Y.; Wan, D.; Tan, S. J. R.; Chen, Z.; Leng, K.; Dan, J.; Fu, W.; Geng, D.; Song, P.; Du, Y.; Venkatesan, T.; Pantelides, S. T.; Pennycook, S. J.; Zhou, W.; Loh, K. P. *Nano Lett.* **2018**, *18* (1), 482–490.

(210) Kotakoski, J.; Santos-Cottin, D.; Krasheninnikov, A. V. *ACS Nano* **2012**, *6* (1), 671–676.

(211) He, K.; Robertson, A. W.; Lee, S.; Yoon, E.; Lee, G. Do; Warner, J. H. *ACS Nano* **2014**, *8* (12), 12272–12279.

(212) Xiao, S. L.; Yu, W. Z.; Gao, S. P. *Surf. Sci.* **2016**, *653*, 107–112.

(213) Sang, X.; Li, X.; Zhao, W.; Dong, J.; Rouleau, C. M.; Geohegan, D. B.; Ding, F.; Xiao, K.; Unocic, R. R. *Nat. Commun.* **2018**, *9*, 2051.

(214) Thomsen, J. D.; Kling, J.; Mackenzie, D. M. A.; Bøggild, P.; Booth, T. J. *ACS Nano* **2019**, *13*, 2281–2288.

(215) Gong, C.; He, K.; Lee, G.-D.; Chen, Q.; Robertson, A. W.; Yoon, E.; Hong, S.; Warner, J. H. *ACS Nano* **2016**, *10* (10), 9397–9410.

(216) Fu, W.; Chen, Y.; Lin, J.; Wang, X.; Zeng, Q.; Zhou, J.; Zheng, L.; Wang, H.; He, Y.; He, H.; Fu, Q.; Suenaga, K.; Yu, T.; Liu, Z. *Chem. Mater.* **2016**, *28* (21), 7613–7618.

(217) Zhang, Y.; Yin, L.; Chu, J.; Shifa, T. A.; Xia, J.; Wang, F.; Wen, Y.; Zhan, X.; Wang, Z.; He, J. *Adv. Mater.* **2018**, *30* (40), 1803665.

(218) Li, H.; Li, P.; Huang, J. K.; Li, M. Y.; Yang, C. W.; Shi, Y.; Zhang, X. X.; Li, L. J. *ACS Nano* **2016**, *10* (11), 10516–10523.

(219) Jain, K. *Excimer Laser Lithography*; SPIE Press: Bellingham, WA, 1990.

(220) Lin, L.; Li, J.; Li, W.; Yogeesh, M. N.; Shi, J.; Peng, X.; Liu, Y.; Rajeeva, B. B.; Becker, M. F.; Liu, Y.; Akinwande, D.; Zheng, Y. *Adv. Funct. Mater.* **2018**, *28* (41), 1803990.